

Insights into the spatiotemporal regulation of the cellular cytoskeleton through applications of FRET

Dissertation
zur Erlangung des Doktorgrades
der Mathematisch-Naturwissenschaftlichen Fakultäten
der Georg-August-Universität zu Göttingen

vorgelegt von
Mišo Mitkovski
aus Bad Homburg, Deutschland

Göttingen, 2005

D7

Referent: *Prof. Dr. Ralf Ficner*

Korreferent: *Prof. Dr. Erwin Neher*

Tag der mündlichen Prüfung: 2. und 3. November 2005

“Za mama, tato i Aleksandar”

Acknowledgments

I would like to acknowledge Dr. Fred S. Wouters for allowing me to conduct research in the field of cellular biophysics. I am thankful to Prof. Dr. Ralf Ficner and especially to Prof. Dr. Erwin Neher for serving as the referee and Anleiter/co-referee on my PhD committee.

I am indebted and thankful to many, who have been my guides along the way. To mention a few, professors Heidi Dobson, Lennart Ågren, Paul Yancey, Earl Fleck, Anne Sylvester, Allan Caplan, Ronald Crawford for having introduced me to an amazing breadth of interesting scientific topics including electroantennography (in picturesque Öland, Sweden), physiology and marine biology (included memorable trips off the Oregon coast and to Friday Harbor), the creation of a *virtual fetal pig dissection*, the field of maize genetics, an introduction to molecular biology and to *ab initio* molecular dynamics. I am thankful for the insights gained on the cellular cytoskeleton while working in the laboratory of professors Mary Osborn and Klaus Weber. This was a special time, as the novel method of RNA interference was just being applied to the study of cytoskeletal proteins. I am also grateful to Agnieszka Patkaniowska for many discussions on that topic and especially on helping me understand new developments in the field of RNAi. I would like to thank Prof. Dr. Jürgen Wehland, Dr. Klemens Rottner and Dr. Theresia Stradal for their kind introduction to live-cell microscopy. For discussions regarding analysis of CLSM derived images I would like to thank Alessandro Esposito and Dr. Rainer Heintzman. I am much indebted to my mother and especially to Fernanda Queiroz for introducing me to the extraordinary technique of flow cytometry and allowing me to use this robust method that ended up producing some exciting results presented here. I am thankful to Peter Nagy for his advice and software for analysis of flow cytometry data.

I would also like to acknowledge the “Open Source” movement and organizations that support free software for making available programs such as L^AT_EX, I_nstaller, BibDesk, PubDesk, Reference Miner and ImageJ (with all the useful plugins), which have been invaluable for the progress of this work. Furthermore, I would like to acknowledge Dr. Rainer Bohrer and the Gesellschaft für wissenschaftliche Datenverarbeitung, Göttingen (GWDG) he is associated with for introducing me to GCG and the plethora of invaluable computing services. Along these lines, I am thankful to Matthias Weyl and Oliver Schade for their support as computer administrators at the European Neuroscience Institute, Göttingen (ENI-G). Wiebke Heinrich and Dagmar Thomitzek of that institution have provided invaluable help with administrative tasks and have supported this work in many ways. A “thank you” goes also to all PhD candidates, postdocs and staff members of ENI-G.

I am thankful to Dr. Michael and Nancy Roach and family for the constant source of inspiration. The many ingenious approaches to problem solving of my father have been an inspiration for the ever-present need for creativity in my work. I am grateful for the early introduction to microscopy I have gotten from my mother.

Finally, I would like to thank my parents and brother for their constant support of my scientific endeavors.

Contents

1	Introduction	1
1.1	The cellular cytoskeleton and the extracellular matrix	1
1.2	Visualizing biochemistry and biophysics at the subcellular level	8
1.3	Linear Extensions for Good Orientation	10
1.4	The FRETing Matrix	11
2	Methods	13
2.1	Linear Extensions for Good Orientation (LEGO)	13
2.1.1	Design Strategy	13
2.1.2	The FRET-acceptor: pVenus-N1	14
2.1.3	The FRET-donor: pECFP-C1 modification	16
2.1.4	Alpha-helix encoding fragments	17
2.1.5	Rho-binding domain of Rhotekin	17
2.1.6	Flow Cytometry	19
2.2	FRETing Matrix	20
2.2.1	Fibronectin labeling and subsequent coating of glass coverslips	20
2.3	Imaging of live and fixed samples	22
2.3.1	Lambda scan of LEGO and the FRETing Matrix	23
2.3.2	Live-cell imaging	23
2.3.3	Interference reflection microscopy	24
2.3.4	Image Analysis	26
2.4	Cell lines	27
2.5	Transfection of DNA vectors into adherent cells	27
2.6	Protocols	28
2.6.1	Primers	28
2.6.2	PCR	28
2.6.3	Restriction Digest	29
2.6.4	Klenow fragment treatment	29
2.6.5	Ligation	30
2.6.6	Gel-extraction	30
2.6.7	Chemical transformation	31
2.6.8	The <i>ReFlex</i> software package	32
2.6.9	The phalloidin stain	33
2.7	Solutions	35
3	Results	36

3.1	LEGO	36
3.1.1	Lambda scan showed ECFP and Venus specific emission peaks	36
3.1.2	Acceptor photobleaching revealed presence of FRET	38
3.1.3	Ratiometric Imaging of Cells Expressing LEGO Constructs	39
3.1.4	Fluorescence Activated Cell Sorting (FACS) of LEGO-transfected cells	44
3.1.5	Estimation of the relative FRET efficiency from flow cytometry data	46
3.2	FRETing Matrix	50
3.2.1	Lambda scan shows Cy3 and Cy5 emission peaks	53
3.2.2	Acceptor photobleaching reveals the high FRET efficiency of the FRETing Matrix	53
3.2.3	Ratiometric imaging of the FRETing Matrix	55
3.2.4	The high FRET efficiency patterns localize along stress fibers	58
3.2.5	The onset of force exertion during cell spreading can be visualized with the FRETing Matrix	58
3.2.6	High FRET efficiency spots correlate with actin stress fibers during cell migration	63
3.2.7	RhoA GTPase is involved in the patterning of the high FRET ratio spots	67
4	Discussion	70
4.1	LEGO	71
4.1.1	Transfection and expression	71
4.1.2	Lambda scan and APB	71
4.1.3	Ratiometric determination of relative FRET efficiency	72
4.1.4	Flow cytometry	73
4.2	FRETing Matrix	77
4.2.1	Lambda scan and acceptor photobleaching	77
4.2.2	Ratiometric visualization of contrast in FRET in the FRETing Matrix	78
4.2.3	Verification of the ratiometric readout via acceptor photobleaching	79
4.2.4	FRET patterns and stress fibers in fixed cells	79
4.2.5	Cell spreading	80
4.2.6	FRET patterns and stress fibers during cell migration	81
4.3	RhoA GTPase was involved in patterning of the high FRET efficiency spots	82
4.4	Conclusions	83

List of Figures

1.1	Selected features of the actin cytoskeleton	3
1.2	The actin cytoskeleton and types of cell adhesions during cell migration	5
1.3	The Rho GTPase activity cycle	6
1.4	Activators and inhibitors of the RhoA GTPase	6
1.5	Integrin heterodimers and their respective ligands.	7
1.6	Dependence of FRET efficiency on donor-acceptor distance and transition dipole orientation	9
2.1	The <i>Raichu-RBD</i> intramolecular FRET biosensor	14
2.2	The DNA makeup and cloning strategy behind the eleven LEGO constructs	15
2.3	Workflow outlining the cloning strategy used to generate the eleven LEGO constructs	18
2.4	The functional domains of fibronectin	20
2.5	Design model for the FRETing Matrix	21
2.6	Interference reflection microscopy	24
2.7	Study of cell adhesion dynamics with interference reflection microscopy	25
3.1	λ scan of HeLaSS6 cell expressing LEGO1	37
3.2	Excitation and emission spectra of ECFP and EYFP	37
3.3	Acceptor photobleaching in a RMCD cell expressing LEGO1	40
3.4	LEGO1-11 ratios of donor and acceptor intensities obtained with CLSM	41
3.5	An exemplary non-linear fit of ratiometric data	42
3.6	Mean ratio and standard error for each LEGO determined by non-linear regression	43
3.7	Linear regression of the means of all LEGO constructs	44
3.8	Residuals from the linear regression line shown in figure 3.7	45
3.9	Example scatter plots obtained with flow cytometry measurements from control cells and those transfected with a LEGO construct	47
3.10	Properties of cells chosen for calculation of relative FRET efficiency	48
3.11	Relative FRET efficiency of HeLaSS6 cells expressing LEGO1-11	49
3.12	Relative FRET efficiency of cells co-transfected with either LEGO and RhoA _{T19N} or LEGO and RhoA _{G14V}	51
3.13	Adherent HeLaSS6 cells co-transfected with either LEGO10 and RhoA _{T19N} or LEGO10 and RhoA _{G14V}	52
3.14	λ -scan of a FRETing Matrix preparation	54

3.15	Excitation and emission spectra of Cy3 and Cy5	55
3.16	Acceptor photobleaching of the FRETing Matrix	56
3.17	Change in FRET efficiency in the FRETing Matrix caused by a NIH/3T3 cell	57
3.18	Validation of the ratiometric method of FRET efficiency measurement with the FRETing Matrix	59
3.19	Phalloidin-based visualization of actin filaments within a RMCD cell grown on the FRETing Matrix	60
3.20	B16F1 cell spreading observed with interference reflection microscopy	61
3.21	GFP-actin and force exertion readout in B16F1 cells during cell spreading	62
3.22	Magnified perspective of cells shown in figures 3.20 and 3.21	64
3.23	Membrane protrusion occurs prior to force exertion; the FRETing Matrix does not exhibit “memory effect”	65
3.24	B16F1 cell migration observed with interference reflection microscopy, by the GFP-actin signal and from the perspective of force exertion . .	66
3.25	Magnified version of the sequence of events shown in figure 3.24 with emphasis on the GFP-actin and force exertion signal	68
3.26	The RhoA GTPase controls patterning of high FRET efficiency spots	69

List of Tables

2.1	FACS analysis excitation/emission filter setup	19
2.2	Lambda scan settings	23
2.3	PCR setup	29
2.4	Scheme for restriction enzyme digest	29
2.5	Klenow fragment restriction site removal	30
2.6	DNA ligation	30
2.7	Phalloidin stain	34
2.8	Solution Recipes	35
3.1	Selected acquisition settings used to collect emission generated by LEGO constructs	38
3.2	Types of plots used to visualize flow cytometry data with the <i>BD</i> <i>FACSDiva</i> software	44
3.3	Number of cells measured with flow cytometry for each transfection combination	46

Abbreviations

C

CLSM: confocal laser scanning microscope

D

DNA: deoxyribonucleic acid

E

E: FRET efficiency

ECFP: enhanced cyan fluorescent protein

ECM: extracellular matrix

EDTA: ethylenediaminetetraacetic acid

F

FA: focal adhesion

FACS: fluorescence activated cell sorting

FAK: focal adhesion kinase

Fn: fibronectin

FRET: Förster resonance energy transfer

G

GAP: GTPase activating proteins

GDI: guanosine dissociation inhibitor

GDP: guanosine-5'-diphosphate

GEF: guanosine exchange factor

GFP: green fluorescent protein

GGTase: geranyl-geranyl transferase

GTPase: an enzyme that can bind and hydrolyze GTP

GTP: guanosine-5'-triphosphate

I

IRM: interference reflection microscopy

L

LEGO: linear extensions for good orientation

M

MCS: multiple cloning site

μg : microgram ($1 \cdot 10^{-6} kg$)

μm : micrometer ($1 \cdot 10^{-6} m$)

ml: milliliter ($1 \cdot 10^{-3} L$)

N

nm: nanometer ($1 \cdot 10^{-9} m$)

P

PBS: phosphate buffered saline

PCR: polymerase chain reaction

PFA: paraformaldehyde

PMT: photomultiplier tube

R

RBD: Rho binding domain of Rhotekin

R_o : the distance at which the FRET efficiency between randomly oriented donor and acceptor VFPs is 50%

RGD domain: asparagine-glycine-aspartate domain

Rho: Ras homology family of small GTPases

RhoA_{G14V}: constitutively active RhoA

RhoA_{T19N}: dominant negative RhoA

RMCD: rat mammary adenocarcinoma cell line

T

TBE: tris buffered EDTA

V

VFP: visually fluorescent protein

Y

YFP: yellow fluorescent protein

Abstract

The cellular cytoskeleton is composed of microfilaments, intermediate filaments, microtubules and a host of accessory proteins that control its dynamics during different, cell-type and environment dependent behaviors. The Rho family of small GTPases play a pivotal role in these processes. RhoA, for instance, simultaneously coordinates focal adhesion (FA) and stress fiber formation. The stress fibers are marked by actomyosin based contractile forces, which concentrate at FAs and contribute to the generation of cytoplasmic tension required for proper cell morphology, adhesion or for cell migration. An optical biosensor based on the principles of the Förster resonance energy transfer (FRET) was created to visualize the amount of active, GTP-bound RhoA present, whose biochemical signaling leads up to the generation of force within the cellular cytoskeleton. The biosensor was optimized with a set of α helices of successively increasing length functioning as linear extensions for good orientation (LEGO). Thereby, a novel approach for the rational design of a FRET biosensor with high detection sensitivity and dynamic range was introduced. The best RhoA biosensor, LEGO10, reported an increase in FRET efficiency, when RhoA was GDP-bound and inactive, while a decrease in FRET efficiency ensued when constitutively active, GTP-bound RhoA was the predominant form.

Transmembrane integrin molecules concentrated at FAs enable indirect contact of the cytoskeleton with the extracellular matrix (ECM) and maintain a continuous bidirectional information flow between the intra- and extracellular environment that regulates gene expression, cell growth, proliferation, and motility. An explanation

for this process requires knowledge about the spatiotemporal activity of proteins and signaling cascades involved in the cytoskeleton-ECM interface. During adhesion or motility cells need to coordinate assembly, maintenance and disassembly of contacts with the ECM, which are pivotal in the generation and conductance of force and traction and underly the control of Rho family GTPases. To study these events, an ECM consisting of fluorescently labeled fibronectin (Fn) was created, in which the applied Cy3 and Cy5 fluorophores operate as a donor-acceptor pair for FRET, thus creating the FRETing Matrix. Simultaneous observation of GFP-labeled cytoskeletal components, such as actin, was possible because of sufficient spectral separation to the Cy3 and Cy5 labeling reagents that were chosen as the FRETing Matrix fluorophores. The FRETing Matrix was used to characterize the spatiotemporal exertion of mechanical force during cell adhesion, spreading and migration. Force-induced structural rearrangements in the FRETing Matrix lead to changes in FRET efficiency that were RhoA GTPase dependent and occurred at FAs and below membrane proximal to stress fibers. During initial stages of cell spreading, cell protrusion due to actin polymerization occurred prior to establishment of adhesion sites through which cells subsequently exerted force necessary for establishment of cytoplasmic tension and ultimately for cell polarity. The FRETing Matrix technique was thus established as a continuous imaging force biosensor that rapidly and faithfully reports on the dynamic interaction of cells with their substratum.

Chapter 1

Introduction

Cell adhesion, migration and morphology are features inherent to life and are essentially dependent on the cellular cytoskeleton that drives them. These features are manifested during embryogenesis [30, 46], neuronal growth cone migration [49, 79], wound healing [38, 48] or white blood cell migration [2, 38, 44, 84, 100, 106]. Irregularities therein can result in pathologies, including cancer metastasis [70] or skin disorders [22, 41, 96], and necessitate an understanding of the underlying molecular [25, 61–63, 71, 75, 102, 104] and mechanical [31, 32, 36, 39, 72, 86, 104] signaling.

1.1 The cellular cytoskeleton and the extracellular matrix

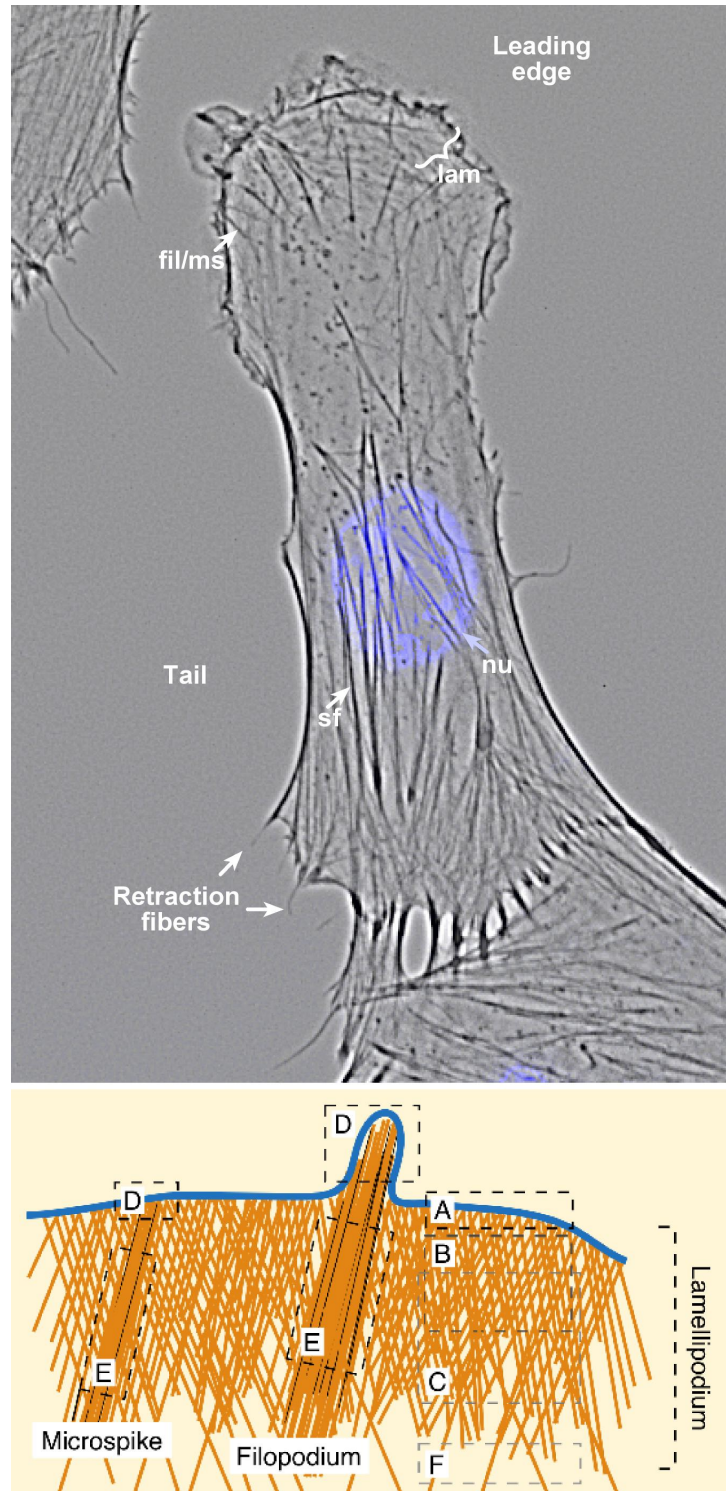
The cellular cytoskeleton is composed of microfilaments, intermediate filaments and microtubules that can be distinguished by their respective diameter of $7-9nm$, $10nm$ and $24nm$ [45]. These key players are complemented by an ever-growing array of proteins that regulate their dynamic behavior [11, 72, 104]. Evidence exists, whereby the activity of these proteins is influenced by mechanical force applied onto cells [39, 73, 86], which in turn are also able to exert force onto their surrounding [6, 39, 86]. The cytoskeleton communicates indirectly with the ECM surrounding the cells via α and β subunits of integrin transmembrane molecules. A continuous bidirectional

exchange of information between the cytoskeleton and the ECM is essential for cells to properly carry out proliferation, gene expression, adhesion and motility [16,28,43]. An explanation for this process necessitates a firm understanding of the proteins and signaling cascades involved in modulation of the cytoskeleton and the cytoskeleton-ECM interface.

The top of figure 1.1 features a RMCD cell to illustrate the distribution of actin microfilaments that have been labeled with phalloidin. In this manner the lamellipodium becomes apparent at the leading edge of the cell, which, depending on the cell type, can vary between $1 - 5\mu m$ in width [80]. The lamellipodium is where cell protrusion during migration occurs and has been termed an area of high actin incorporation leading to the formation of actin bundles. These bundles, while still completely embedded in the lamellipodium, are called microspikes, but can eventually mature to form filopodia, which are structures that protrude beyond the lamellipodium (illustrated in bottom of figure 1.1).

Two schematics of a migrating cell are illustrated in figure 1.2. Section A of this figure describes cell migration from the perspective of the family of small GTPases Rho, Rac and CDC42 and their mode of control over the actin cytoskeleton, while in section B the types of cell-substrate adhesions that occur in parallel are illustrated. In section A it is shown that CDC42 and Rac are active at the leading edge of the cell, while RhoA activity is predominant in the trailing part of the cell [2,26,93]. CDC42 and Rac are known to initiate formation of filopodia and lamellipodia, respectively, while RhoA is involved in stress fiber and focal adhesion formation [9,26,87]. Therefore, as the cell migrates, actin polymerization occurs in the lamellipodium, such that actin filaments are created that are anchored at focal complexes. These complexes remain stationary as the cell moves forward, so that eventually they may fall under the control of RhoA GTPase and mature into focal adhesions. Subsequently, these adhesions may aggregate to form sliding adhesions [95] and may finally be dis-

Figure 1.1: The actin cytoskeleton plays an important role in shape establishment of a cell in various stages of the cell cycle or during cell migration. The upper figure shows the leading edge and the tail of a migrating RMCD cell. Filopodia and microspikes (fil/ms) are part of the lamellipodium (lam) at the leading edge, while stress fibers (sf) are located in the retracting tail region. The nucleus (nu) is emphasized in blue. The lower figure is a cartoon of some of the components of the lamellipodium. In particular it illustrates the actin meshwork in the lamellipodium out of which a microspike can develop, which can later mature into a filopodium [80].



assembled through involvement of microtubules, focal adhesion kinase (FAK) and the GTPase dynamin in a process that is independent of Rho activity [19].

RhoA was of particular interest in this study. The activity cycle which it undergoes is shown in figure 1.3. While it is in the cytoplasm, RhoA is GDP bound and inactive. In fact, it is actively kept in the GDP-bound form by Rho guanine dissociation inhibitors (GDIs) [56], which prevent the dissociation of GDP from RhoA and furthermore prevent post-translational modification of the RhoA C-terminus by geranyl-geranyl transferases (GGTases). Guanine exchange factors (GEFs) facilitate the exchange of GDP to GTP, while GGTases membrane target RhoA through prenylation of the C-terminus. The membrane targeted and GTP loaded form of RhoA then activates downstream effectors. For instance, Rho kinase and mDia are downstream effectors of RhoA, whose activation leads to stress fiber and FA formation [69,95]. GTPase activating proteins (GAPs) increase the inherently low rate of GTP hydrolysis of RhoA, resulting in GDP-bound, inactive RhoA. The RhoA activity cycle is then completed through action of Rho GDIs that bind the GDP-bound RhoA and maintain it as such.

Constitutively active (RhoA_{G14V}) and dominant negative (RhoA_{T19N}) forms of RhoA exist. The GTPase activity is not present in RhoA_{G14V}, which then remains GTP-bound and continuously activates downstream effectors, leading to formation of stress fibers and FAs [69]. The dominant negative RhoA_{T19N} is thought to have an increased affinity for GEFs. This mutant then competes with endogenous RhoA, thereby interrupting signal transduction pathways leading to loss of cytoplasmic tension [81]. A selection of other means not used in this work to activate or inactivate RhoA is shown in figure 1.4 [20, 34, 57, 64, 69].

Stress fibers generated through activity of small GTPases are anchored at adhesion sites. The adhesion sites in turn contain α and β integrin subunits that function as an interface between the cellular cytoskeleton and the ECM. Figure 1.5 illustrates

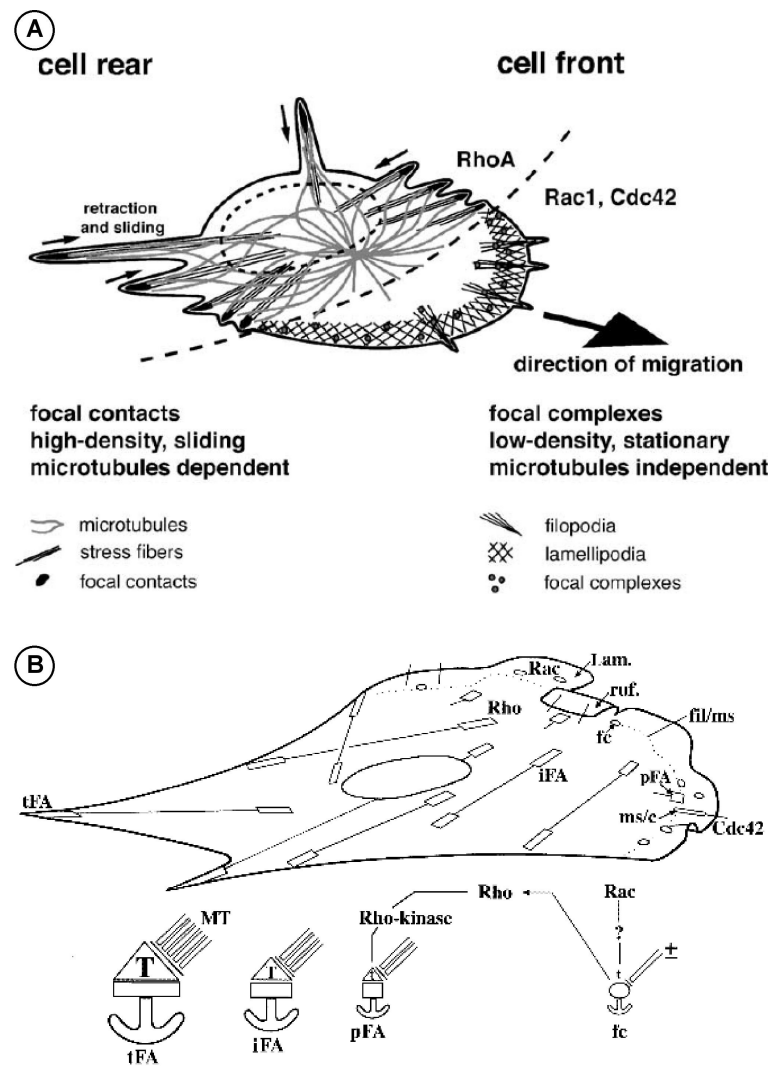


Figure 1.2: Schematic of the types of adhesion sites and constellations of the actin cytoskeleton formed in a migrating cell. Part **A** emphasizes the role of the actin cytoskeleton during cell migration. Rac1 and CDC42 activity at the front of the cell result in actin polymerization and a protruding lamellipodium and filopodia. The rear end of the cell underlies the control of RhoA and microtubules leading to actin-dependent retraction and sliding [97]. Section **B** [77] illustrates the types of contacts formed by an adhering fibroblast with a substrate (abbreviations are: fc: punctate focal complex, ms/c: microspike bundle contact, MT: microtubules, iFA: intermediate focal adhesion in the body of the cell, pFA: precursor of a focal adhesion, tFA: focal adhesion at trailing edge of cell). New contacts are formed in the front (right) part of the cell where the ruffling lamellipodium (ruf. Lam.) is located. The RhoGTPase family and microtubules influence a cell's adhesion dynamics.

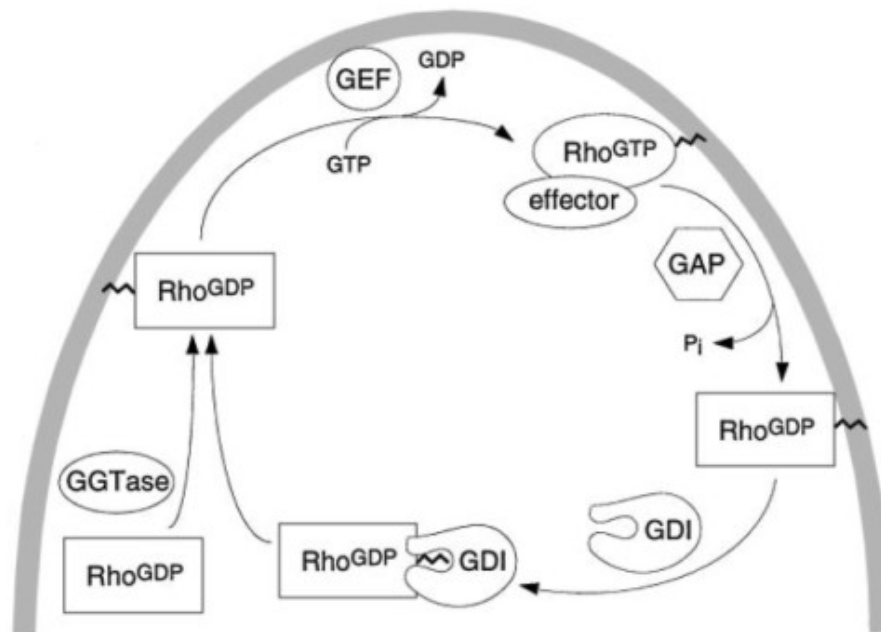


Figure 1.3: A simplified representation of the Rho GTPase activity cycle (from [71])

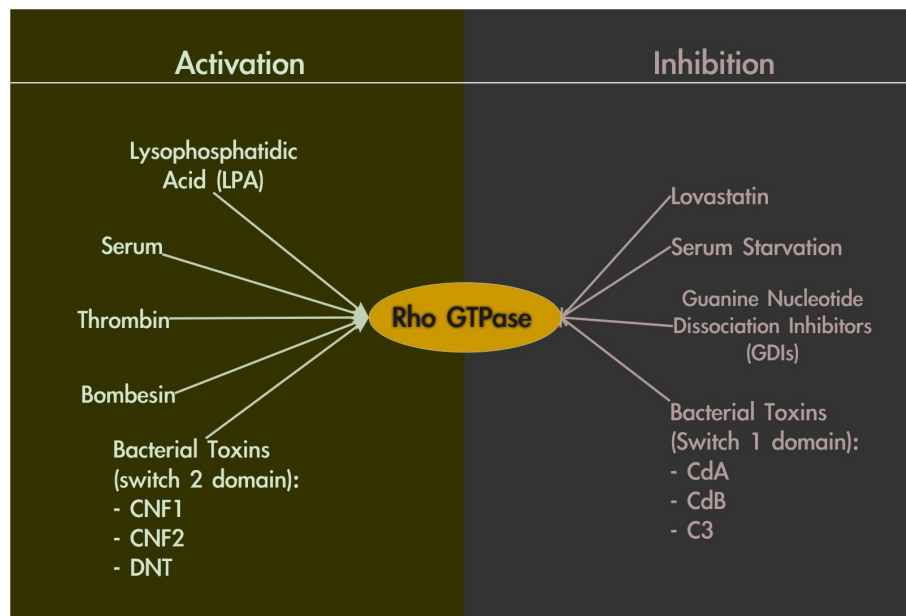


Figure 1.4: An overview of some of the activators or inhibitors of the RhoA GTPase.

the types and combinations of different integrin α and β subunits that compose the heterodimeric integrin molecules, which depend upon the cell type, the composition and rigidity of the ECM, on the migration status of the cell (migratory or stationary) and on the type of adhesion [29, 79].

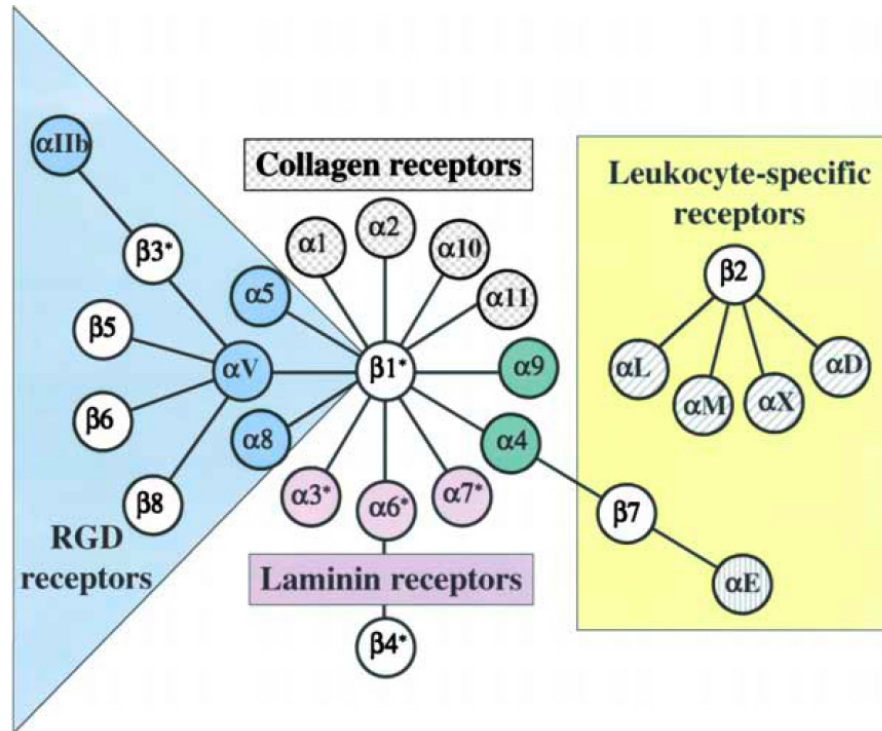


Figure 1.5: A compilation of various α and β subunits that make up different types of integrin heterodimers specific for either RGD receptors (this includes fibronectin), collagen, laminin or leukocyte-specific receptors (from [29]).

RhoA GTPase initiated contractile actomyosin-based force originating in the actin cytoskeleton is transmitted via integrins to the ECM. However, the reverse may also occur, where external force is conveyed via adhesions to the cellular cytoskeleton. This might for instance take place when endothelial cells are exposed to shear stress generated by blood flow and to the associated hydrostatic pressure. From this functional perspective, FA sites have been described as sites of force application and as mechano-sensing structures [7, 95]. The small, point-shaped adhesion sites located at the edges of lamellipodia are referred to as focal complexes. A further class are the tensin-enriched fibrillar adhesions involved in fibrillogenesis. Lastly, larger, $3-10\mu m$

long structures, at which the cytoskeleton exerts force through actomyosin-based contraction that underlies the control of RhoA GTPase, are called focal adhesions (FAs) [66]. The size of FAs has been correlated to the amount of force that is exerted upon them. In fact, there is a proportional relationship between the amount of force transmitted through a focal adhesion site and its size [7].

Fibronectin (Fn), laminin and collagen are major components of the ECM and influence cell adhesion, proliferation, differentiation and wound healing [29]. Fn, which was of most concern to this study, is a 440 kDa protein. Fn is a dimer composed of two globular subunits linked via disulfide bonds at the C-termini in its soluble form. As such, it does not react with other ECM proteins and does not self-assemble. These events do take place once integrin molecules bind to the asparagine-glycine-aspartate (RGD) domain of Fn, which then causes unfolding and self-assembly into fibrillar Fn structures, which represent its biologically active form [3, 4, 16].

1.2 Visualizing biochemistry and biophysics at the subcellular level

The aim of this study was to develop two optical biosensors on the basis of the photophysical phenomenon of the Förster resonance energy transfer (FRET) and which are optimized for the investigation of the concomitant biochemical and mechanical signaling involved in cell adhesion, migration and establishment of cell morphology [10, 21, 53, 82, 83]. FRET is based on the non-radiative energy transfer between compatible donor and acceptor fluorochromes. The efficiency of this energy transfer is mainly dependent on the inverse sixth power of the donor-acceptor separation distance (figure 1.6A), their respective transition dipole orientations (figure 1.6B) and the required overlap between the donor emission and acceptor excitation spectra. The distance at which FRET occurs (up to 70\AA [82]) coincides with the average protein diameter and indicates protein interaction. Conversely, at any greater dis-

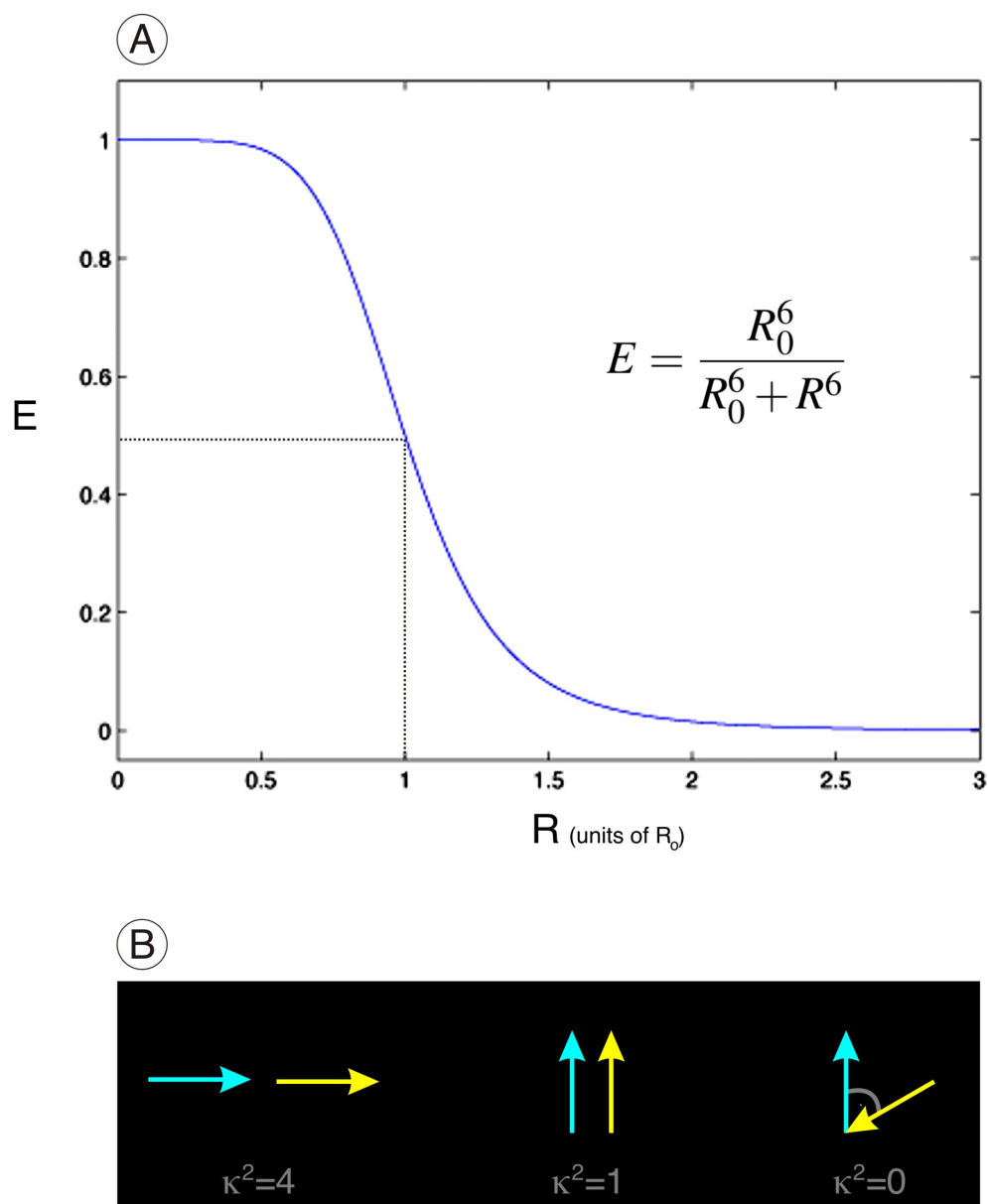


Figure 1.6: FRET efficiency is highly dependent on the distance (A) and the dipole orientation (B) between the donor and acceptor fluorochrome. The distance dependency is described by the equation in A, where E represents the FRET efficiency, R the distance between the acceptor- and donor-fluorochrome and R_0 the distance at which $E = 50\%$. The resonance energy transfer is further dependent on κ^2 (B), which describes the angle between the emission transition dipole of the donor and the absorption transition dipole of the acceptor [40].

tance FRET is practically absent. Past studies have shown that modification of proteins with FRET-compatible dyes, as well as the advent of chimeras consisting of a polypeptide of interest and FRET-compatible visually fluorescent proteins (VFPs), is applicable toward the elucidation of protein-protein interactions and protein conformational changes via FRET. A common application of FRET for the study of protein behavior is through the construction of a chimera in which a protein-binding domain is sandwiched between two FRET-compatible VFPs [10, 51, 102]. However, without the precise crystal structural information it is presently not possible to optimize the coordination of fluorochromes for the best possible intramolecular FRET, along with the maximal dynamic detection range of such a biosensor construct. For this reason, scientists resort to the laborious process of constructing several randomly linked versions, in the hope to identify one in which the highest FRET-based detection sensitivity has been achieved [74]. The work presented in this dissertation introduces a rational approach for the design of such a molecule.

1.3 Linear Extensions for Good Orientation

A set of intra-molecular FRET biosensors were created that thoroughly sample different dipole orientations and distances between the donor and acceptor VFPs. To achieve this, a series of unusually stable α helices [47], which differ in the number of amino acids, were inserted between the VFP FRET pair ECFP and Venus. Every sequential amino acid addition elicited a 100° turn of the α helix, thus enabling a controlled change in the ECFP transition dipole orientation with respect to that of Venus. Furthermore, the amino acid addition resulted in a controlled $0.15nm$ incremental increase in the α helical length [47, 90], thus allowing for simultaneous sampling of the effect of increased distance between the VFPs at a rate that is below the $R_o^1 = 5nm$ distance for ECFP-EYFP [27]. This set of α helix-based modifications

¹ R_o is the distance at which the FRET efficiency between randomly oriented donor and acceptor VFPs is 50%

was designated as LEGO (Linear Extensions for Good Orientation).

The small GTPase Rho plays a key role when cells need to generate mechanical force required for the maintenance of cytoplasmic tension or cell morphology, division, adhesion or migration [26]. To monitor activity of the RhoA GTPase, the Rho-binding domain (RBD) of Rhotekin was inserted between the two VFPs in the intramolecular FRET biosensor described above. This downstream effector binds active, GTP-bound RhoA and thereby reduces the intrinsic and GAP-enhanced GTPase activity of Rho [58,60,102]. The Rhotekin RBD has been previously applied for detection of Rho activity [60,102]. In the context of the LEGO-based design approach of a FRET biosensor, this RBD was successfully applied to generate a FRET biosensor optimized for the highest sensitivity toward RhoA activity. Thus, an improved version of a RhoA based biosensor was created that reports on the biochemical signaling leading up to mechanical force generation within the actin cytoskeleton.

1.4 The FRETing Matrix

For motility to occur, cells need to coordinate assembly and disassembly of contacts with the ECM (focal adhesions, focal complexes), which are pivotal for the generation of force and traction. To better understand the dynamics of focal complex formation and their migration in time, an ECM consisting of fluorescently labeled Fn was generated. The fluorescent labels were chosen to operate as a donor-acceptor FRET pair, thus creating a FRETing Matrix. The FRETing matrix was used to visualize areas at which cells, through RhoA dependent, force-induced rearrangements, modify the Fn-ECM structure, which includes sites proximal to focal adhesions and stress fibers. The FRETing Matrix technique was established as a continuous imaging force-biosensor that faithfully reports the dynamic interaction of cells with their Fn environment.

Taken together, the LEGO and FRETing Matrix biosensors provided detailed insight into the spatio-temporal regulation of morphological changes during cell spreading, adhesion and migration from the perspective of the RhoA GTPase activity status and mechanical forces exerted onto the ECM.

Chapter 2

Methods

2.1 Linear Extensions for Good Orientation (LEGO)

2.1.1 Design Strategy

A set of eleven differing DNA vectors was generated, whose purpose was to eventually be expressed in mammalian adhering cells, resulting in molecules that optically report on the RhoA GTPase activity by means of the Förster resonance energy transfer (FRET). Since the RhoA GTPase is involved in the biochemical signaling that controls stress fiber dynamics, this set of molecules would then represent FRET biosensors for intracellular force. Additionally, these molecules simultaneously sample the FRET efficiency at different donor-acceptor distances and at different dipole orientations between the donor and acceptor fluorochrome. Therefore, this set of molecules introduces a new, rationalized approach toward designing the one FRET biosensor with the highest sensitivity and dynamic range within which it reports on the RhoA GTPase activity.

The two visible fluorescent proteins (VFPs) ECFP and Venus were cloned in tandem to generate a DNA vector encoding a single molecule construct in which they would serve as the FRET-donor and FRET-acceptor, respectively. In-between, the Rho-binding domain of Rhotekin [58] (RBD, amino acids 7 – 82) was placed immediately

3' to ECFP. At this stage, the resulting construct resembles *Raichu-RBD* [102] shown in figure 2.1, which was published while the LEGO project was ongoing. DNA encoding an α helix [47] was placed between the RBD and Venus. The resulting

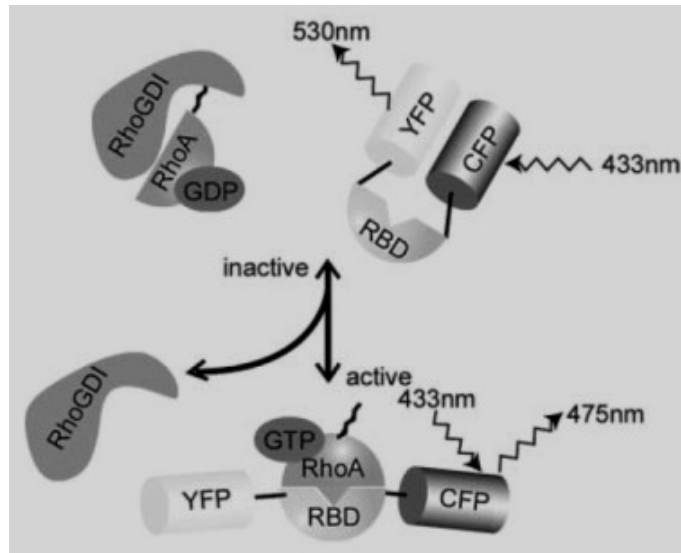


Figure 2.1: A schematic view of *Raichu-RBD* a single-molecule RhoGTPase FRET biosensor (from [102]).

construct was then replicated eleven times, such that the only varying feature within the eleven constructs was the addition of one amino acid as shown in figure 2.2.

The purpose of prolonging the α helix by one amino acid is to simultaneously increase its length by $0.15nm$ and to also change the orientation between the N- and C-terminus of the alpha helix by 100° [90]. This change in length and orientation would be propagated to the entire single-molecule construct, thereby changing the distance and orientation between the donor and acceptor dipoles.

2.1.2 The FRET-acceptor: pVenus-N1

Add-on polymerase chain reaction (PCR)¹ was performed using the DNA vector Venus/pCS2 as the template (kindly provided by Dr. Takeharu Nagai, RIKEN In-

¹PCR protocol is on page 28

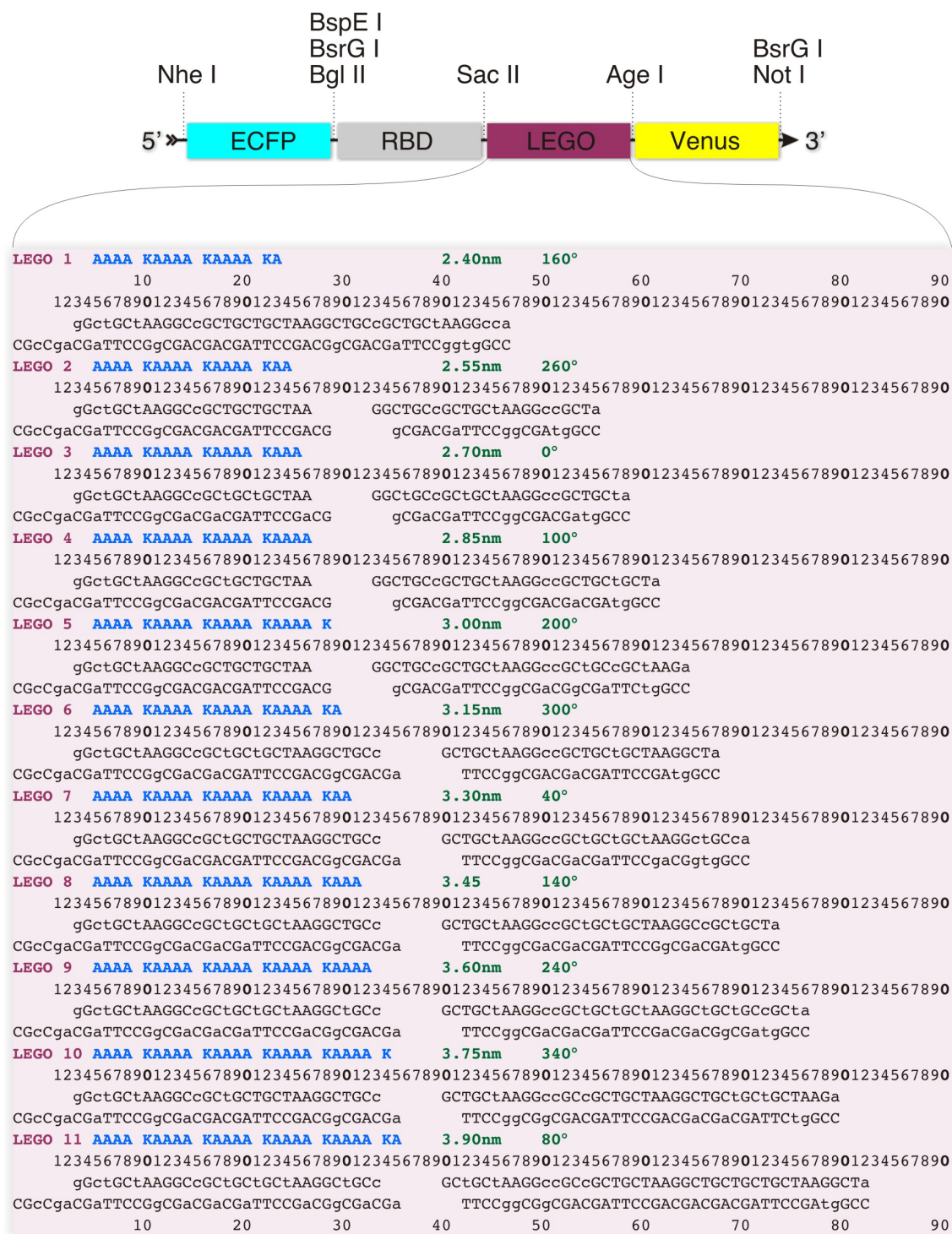


Figure 2.2: The top of the graphic displays the sequence in which ECFP, Rho-binding domain (RBD), α helix (LEGO) and Venus were cloned for each of the eleven LEGO constructs, along with the corresponding enzymatic restriction sites. Below, shown in the 5' - 3' orientation, are the sense and anti-sense strands used to create the different segments encoding the α helices. Emphasized in blue is the predicted resulting amino acid sequence, while in green the corresponding increase in length of the alpha helix is shown, as well as the new resulting angle between the last and the first residue of the alpha helix.

stitute, Japan) and forward (Ven_{FW}) and reverse (Ven_{RV}) primers² so that Age I and Not I restriction sites were added to the 3' and 5' end of the amplicon, respectively. The resulting fragment was purified with a MinElute® PCR purification kit, digested with Age I and Not I and gel-extracted³ with a MinElute® gel extraction kit by following manufacturer instructions (both kits were from QIAGEN, Hilden, Germany). Simultaneously, pEYFP-N1 (BD Biosciences, Clontech, Heidelberg, Germany) was also digested with Age I and Not I, yielding a larger 4kb fragment. The 4kb fragment and the Venus amplicon were ligated⁴ to create pVenus-N1, which retained the same multiple cloning site (MCS) as pEYFP-N1. The ligation product was transformed⁵ into chemically competent bacteria.

2.1.3 The FRET-donor: pECFP-C1 modification

The vector encoding the FRET donor, pECFP-C1 (BD Biosciences, Clontech, Heidelberg, Germany), was modified by removing the Age I site located at base pair 601. In this manner subsequent inclusion of the α helix-coding sequence (flanked by Sac II and Age I) or possible future replacement of the Venus-encoding region (flanked by Age I and Not I) in the final construct (top of figure 2.2) would still be possible through the use of restriction enzyme combinations involving Age I. Essentially, pECFP-C1 was digested with Age I, which was then followed up by treatment with the Klenow⁶ fragment (Roche Molecular Biochemicals, Mannheim, Germany) to generate blunt ends and finalized by self-ligation. The ECFP encoding DNA lacking the Age I restriction site was then cloned into pVenus-N1, resulting in pECFP-Venus.

²Primers are shown on page 28

³The gel-extraction method is described on page 30.

⁴Refer to the ligation protocol on page 30.

⁵Refer to transformation protocol on page 31

⁶Treatment with the Klenow fragment is described on page 29

2.1.4 Alpha-helix encoding fragments

Based on the α helix described by [47] the Wisconsin Package (Version 10.3, Accelrys Inc., San Diego, USA) was used to generate the α helix encoding fragments shown in figure 2.2. To prevent synthesis errors or formation of secondary structures the fragments were split as shown in figure 2.2. In a further attempt to prevent secondary structure formation, information gained about the predicted secondary structure by the MFold program [107] of the Wisconsin Package was taken into consideration when deciding on the final sequence, while still maintaining the amino acid sequence outlined by [47]. The final sense and anti-sense fragments were synthesized by MWG Biotech AG (Ebersberg, Germany). After ligation of the appropriate fragments (see figure 2.2), the ligation products and pECFP-Venus were digested with Sac II and Age I. In a final step the purified digestion products were used to create eleven constructs, one for each α helix encoding region, to yield pECFP- α helix(1...11)-Venus.

2.1.5 Rho-binding domain of Rhotekin

The Rho-binding domain of Rhotekin (GenBank accession number U54638) was amplified from the vector GST-Rhotekin HR1 (kindly provided by Dr. Harry Mellor, University of Bristol, Bristol, UK) using primers RBD_{FW} and RBD_{RV}⁷. During the amplification step the Bgl II and Sac II restriction sites were added to the amplicon at the 5' and 3' end, respectively. Prior to ligation into the final destination constructs, the amplicon was purified, double digested with Bgl II and Sac II and gel extracted. The resulting series of 11 vectors were of the sequence pECFP-RBD- α helix(1...11)-Venus and are referred from hereon as LEGO1-11. The entire cloning strategy leading up to the final LEGO constructs is outlined in figure 2.3.

⁷Primers are shown on page 28

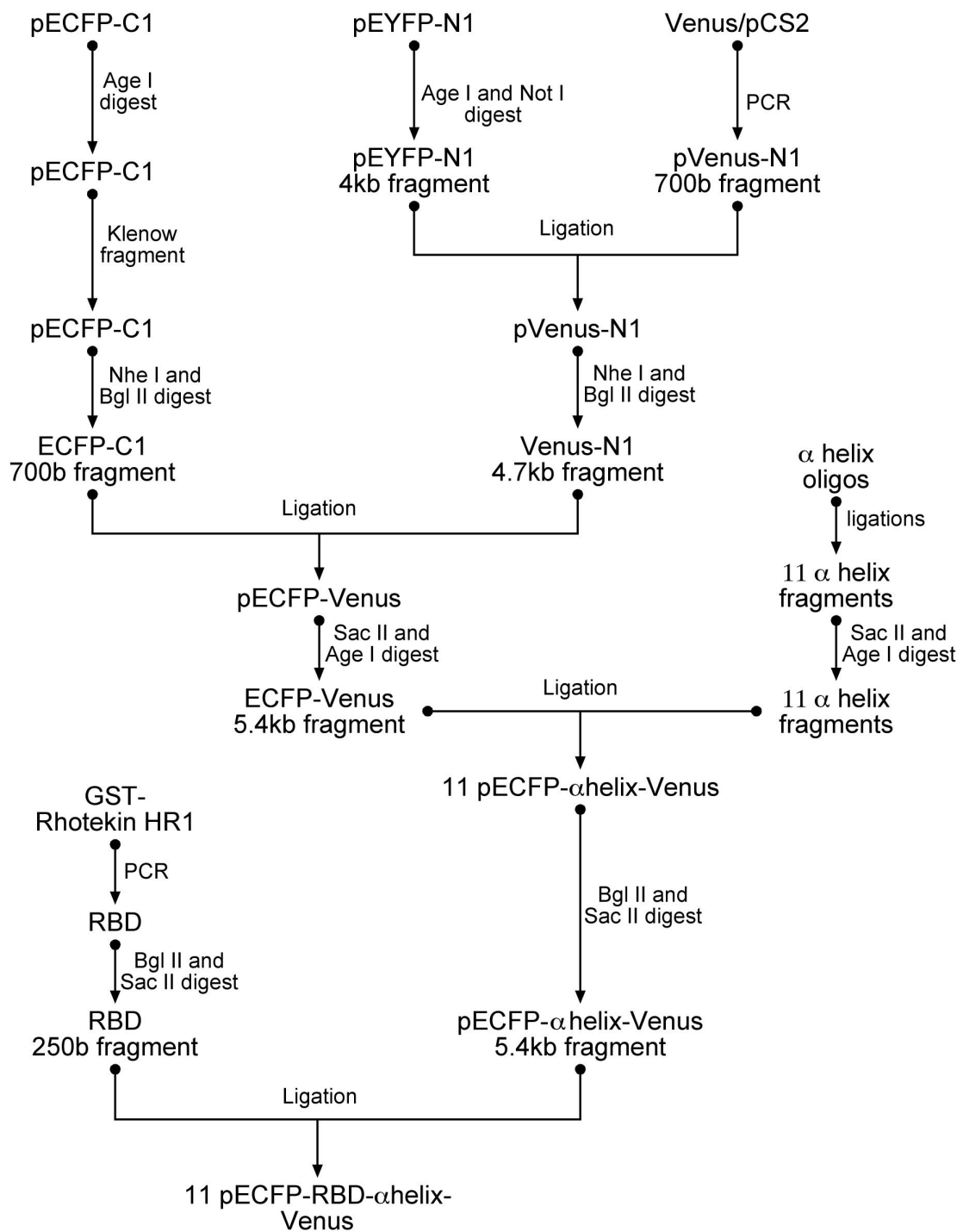


Figure 2.3: Workflow outlining the cloning strategy used to generate the eleven LEGO constructs.

2.1.6 Flow Cytometry

In preparation for flow cytometry experiments, HeLaSS6 cells were grown in 6-well plates to near confluency and transfected with the respective construct combination. After an expression-time of 18 – 24hrs, the cells were detached through trypsinization and analyzed using the BD FACSAria (BD Biosciences, Heidelberg, Germany) flow cytometer. First, viable cells were selected (population P1) as shown in figure 3.9 based on side light scatter (SSC) and forward light scatter (FSC) information obtained from untransfected cells. Then, cells transfected with either ECFP or Venus were measured (figure 3.9C and D) using the filter setup outlined in table 2.1. Finally, the *BD FACSDiva* software was used to compensate the fluorochrome emissions so that the ECFP emission could be successfully separated from the Venus emission [67,89]. The resulting compensation settings were then applied to all subsequent measurements of cells expressing the respective LEGO constructs. The relative

FACS ANALYSIS EXCITATION/EMISSION FILTER SETUP			
Channel name	Excitation (λ_{ex})	Emission (λ_{em})	Long pass filter
Venus violet-A	407nm	545 – 625nm	526nm
Venus blue-A	488nm	500 – 560nm	502nm
CFP-A	407nm	410 – 490nm	none

Table 2.1: Measurement and analysis setup of flow cytometry experiments.

FRET efficiency was calculated using the *ReFlex* software package [17], whose algorithm is based on equations described in [85,88]. Based on acceptor photobleaching (APB) experiments on adherent cells expressing LEGO constructs, a FRET efficiency between 25 – 30% was estimated (figure 3.3). The factor “ α ” of equation 4 listed in [85] was chosen so that the estimated FRET efficiencies would fall within this range. Therefore, the absolute values obtained with the ReFlex software do not represent precise FRET efficiencies. Instead, the obtained values are regarded as relative FRET efficiencies, which can nonetheless be used to quantitatively compare the difference in FRET efficiency exhibited by the various LEGO constructs. A more detailed description of the ReFlex software and how it was applied can be found in

the *Protocols* section on page 32.

2.2 FRETing Matrix

2.2.1 Fibronectin labeling and subsequent coating of glass coverslips

While reporting on the biochemical signaling leading up to the generation of intracellular force within the cytoskeleton was the objective of the LEGO project, the FRETing Matrix was designed to report on the force that cells exert on the extracellular environment, the extracellular matrix (ECM). Fibronectin (Fn) is an ECM protein that plays a pivotal role in cell adhesion during cell spreading and migration. Different structural domains of this dimeric protein, including the RGD integrin binding domain, are outlined in figure 2.4. The motivation for labeling Fn

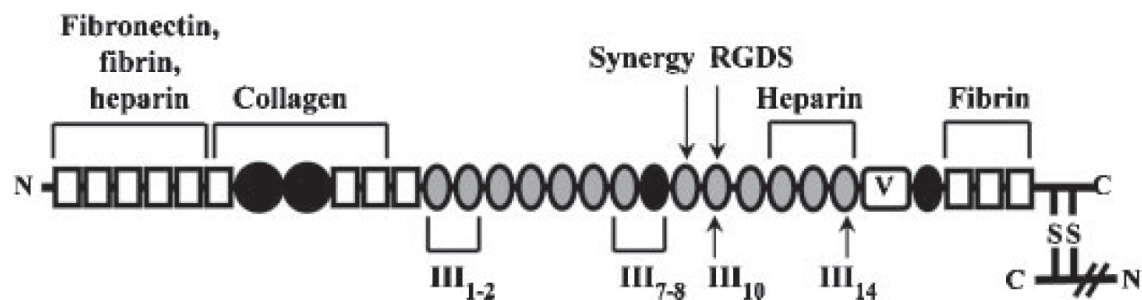


Figure 2.4: A schematic representation of the functional domains of fibronectin. The integrin binding sites are indicated by arrows. Fibronectin molecules are present as dimers through the formation of disulfide bridges at their C-termini (figure adapted from [91])

is outlined in figure 2.5. Essentially, a homogeneously mixed coating solution containing separately labeled Cy3- and Cy5-conjugated Fn would generate an ECM coat on a glass surface that would then exhibit FRET, which would be of the same efficiency throughout the entire coat. However, once cells adhere to the labeled Fn via their integrin molecules, they would reorganize the Fn, which would cause a change of the intermolecular distance between the FRET donor (Cy3) and FRET acceptor (Cy5) molecules. As a consequence, local changes in FRET efficiency would then become visible. Integrin molecules are clustered at cellular adhesion sites, from

which force-transducing stress fibers emanate. Overall, this principle was tested and proven in similar manner by Kong et al. [39] while the FRETing Matrix experiments were ongoing.

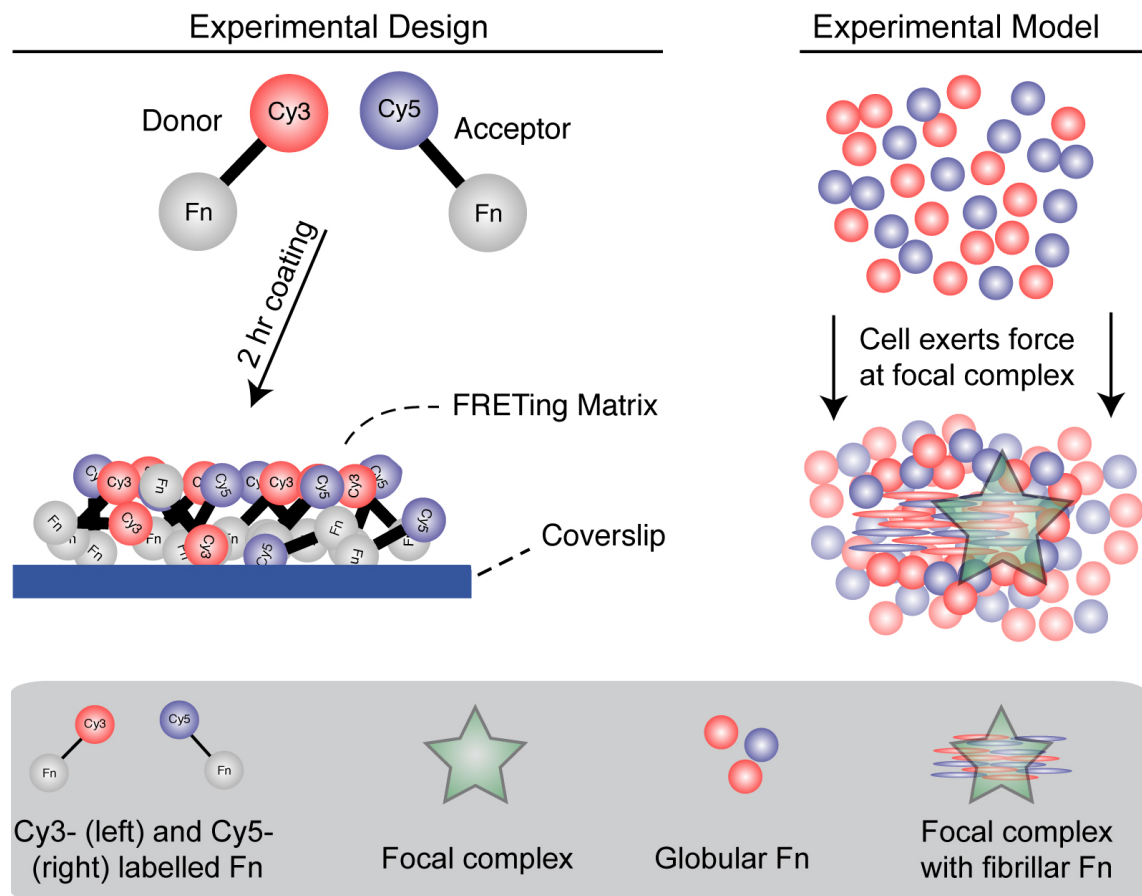


Figure 2.5: Schematic of the experimental design for creating a fibronectin-based FRETing Matrix and the proposed biosensing mechanism.

The suspension of bovine Fn obtained from Sigma (Sigma, Seelze, Germany) contained $0.05M$ Tris, which is a source of primary amino groups that would compete with the free amino groups of Fn for the amino-reactive Cy3 or Cy5 dye during the labeling process. Therefore the Fn was dialyzed in two subsequent steps (step 1=2hrs, step 2=over-night) with $2L$ PBS at $4^{\circ}C$ using a dialysis cassette (Slide-A-Lyzer 10K, PIERCE, Bonn, Germany). The new concentration of the dialyzed Fn was determined based on the resulting volume and used for subsequent calculations. The dialyzed Fn was then buffered to pH 8.5 and $100mM$ bicine (Sigma, Seelze, Germany). A 10-fold molar excess of Cy3 or Cy5 (GE Amersham Biosciences, Freiburg,

Germany) amino reactive dye was added to separate aliquots of the dialyzed, bicine-buffered Fn. This labeling reaction was allowed to proceed for 30 minutes at room temperature, after which it was quenched by lowering the pH and introducing free amino groups through addition of 1M Tris pH 7.5 (final Tris concentration was then 0.05M). The Fn was kept sterile at all times and with the exception of the 30 minute labeling window at room temperature it was kept cold on ice. Further care was taken not to vigorously shake or re-suspend the Fn-solution. The two differently labeled Fn solutions were then wrapped in aluminum foil and stored at 4 – 8°C. In this state the labeled Fn was usable for approximately 3 weeks.

To generate a FRETing Matrix on a glass coverslip, the Cy3 and Cy5-labeled Fn was combined at a ratio of 1:2 and dissolved in the imaging buffer (refer to table 2.8) so that the final coating occurred at a Fn concentration of $10 \frac{\mu\text{g}}{\text{ml}}$ for 2hrs. This coating concentration and the 1:2 Fn^{Cy3}:Fn^{Cy5} ratio were experimentally determined to yield a FRET efficiency within the FRETing Matrix of approximately 50% (also see figure 3.16). Unreacted dye was removed from the FRETing Matrix preparation by washing with imaging buffer.

2.3 Imaging of live and fixed samples

All microscopic imaging was performed on a Leica (Leica, Heidelberg, Germany) TCS confocal laser scanning microscope (CLSM) equipped with a 63x (1.32NA) objective. This CLSM was further equipped with an acousto-optical beam splitter (AOBS) module, which enabled free choice of the size and position of the desired emission window. For each experiment, care was taken to reduce bleaching, unless it was desired as in the case of acceptor photobleaching. This was achieved by creating a balance between sample emission and laser power, photo-multiplier (PMT) voltage, beam expander choice, scan velocity, frame or line averaging settings. These parameters, with the exception of the laser power, remained unchanged once they

were established at the onset of a particular experiment. Furthermore, once the parameters were set, the offset of each PMT in usage was adjusted so that hardly any underexposed pixels were present at 0% laser power. Lastly, images for each channel in use were recorded, while keeping the laser power at 0% to determine the “dark current”, which was later subtracted from the respective emissions.

2.3.1 Lambda scan of LEGO and the FRETing Matrix

λ scans were performed to verify the presence of the respective fluorochrome or chemical dye peaks in the LEGO or FRETing Matrix experiments, respectively. A serial scan was setup as described in table 2.2. In particular, a 10nm-wide emission window migrated from the indicated start to finish wavelength. Care was taken to reduce bleaching by keeping the laser intensity as low as possible, while still collecting sufficient signal.

Experiment	$\lambda_{excitation}$	$\lambda_{emission}$	
		start	finish
LEGO	405nm	438nm	608nm
FRETing Matrix	543nm	558nm	703nm

Table 2.2: Lambda scan settings used for the LEGO and FRETing Matrix experiments.

2.3.2 Live-cell imaging

Live cell imaging was performed for cell-spreading (figure 3.20) and cell-migration (figure 3.24) experiments. For this purpose a heated, closed chamber was used (Focht live cell (FCS2) chamber, Bioptechs, Butler, PA, USA), which required usage of 40 mm diameter coverslips (Hecht-Assistent, Sondheim, Germany). This chamber provides a key advantage in that it heats the sample evenly so that less optical disturbances occur due to potential change in the refractive index of portions of medium of different temperature.

2.3.3 Interference reflection microscopy

Interference reflection microscopy (IRM) was used to visualize areas of close contact between a cell and the surface upon which it grows [1, 14, 15, 65, 66]. Figure 2.6 illustrates the theory behind IRM. This method relies on the property by which cell features that are closer to the adhesion surface will produce lightwaves that reflect in a destructive manner, effectively canceling each other out the closer to each they are. Figure 2.7 shows four successive frames of a migrating cell (downward) recorded in

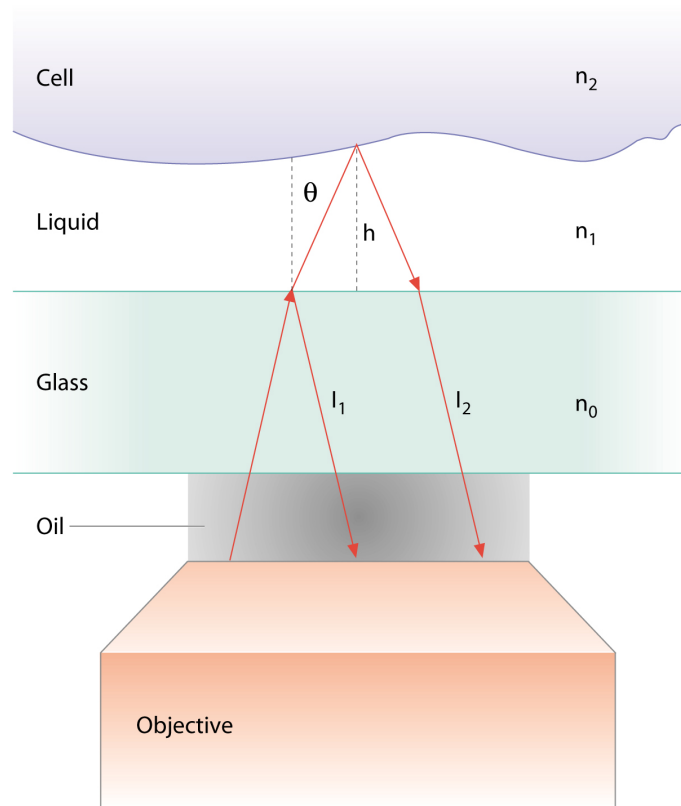


Figure 2.6: Interference Reflection Microscopy (IRM). As a light beam passes through media of different refractive indices beams I_1 and I_2 are generated, which interfere with each other (shown as modified version of [1]). The interference is more pronounced when the distance between the cell and the glass surface is small.

IRM mode. What appear at first as dark areas, are regions that still remain attached, even though the main body of the cell has moved on (triangles).

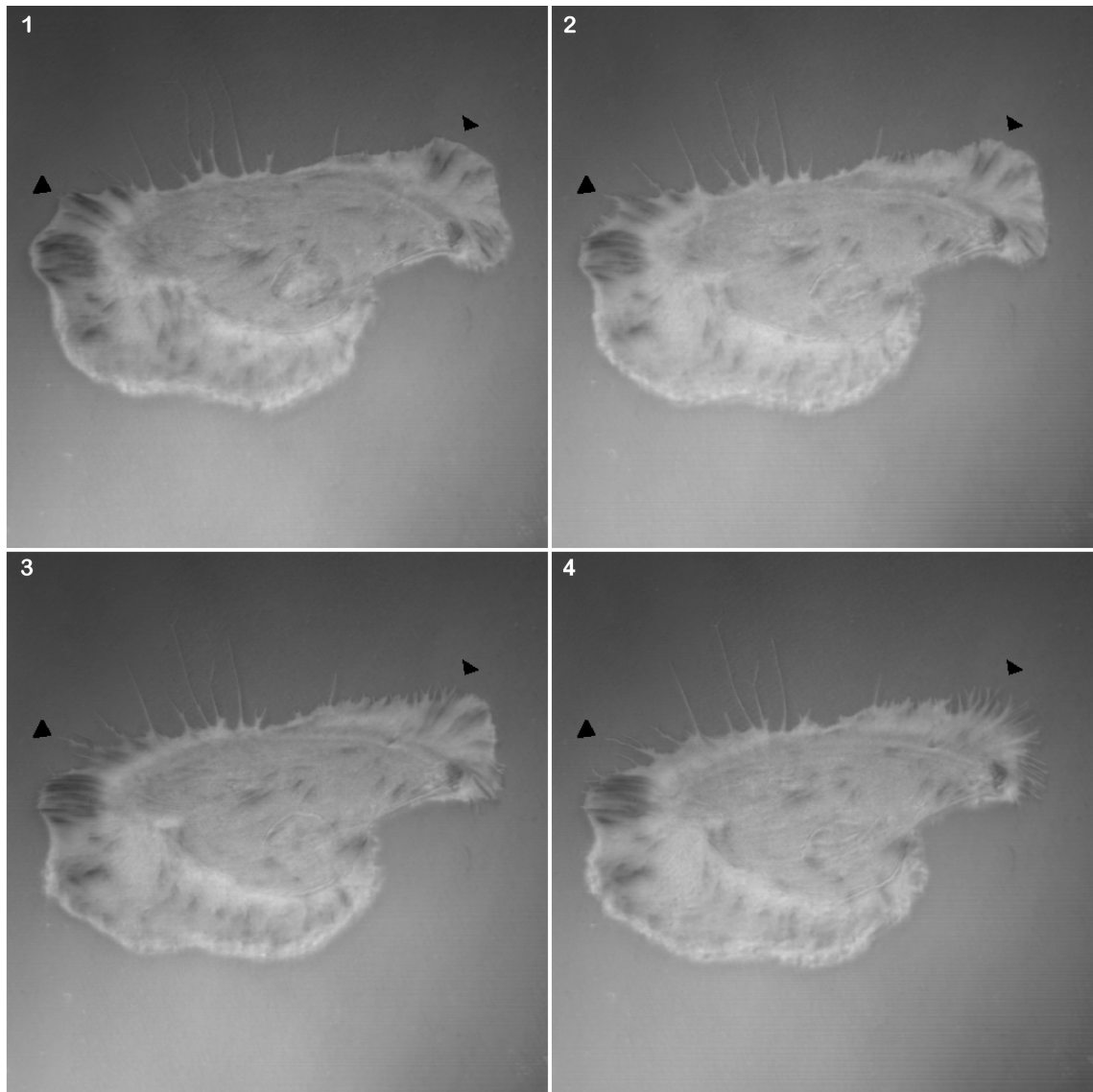


Figure 2.7: IRM can be applied to study cell adhesion dynamics during migration. The black triangles point out adhesion sites (dark areas), which, as the cell moves downward, remain attached.

2.3.4 Image Analysis

Analysis of images obtained with the Leica CLSM was conducted using Matlab (The MathWorks GmbH, Aachen, Germany) or ImageJ (<http://rsb.info.nih.gov/ij/>). In particular, a script was created within Matlab, which automated the calculation of the Venus/ECFP ratio of any number of recordings (ECFP and corresponding Venus sensitized emissions) located within one computer subdirectory. Furthermore, a cumulative histogram was created, which represented the frequency versus intensity distribution of all ratios of the images used for the calculation (i.e. for a particular LEGO construct). The values of the histogram were imported into the GraphPad Prism 4 (<http://www.graphpad.com/prism/Prism.htm>) software and a Gaussian distribution was modeled to determine the location of the mean ratio and the standard deviation thereof. The standard error was then determined by dividing the standard deviation by the square root of the the number of cells measured per LEGO construct (also refer to figure 3.6).

ImageJ was used when working with sequential images to generate image stacks, movies or montages that represented acceptor/donor emission ratios or when calculations were conducted to estimate the FRET efficiency after acceptor photobleaching. In particular, when working with LEGO recordings (can also be applied to the FRETing Matrix) the color table of images was changed to jet (the jet color table is exemplified in figure 3.16) and images were converted to 32 bit. Then a gaussian blur with a radius of 2 pixels was applied. The sensitized emission image was thresholded so that all values beneath the threshold were defined as “not-a-number” (NaN) and were no longer used for subsequent calculations. In this manner a mask was generated for each specific cell. At this point the sensitized emission was divided by the donor emission to yield the ratio. The color table was then adjusted so that the minimum and maximum value for all calculated ratios was the same.

2.4 Cell lines

The cell lines used were B16F1, B16F1 cells stably transfected with GFP-actin, HeLa SS6, NIH-3T3 (DSMZ #: ACC59) and RMCD. The HeLa SS6 and RMCD cell lines were kindly provided by Prof. Mary Osborn (Max-Planck-Institut für biophysikalische Chemie, Göttingen, Germany) and both B16F1 lines by Prof. Beat Imhof (University of Geneva, Geneva, Switzerland). All cell lines were maintained at 37°C and 5% CO₂ and were grown in Dulbecco's modified Eagle's medium (DMEM, GIBCO Invitrogen, Karlsruhe, Germany), supplemented with 10% FCS (PAA Laboratories, Linz, Austria), 100 U/mL penicillin and 100 µg/mL streptomycin (both from Sigma, Seelze, Germany). To ensure continuity of the stable transfection, the B16F1 cell line expressing GFP-actin was maintained in medium containing 1.5 mg/mL G418 (GIBCO Invitrogen, Karlsruhe, Germany).

2.5 Transfection of DNA vectors into adherent cells

Transient transfections were performed using Lipofectamine 2000 (Invitrogen, Karlsruhe, Germany) and following manufacturer directions. Depending on whether the cells were intended to be used for microscopy or flow cytometry, they were transfected at 50% or 80% confluency, respectively. Cells slated for microscopy were grown on glass-coverslips in 24-well plates, while those slated for flow cytometry in 6-well plates (both by Nunc, Wiesbaden, Germany). Prior to transfection, the cell culture medium was exchanged. After a 4hr incubation period with the transfection reagent, the cells were washed and the medium was exchanged once again. An 18 – 24hr period followed, during which the cells were allowed to express the respective constructs and after which they were fixed (see part of phalloidin stain on page 34) for microscopy or trypsinized for flow cytometry. A 1:1.25 DNA (µg) to Lipofectamine 2000 (µL) transfection ratio was maintained. Furthermore, for the LEGO

experiments, a 1:2 ratio between DNA encoding the respective LEGO construct and RhoA_{T19N} or RhoA_{G14V} was maintained.

2.6 Protocols

2.6.1 Primers

Listed below are primers used in addition to those listed in figure 2.2, arranged according to the respective DNA fragment that was amplified or sequenced:

- Venus
 - Ven_{FW}: 5' -cggccaccggtatggtgagcaagggcgaggagctgt- 3'
 - Ven_{RV}: 5' -agctgtacaagtaaagcggccgactcg- 3'
- Rho binding domain of Rhotekin (GenBank accession code: U54638)
 - RBD_{FW}: 5' -GATCGATAGATCTATCCTGGAGGACCTCAATATGCT- 3'
 - RBD_{RV}: 5' -CAGGTGCTGGAGAAGACAGGCGCCGCGGTCGATC- 3'
- EGFP: used for sequencing ECFP and Venus
 - EGFP_{FW} 5' -CAACGGGACTTTCCAAAATG= 3'
 - EGFP_{RV} 5' -AGCTGCAATAAACAAGTT- 3'

All primers were synthesized by MWG-Biotech AG, Ebersberg, Germany.

2.6.2 PCR

For the polymerase chain reaction the enzymes Pfu polymerase (Stratagene, La Jolla, CA, USA) or Deep Vent polymerase (New England BioLabs, Inc., Frankfurt, Germany) were used. Depending on the enzyme, size of the expected amplicon and the primers, the elongation temperature and time and the annealing temperature had to be adjusted. dNTPs used were from Roche Diagnostics GmbH (Roche Diagnostics GmbH, Mannheim, Germany). The individual steps and settings of a typical PCR are shown in table 2.3. During the PCR a 1 – 1.5% agarose gel was prepared (the percentage depended on the size of the amplicon) on which the PCR product was run and analyzed (also see page 30). All PCR products were sequenced (using

primers shown in page 28) after they were ligated into their respective vectors, due to the possibility of errors occurring during a PCR.

Description	PCR cycle step #	Time	Temperature
Initial Denaturation Step		5 min	95°C
Denaturation	1	30 sec	95°C
Annealing	2	30 sec	57°C
Elongation	3	1 min	72°C
Final Elongation Step		10 min	72°C

Table 2.3: A generic setup that functioned as a starting point for the various PCRs performed (also see figure 2.3).

2.6.3 Restriction Digest

The enzymes Nhe I, Bgl II, Sac II, Age I (PinA I) and Not I, as well as the respective reaction buffers, were purchased from Roche Diagnostics GmbH (Roche Diagnostics GmbH, Mannheim, Germany). A general setup for a respective digest is outlined in table 2.4. Care had to be taken to select the correct buffer which enabled optimal function of the single or multiple restriction enzymes when conducting a single or multiple digest. After 1hr incubation at 37°C, the digestion products were gel-purified as outlined on page 30.

Component	Final concentration
DNA	1 μ g
Buffer (10x)	2.5 μ L
Restriction enzyme	1 unit
Water	Up to final volume of 25 μ L

Table 2.4: A typical restriction digest setup.

2.6.4 Klenow fragment treatment

As explained previously on page 16, it was necessary to remove the Age I restriction site in pECFP-N1. In practice, this was done by first digesting the plasmid with the Age I restriction endonuclease, which produced sticky ends. The Klenow fragment,

which is the large fragment of DNA polymerase I, catalyzes mononucleotide addition in the 5' - 3' direction and was used to fill in the sticky ends produced by the Age I digest. A typical Klenow treatment setup is shown in table 2.5. Following a 15 minute incubation at 37°C, the Klenow fragment was heat-inactivated at 75°C for 10 minutes. Lastly, the blunt ends were ligated in a setup as shown in table 2.6.

Component	Final concentration
DNA	1 μ g
Buffer(10x)	2 μ L
Klenow fragment	1 unit
dNTPs	0.5 μ L (Each dNTP is 10mM)
Water	Up to a final volume of 20 μ L

Table 2.5: Setup used for incubation with the Klenow fragment.

2.6.5 Ligation

After various restriction digests, PCR or Klenow fragment treatments, the DNA was ligated using the T4 DNA Ligase (Roche Diagnostics GmbH, Mannheim, Germany). The general setup is shown in table 2.6. A successful ligation was usually obtained after a 30 minute incubation at room temperature.

Component	Final concentration
DNA	up to 1 μ g
Buffer(10x)	2 μ L
T4 DNA ligase	5 units
Water	Up to a final volume of 20 μ L

Table 2.6: Setup used for DNA ligation.

2.6.6 Gel-extraction

DNA obtained from a restriction digest or PCR was isolated via a gel-purification procedure. Depending on the size of the fragment to be isolated, a 1 – 1.5% gel was prepared. 0.5 – 0.75g of agarose (Sea Kem LE Agarose, Cambrex, Verviers, Belgium) were added to 50mL TBE buffer and dissolved by heating. GelStar (Cambrex,

Verviers, Belgium) was added to the agarose-TBE suspension to visualize the DNA being separated. It is important to note that GelStar was added prior to DNA separation as this yielded better results. The retardation of DNA migration by GelStar within the gel was negligible when the amount of DNA loaded was below 800ng. The bands of interest were identified by comparing them to a 1kb DNA ladder (PE-QGOLD 1kb DNA-Leiter, PEQLAB Biotechnologie GmbH, Erlangen, Germany), which was run in parallel. The band of interest was then cut out with a scalpel, weighed and the finally the DNA was isolated with a MinElute gel extraction kit (QIAGEN, Hilden, Germany) following the manufacturer directions.

2.6.7 Chemical transformation

A chemical transformation of BL21 chemically competent bacteria (Sigma, Seelze, Germany) was conducted when an existing or newly ligated plasmid needed to be amplified. The chemically competent cells were thawed on ice and 50 μ L thereof were aliquoted. 50-100ng DNA were added to the aliquoted bacteria, while keeping the samples on ice. The control transformations included ligations which were conducted without the presence of an insert. This preparation was then left on ice for 30 minutes, after which the bacteria were exposed to a 42°C heat shock lasting 1 minute and a subsequent 2 minute incubation on ice. 1mL of LB medium was then added and the bacterial cells were allowed to incubate at 37°C for 45 minutes. 150 μ L of the bacterial suspension were then plated on agar plates containing the appropriate selective antibiotic (all LEGO constructs encode kanamycin resistance). The agar plates were incubated over-night at 37°C. The following day, colonies were picked and grown over-night while shaking at 37°C. Finally, the over-night cultures were spun-down and the DNA was extracted with a MiniPrep kit (QIAGEN, Hilden, Germany).

2.6.8 The *ReFlex* software package

The *ReFlex* software package was used to calculate relative FRET efficiencies of all LEGO constructs expressed in HeLaSS6 cells. The cells were measured as described on page 19 and the results were exported with the *FACSDiva* software in flow cytometry standard (FCS) files of version 2.0. Several variables were then used for the FRET efficiency estimation by the *ReFlex* software, which is based on algorithms introduced in [88] and further applied in [85]. The equation array 2.1 lists the three different types of intensities detected from each sample, where λ_{exD} , λ_{exA} respectively refer to excitation of the donor or acceptor and λ_{emD} , λ_{emA} to the respective emission collected from the donor or the acceptor fluorochrome.

$$\begin{aligned} I_1(\lambda_{exD}, \lambda_{emD}) \\ I_2(\lambda_{exD}, \lambda_{emA}) \\ I_3(\lambda_{exA}, \lambda_{emA}) \end{aligned} \quad (2.1)$$

The wavelengths of the various λ_{ex} and λ_{em} are shown in table 2.1 on page 19. To account for the spectral bleed-through the S_1 and S_3 correction factors shown in equation 2.2 were calculated based on cells expressing only the donor fluorochrome (ECFP). Similarly, the S_2 and S_4 correction factors, also shown in equation 2.2, were determined using emission obtained from cells expressing the acceptor (Venus) only.

$$S_1 = \frac{I_2}{I_1}, S_3 = \frac{I_3}{I_1}, S_2 = \frac{I_2}{I_3}, S_4 = \frac{I_1}{I_3} \quad (2.2)$$

Intensity readings from untransfected cells were used to correct the background emission. With correction factors S_{1-4} in place, the three types of emission I_{1-3} obtained from cells expressing the LEGO constructs can then be described as shown in equation 2.3.

$$\begin{aligned} I_1 &= I_D(1 - E) + I_A S_4 + \frac{S_4}{S_2} I_D E \alpha \\ I_2 &= I_D(1 - E) S_1 + I_A S_2 + I_D E \alpha \\ I_3 &= I_D(1 - E) S_3 + I_A + \frac{S_3}{S_1} I_D E \alpha \end{aligned} \quad (2.3)$$

In equation 2.3 the quenched donor intensity is termed as I_D , while I_A describes the intensity of the directly excited acceptor. For I_1 only the first term was of interest, since the remaining part was zero due to the fact that no donor emission was obtained upon excitation of the acceptor in cells expressing only the acceptor, i.e. $S_4 = 0$. Furthermore, I_2 of equation 2.3, takes into account that aside from acceptor sensitized emission there are also the donor bleed-through and the emission of the directly excited acceptor fluorochrome. Lastly, I_3 contains emission that is generated upon direct excitation of the acceptor, which includes the donor “spill-over” into the acceptor emission, the acceptor emission due to its direct excitation and sensitized emission due to FRET. Combined, the three types of emission can also be expressed as shown in equation 2.4.

$$C = \frac{E}{1 - E} = \frac{1}{\alpha} \left[\frac{I_2 - S_2 I_3}{\left(1 - \left(\frac{S_3}{S_1}\right) S_2\right) I_1} - S_1 \right] \quad (2.4)$$

It follows then that the efficiency of the energy transfer can be calculated by equation 2.5.

$$E = \frac{C}{1 + C} \quad (2.5)$$

The α value shown in equations 2.3 and 2.4 is a proportionality factor that corrects for the different detection efficiencies for the donor and acceptor emission. For a given experimental setup α is a constant and can be determined experimentally [54,85,88]. In this work, the α constant was not derived. Instead a value was chosen so that the resulting relative FRET efficiency would be between 25 – 30%, as determined in adherent cells via APB. Since α remains unchanged, its estimation was not necessary, while a comparison of the relative FRET efficiencies of the individual LEGO constructs was still possible.

2.6.9 The phalloidin stain

The phalloidin stain was used to visualize the filamentous network of the actin cytoskeleton [75]. Coverslips of 12mm diameter, coated with the FRETing Matrix,

were placed in a 12-well plate (Nunc, Wiesbaden, Germany). RMCD cells were then allowed to adhere onto the coverslips over-night. Phalloidin conjugated to FITC was used (Molecular Probes Invitrogen GmbH, Karlsruhe, Germany) to prevent spectral overlap with the Cy3 emission. The phalloidin stain is detailed in the table 2.7.

The Phalloidin Stain

1. Wash cells 1x with the imaging buffer outlined in table 2.8
 2. Incubate cells in 4% PFA for 10 minutes.
 3. Wash 1x with imaging buffer.
 4. Permeabilize cells for 5 minutes with 0.1% Triton X-100/PBS.
 5. Place coverslip on a FITC-phalloidin (50 – 200nM final concentration) drop (20 μ L).
 6. Incubate for 30 minutes.
 7. Place coverslip back into the 12-well plate and wash 3x with imaging buffer.
 8. Add mounting medium (Mowiol) on slide and mount the coverslip.
-

Table 2.7: Fixation and staining of RMCD cells with FITC-phalloidin.

2.7 Solutions

Solution	Component	Amount	Comment
Live cell imaging buffer (10x)	NaCl	80g	
	KCl	4g	
	KH ₂ PO ₄	0.6g	
	MgCl ₂ ·6H ₂ O	1g	
	MgSO ₄ ·7H ₂ O	1g	
	NaHCO ₃	3.5g	
	Na ₂ HPO ₄	0.48g	
	CaCl ₂ ·2H ₂ O	1.85g	Adjust pH to 7.4 prior to adding CaCl ₂
On day of imaging, the following components were added to the 1x preparation:			
	D-glucose	1 $\frac{g}{L}$	
	BSA	0.5 $\frac{mg}{mL}$	
	Hepes		Up to 20mM final concentration
Loading Buffer (3x)	EDTA, 0.5M	2mL	
	Sucrose	6g	
	Bromophenol Blue, 2%	0.2mL	
	Xylene Cyanole, 2%	0.2mL	
	Ficoll 400	0.2g	
PBS(10x)	NaCl	80g	
	KCl	2g	
	Na ₂ HPO ₄ ·12H ₂ O	36.3g	
	KH ₂ HPO ₄	2.4g	
	H ₂ O	800mL	
PFA (4%)	PFA	20g	
	H ₂ O	400mL	
	PBS(10x)	10mL	Add NaOH dropwise until solution becomes transparent. Mix well and cool on ice Adjust pH to 7.3 and bring up volume to 500mL with H ₂ O. Sterile filter the solution and store at -20°C.
TBE(10x)	Tris	108g	
	Boric acid	55g	
	H ₂ O	900mL	
	Na ₂ EDTA, 0.5M, pH 8.0	40mL	

Table 2.8: Recipes for solutions prepared for the respective experiments.

Chapter 3

Results

3.1 LEGO

The fidelity of the final eleven constructs was verified through enzymatic test digests (enzymes are indicated at the top of figure 2.2) and by sequencing in the 3' or 5' direction from within the α helix or RBD fragments using primers outlined in chapter 2 (page 28). The respective DNA vectors were then transfected into adherent mammalian cells with a lipofection reagent (refer to page 27) and visualized with a confocal laser scanning microscope (CSLM) (also see table 3.1).

3.1.1 Lambda scan showed ECFP and Venus specific emission peaks

λ spectral scans were conducted on adherent cells expressing a LEGO construct and the presence of ECFP emission and Venus sensitized emission was confirmed. An example of such a measurement is shown in figure 3.1. The donor (ECFP) was excited at $\lambda = 405nm$ and the emission was recorded in 20 overlapping, 10nm-wide emission windows so that ultimately a total emission range of 438 – 608nm was measured. As evidenced in figure 3.1, two emission peaks were detected. The first peak occurs at 478nm and the second one at 526nm, which closely match those of ECFP and Venus, respectively. For comparison, the published excitation and emission spectra [33] of ECFP and EYFP are shown in figure 3.2. Beyond the

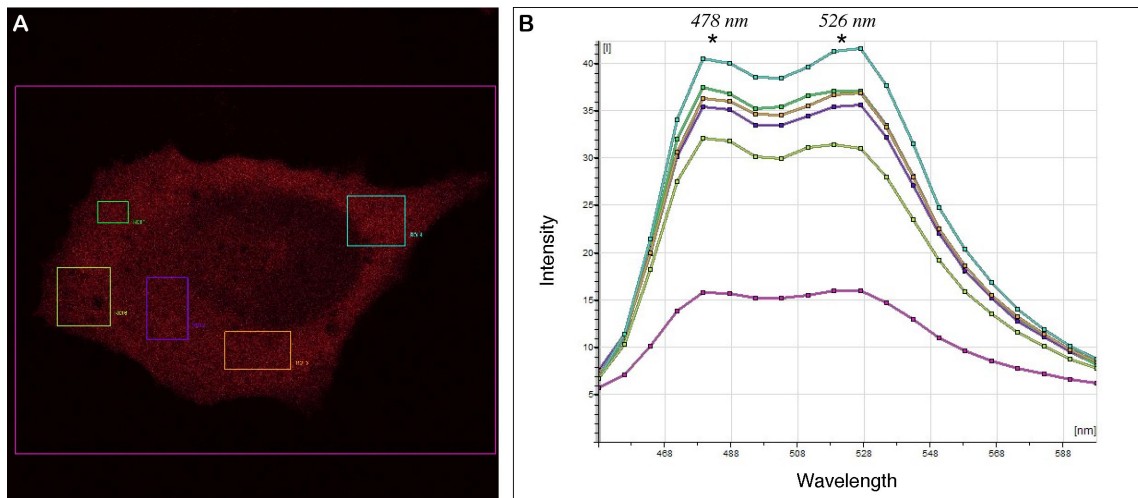


Figure 3.1: A λ -scan was performed on a HeLaSS6 cell expressing LEGO1 (**A**). The emission window of 438 – 608nm was subdivided into 20 overlapping, 10nm-wide windows. The respective emission was recorded sequentially upon $\lambda = 405\text{nm}$ excitation and displayed on an intensity versus wavelength plot (**B**) to reveal any possible emission maxima occurring within the 438 – 608nm emission window. The lines in **B** correspond to the region of interest of the same color shown in **A** from which the emission was analyzed.

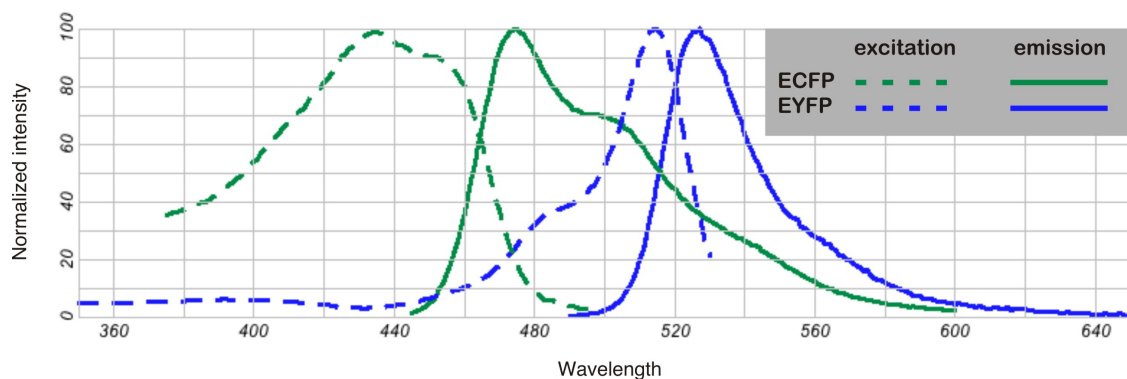


Figure 3.2: The excitation and emission spectra of ECFP and EYFP [33].

emission maxima of ECFP and EYFP, figure 3.2 further illustrates the spectral overlap that occurs between the ECFP and EYFP emission. This was of concern in later experiments (page 38) when the aim was to simultaneously collect donor emission and acceptor sensitized emission. The λ scans revealed the emission peaks and also the overall broadness of emission for the respective fluorochrome. Using this information, it was then possible to establish emission windows that ensured low spectral overlap, but allowed for enough light to be collected in order to obtain a good signal to noise ratio (see table 3.1).

CONFOCAL LASER SCANNING MICROSCOPE SETUP
ECFP excitation : 458nm (Kr-Ar laser)
ECFP emission window : 468 – 493nm
Venus emission window : 515 – 580nm
Objective : 63x oil immersion, NA 1.32

Table 3.1: Selected acquisition settings used to collect emission generated by LEGO constructs.

3.1.2 Acceptor photobleaching revealed presence of FRET

The presence of FRET and estimation of the FRET efficiency in adherent cells expressing a LEGO construct was also determined via acceptor photobleaching (APB). This method relies on the fact that the donor emission is quenched when resonance energy transfer (RET) is taking place. Therefore, photo-destruction or bleaching of only the acceptor in such a scenario will result in de-quenching of the donor fluorochrome. When donor emission is collected before and after photobleaching, while keeping the acquisition settings the same (see table 3.1), then the FRET efficiency can be calculated according to equation 3.1 shown in figure 3.3 [10, 98]. In equation 3.1, E refers to the FRET efficiency, while D_{pre} and D_{post} represent the donor emissions before and after acceptor photobleaching, respectively.

In sections A and B of figure 3.3 the donor emission and acceptor sensitized emission before APB are shown, respectively. After APB, the acceptor sensitized emission was

drastically reduced (figure 3.3D), while the donor emission increased slightly (figure 3.3C). In section E of the same figure is the image which results when the FRET efficiency is calculated according to equation 3.1. To better visualize the difference in FRET efficiency between the bleached and unbleached area, a surface plot is shown in section F of figure 3.3. Section F was generated with ImageJ and is based on the intensity values shown in section E. In other words, in addition to the x and y coordinates, every pixel received a third dimension, z, in which the intensity values are displayed. As before, the same colortable was used to enhance the contrast.

3.1.3 Ratiometric Imaging of Cells Expressing LEGO Constructs

The ratiometric method may be used to visualize FRET when the donor to acceptor ratio is constant [10, 102]. This is the case in all LEGO constructs, which are single-molecule FRET biosensors where the donor to acceptor ratio is always 1 : 1. The ratiometric approach relies on the fact that an increase in sensitized emission due to higher FRET efficiency is always coupled with a decrease in donor emission. Since the donor to acceptor ratio is fixed, it cannot be, for example, that an apparent increase in sensitized emission is due to higher accumulation of acceptor molecules only.

HeLaSS6 cells were grown in 24-well plates and transfected with the respective LEGO constructs. The cells were then fixed and imaged 18–24hrs after transfection, using the settings outlined in table 3.1. The Venus/CFP ratio was calculated for eleven different cells per LEGO construct measured and is summarized in figure 3.4. The eleven individual ratios were then used to generate one normalized, cumulative frequency versus ratio histogram for each LEGO construct. One such example is shown for LEGO5 in figure 3.5. Since the cumulative histogram showed a strong tendency toward a normal distribution, a Gaussian fit (equation 3.2 in figure 3.5) was attempted and a successful non-linear curve fit was reached. Based on this curve

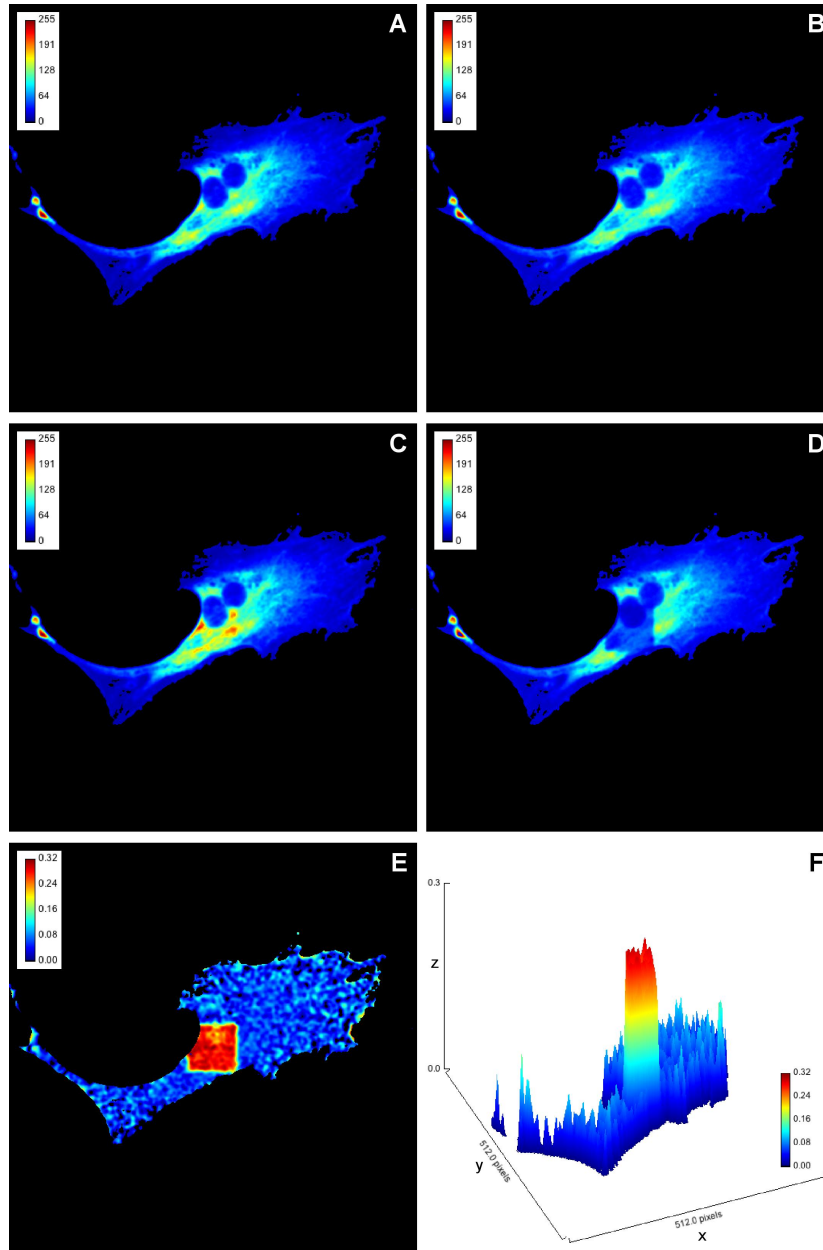


Figure 3.3: A RMCD cell expressing the LEGO1 construct. In **A** the ECFP (donor) emission is shown, while in **B** the sensitized emission of Venus (acceptor) upon donor excitation ($\lambda = 458nm$) is shown. ECFP emission and Venus sensitized emission after acceptor photo-bleaching (APB) with $\lambda = 514nm$ are shown in **C** and **D**, respectively. Shown in **E** is the resulting FRET efficiency calculated according to equation (3.1), where E is the FRET efficiency, D_{pre} the donor before APB and D_{post} the donor after APB. To further emphasize the difference in FRET efficiency between the bleached and the unbleached area of the cell a surface plot (**F**) was generated based on the intensity values in **E**.

$$E = \frac{D_{post} - D_{pre}}{D_{post}} \quad (3.1)$$

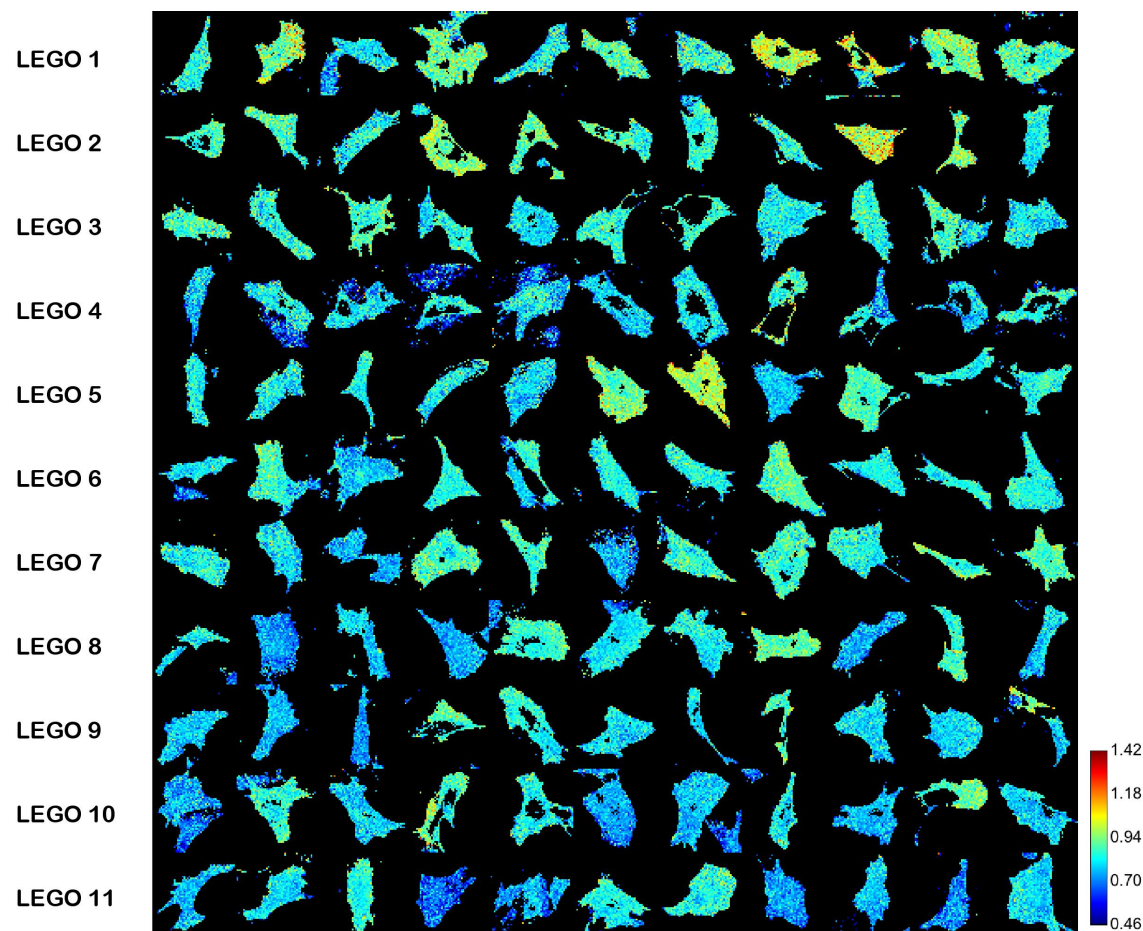
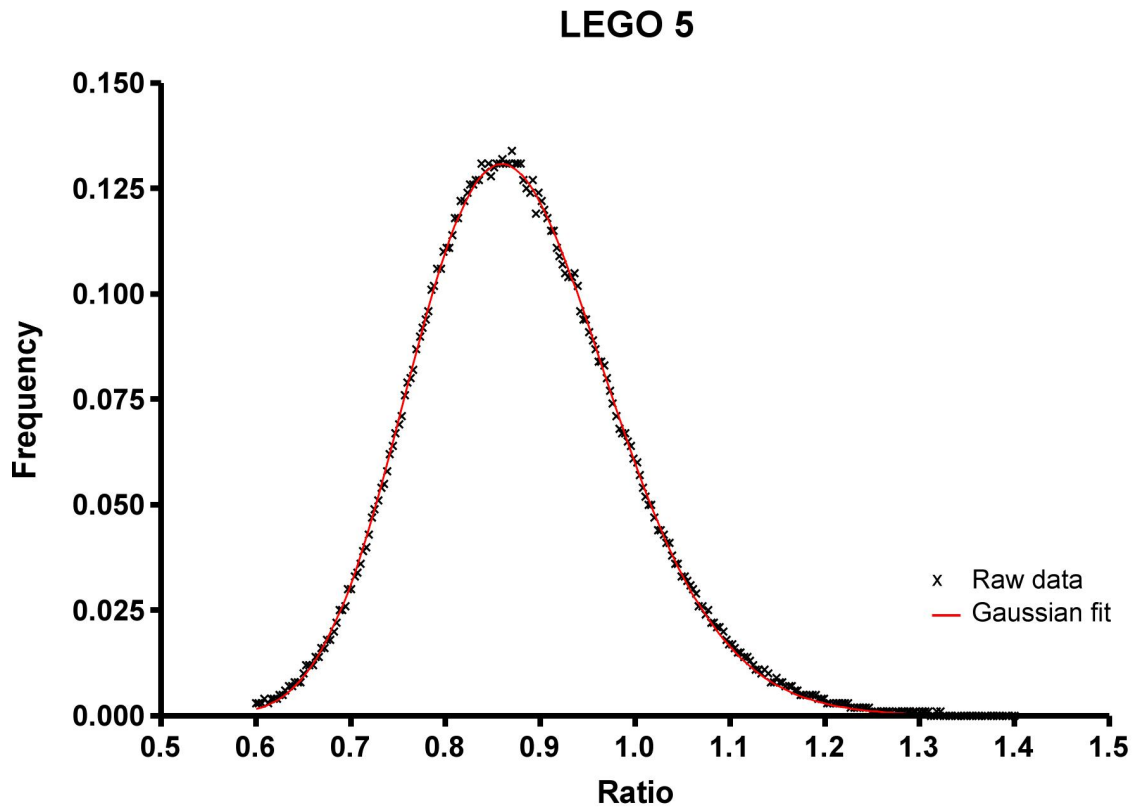


Figure 3.4: Donor and sensitized acceptor emission upon direct excitation of the donor ($\lambda_{ex} = 458nm$) were collected from 11 cells for each of the LEGO constructs (LEGO1-11). The acceptor sensitized emission was then divided by the donor emission to produce the overview shown here.



$$Y = \text{Amplitude} \cdot e^{-0.5 \left(\frac{\ln\left(\frac{\text{Ratio}}{\mu}\right)}{\sigma}\right)^2} \quad (3.2)$$

Figure 3.5: The data obtained from cells transfected with LEGO 5 (see figure 3.4) suggested a normal distribution, when visualized on a frequency vs. ratio scatter-plot. A non-linear (Gaussian) regression (equation 3.2) was applied to eventually successfully model the distribution of the experimental data. For this particular example $\mu = 0.859$ and $\sigma = 0.121$. These values were then used to generate figure (3.6), while taking into account the number of cells measured (n) to calculate the standard error.

fit and on the number of cells measured, the mean ratio and the corresponding standard error were calculated. The resulting values are visualized in figure 3.6. Overall, the FRET efficiency decreases with an increase in LEGO number. The

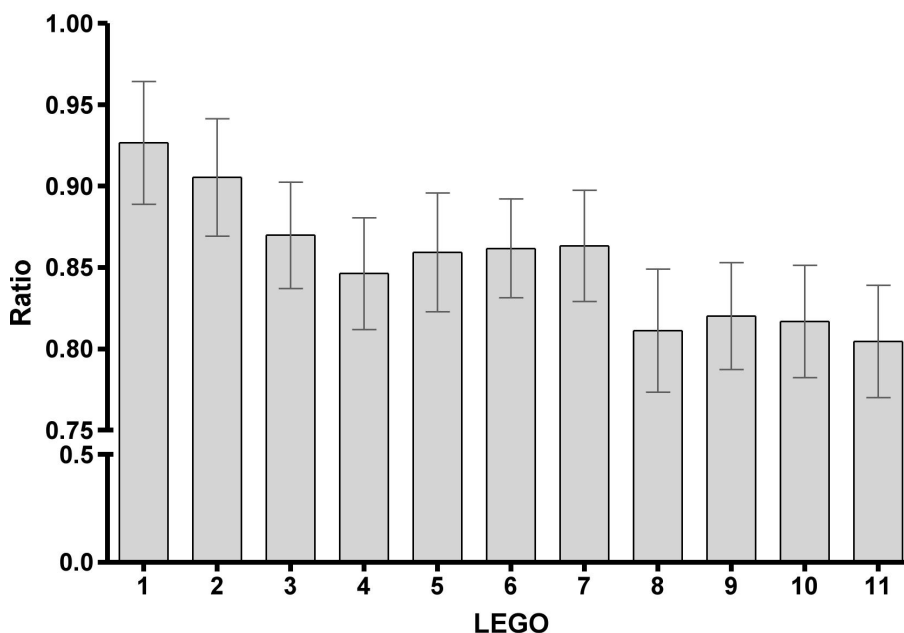


Figure 3.6: The mean ratio and standard error ($n = 11$ for each bar) determined from the non-linear regression illustrated in figure 3.5 for each LEGO construct are shown.

simplest approach to model this decrease is to conduct a linear regression (shown in figure 3.7 of the values in figure 3.6). The linear regression revealed a significant tendency for a decrease in FRET efficiency with an increase in LEGO number (i.e. an increase in the α helix positioned between the donor and acceptor fluorochrome). However, upon a closer look, there are several problems with the linear regression model. The variability of the mean ratios along the line of best fit should be the same and no clustering should occur. To test for this a graph was prepared to illustrate the vertical distances (residuals) above and below the line of best fit. Figure 3.8 showed a cluster at LEGO9-11, where differences were low, in comparison to LEGO1-4, 6-8. Furthermore, the residuals appeared not to be randomly scattered about the line of best fit, but seem to follow the pattern of a dampened sinusoidal line. To verify these concerns, a larger number of cells per LEGO construct needed to be measured, in order to obtain a more robust reading about the true mean value of the Venus/CFP

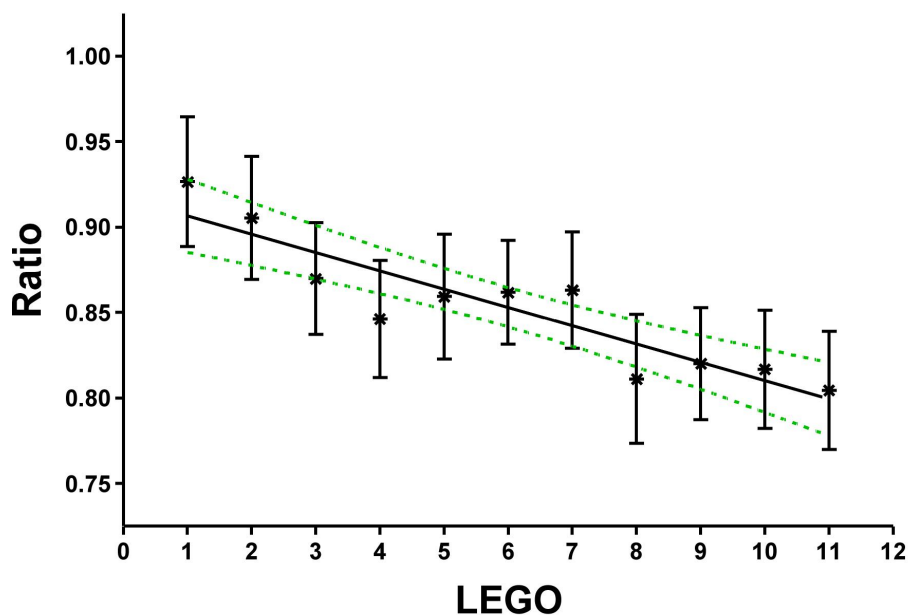


Figure 3.7: Linear regression of the mean ratios obtained from each LEGO construct. The same values as in figure 3.6 were plotted and a linear regression was conducted. The slope of the resulting line ($r^2 = 0.833$) is non-zero (P value < 0.0001) and negative. The dashed green lines demarcate the 95% confidence interval.

ratio.

3.1.4 Fluorescence Activated Cell Sorting (FACS) of LEGO-transfected cells

Flow cytometry information obtained from untransfected and transfected HeLaSS6 cells was organized with the *BD FACSDiva* software in three types of dot plots summarized in table 3.2 and shown in figure 3.9, where they are arranged by the type of transfection. Light scatter information obtained from untransfected cells

- | |
|-----------------------------|
| 1. SSC-A vs. FSC-A |
| 2. Venus Violet-A vs. CFP-A |
| 3. Venus blue-A vs. CFP-A |

Table 3.2: Types of plots used to visualize flow cytometry data with the *BD FACSDiva* software.

was used to generate a SSC-A vs. FSC-A dot plot in which the population of viable cells was selected and labeled as *P1* (figure 3.9A). The cells outlined by this gate

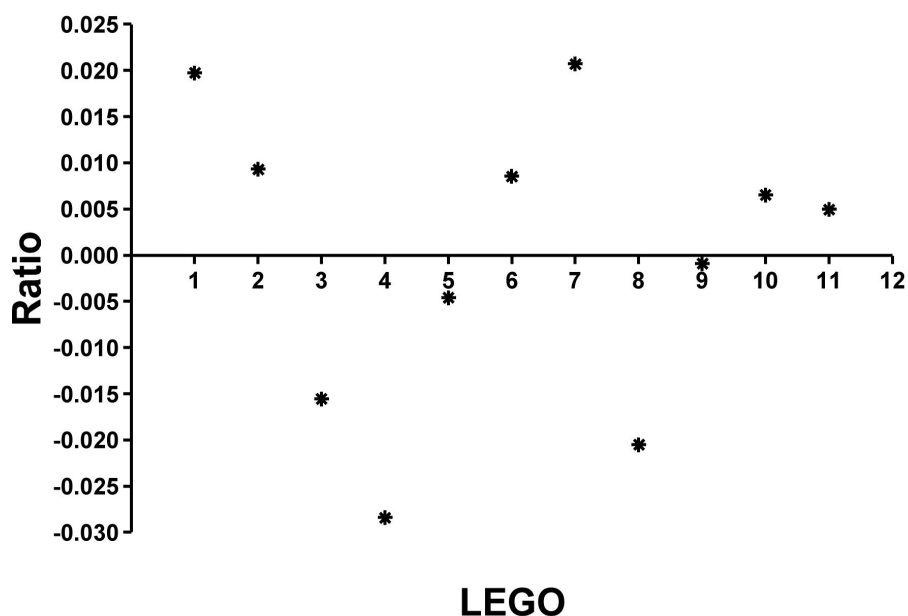


Figure 3.8: Residuals from the linear regression line shown in figure 3.7.

were used for all further measurements and are shown in D, G and J of figure 3.9. In the middle column of this figure are cells from the *P1* population described in terms of their acceptor sensitized emission ($\lambda_{ex} = 407nm$)¹ vs. donor emission ($\lambda_{ex} = 407nm$). Four quadrants (Q) were setup such that untransfected cells are found only in Q3 (B), indicating that negligible or no ECFP or Venus emission is present. ECFP only and Venus only transfected cells are shown in E and H of figure 3.9, respectively, where ECFP emission appears in Q4 and Venus emission appears in Q1. This distribution of the untransfected cells and cells transfected with the fluorescent controls indicated that a successful compensation with the *BD FACSDiva* software for the ECFP and Venus spectral overlap (also refer to figures 3.1 and 3.2) was achieved. These compensation settings were then applied for the remaining measurements of the LEGO-expressing cells, which localized in Q2 of the Venus violet-A vs. CFP-A dot plot (and example is shown in figure 3.9K). In the right column of figure 3.9 are dot plots based on the acceptor ($\lambda_{ex} = 488nm$) vs. donor emission ($\lambda_{ex} = 407nm$). C indicates that untransfected cells show neither

¹ λ_{ex} is the wavelength at which the respective acceptor or donor molecule was excited. Refer to table 2.1 on page 19 for the precise filter setup.

Venus nor ECFP emission, whereas F and I show the ECFP and Venus emission of cells expressing either the ECFP or Venus control. Cells shown in L express LEGO2 and emission of Q2 (shown in K) is colored blue, purple and yellow.

3.1.5 Estimation of the relative FRET efficiency from flow cytometry data

The relative FRET efficiency exhibited by the respective LEGO constructs was calculated with the *ReFlex* software package, which employs the algorithm outlined in [85]. The emission of directly excited Venus was plotted against that of directly excited ECFP (figure 3.10A). There, the region emphasized in blue shows the cells that were selected for the calculation of the relative FRET efficiency. Listed in table 3.3 is the number of cells used from each treatment to calculate the relative FRET efficiency.

LEGO	TRANSFECTION TYPE		
	LEGO only <i>n</i>	LEGO+RhoA _{T19N} <i>n</i>	LEGO+RhoA _{G14N} <i>n</i>
1	67690	30156	105855
2	111040	125453	112376
3	105357	117469	128436
4	109201	125361	133606
5	45373	51150	54108
6	49058	54243	58281
7	29640	40115	42553
8	22524	24411	26272
9	38880	54783	52775
10	43235	59036	59539
11	32855	37597	36439

Table 3.3: Number of cells measured per treatment.

Another way to visualize the cells used to determine the FRET efficiency is to plot the FRET efficiency vs. the emission of the directly excited donor (3.10B). From this perspective it can be seen that the error in the FRET efficiency estimation increases as the signal to noise ratio (SNR) of the ECFP emission decreases. Therefore, cells with low expression level of the respective construct were disregarded. Additionally,

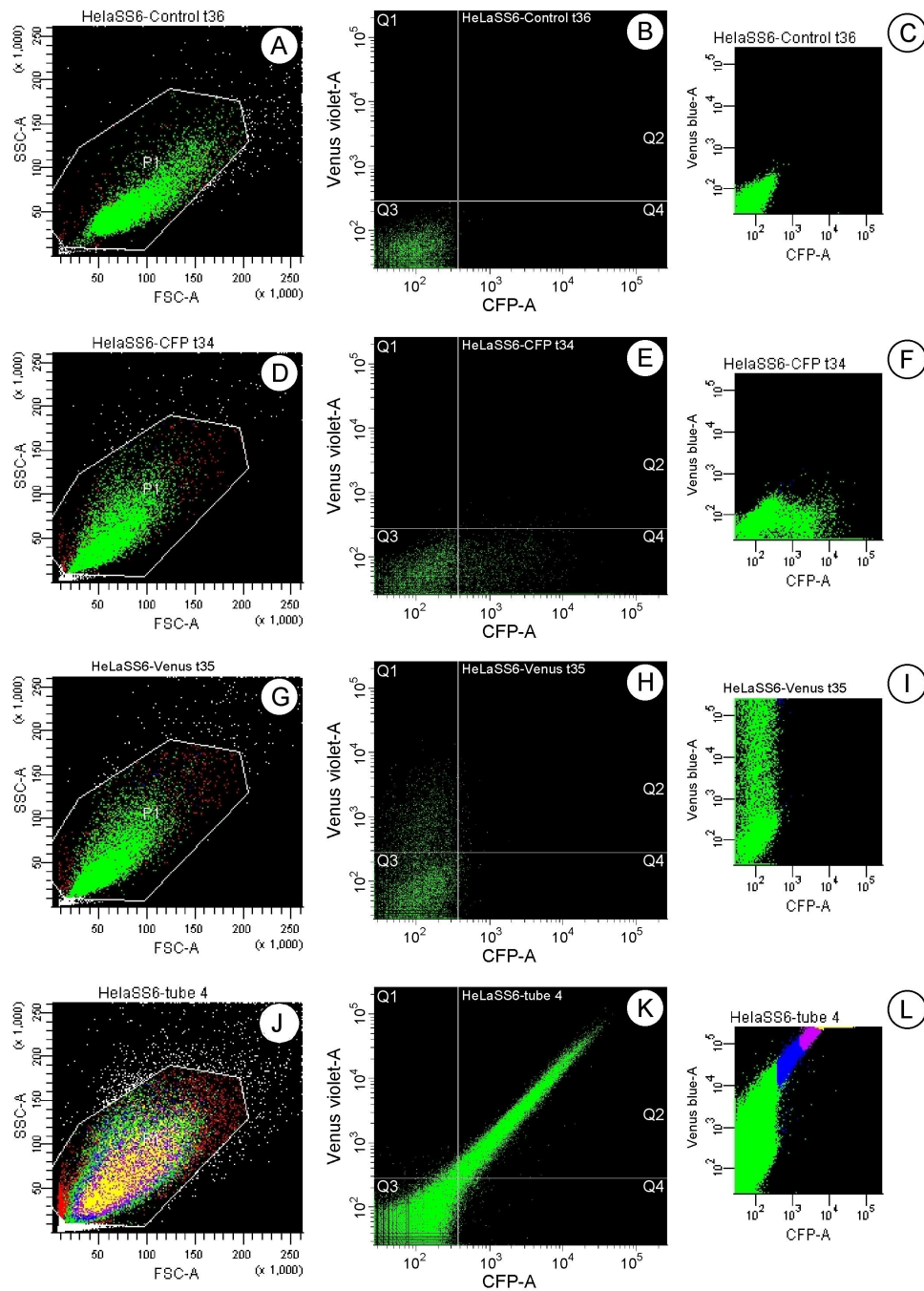


Figure 3.9: Untransfected HeLaSS6 cells (A-C), as well as cells expressing ECFP only (D-F), Venus only (G-I) or the respective LEGO construct (LEGO2 is shown in J-L), were measured with a fluorescence activated cell sorter (FACS). Dot-plots were generated to visualize the cell populations based on their size (*FSC-A*: forward light scatter), cell internal fine structure and granularity (*SSC-A*: 90° side light scatter), ECFP emission upon $\lambda = 407nm$ excitation (*CFP-A*: emission filter 410 – 490nm without a long-pass filter), Venus sensitized emission upon $\lambda = 407nm$ excitation (*Venus Violet-A*: emission filter 545 – 625nm with long-pass filter at 526nm) and Venus emission upon $\lambda = 488nm$ excitation (*Venus blue-A*: emission filter 500 – 560nm with a 502nm long-pass filter).

cells expressing the constructs at an excessively high level were also disregarded due to artifacts arising from the high expression levels of the FRET biosensor or the respective RhoA mutants. Figure 3.10C illustrates the final cell population used for estimation of the relative FRET efficiency.

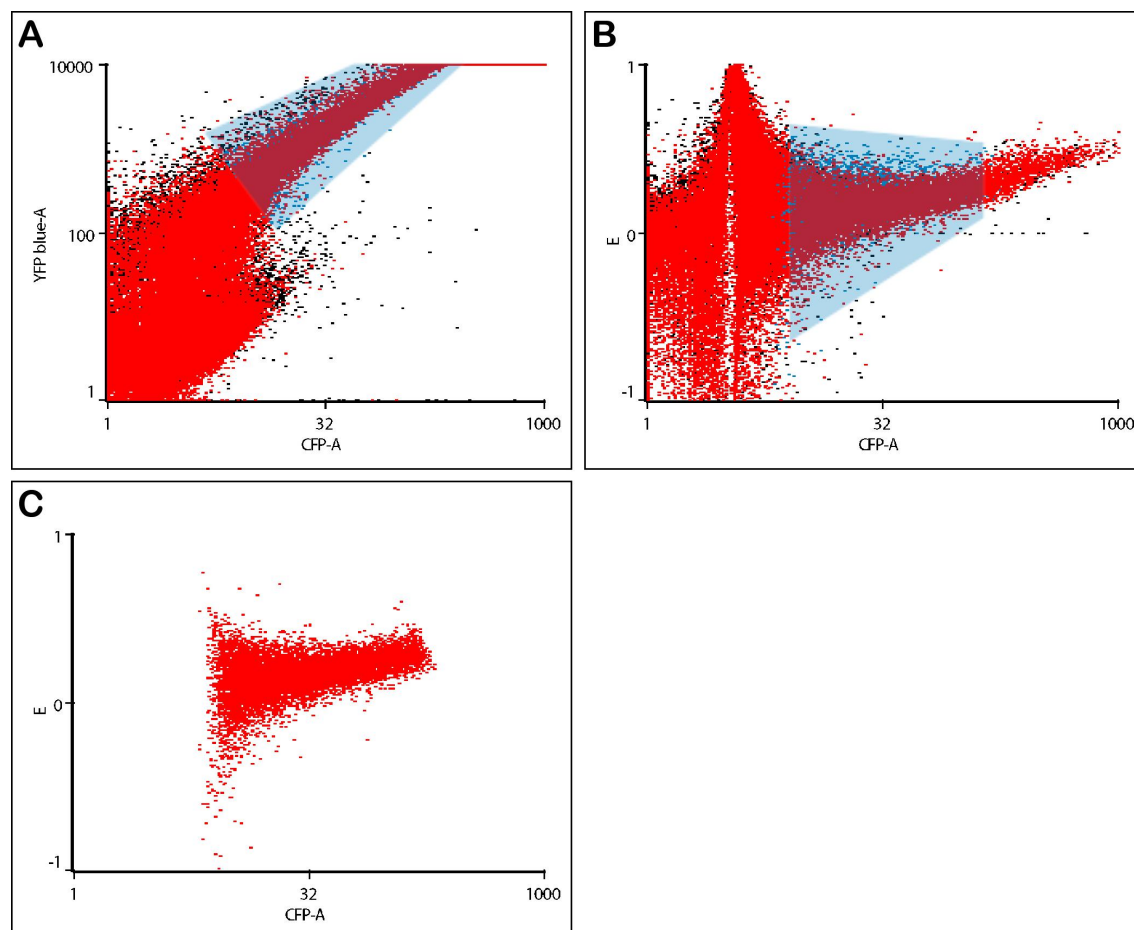


Figure 3.10: Properties of cells chosen for calculation of relative FRET efficiency.

According to the experimental design, an increase in LEGO number correlates with an increase in the distance between the donor and the acceptor and is accompanied by a simultaneous change in of the dipole orientation. In figure 3.11 the relative FRET efficiency was plotted against the respective LEGO. It is apparent that with an increase in LEGO number an overall decrease in FRET efficiency takes place. However, the decrease in FRET efficiency does not follow the pattern as shown in figure 1.6A. Instead, the decrease is biphasic. Two FRET efficiency increases between LEGO1 and 2 and between LEGO5 and 8 are followed by a subsequent decrease in

FRET efficiency. This indicates that the decrease in FRET efficiency shown in figure 3.11 is not dependent on the increase in distance between the donor and acceptor fluorochrome alone.

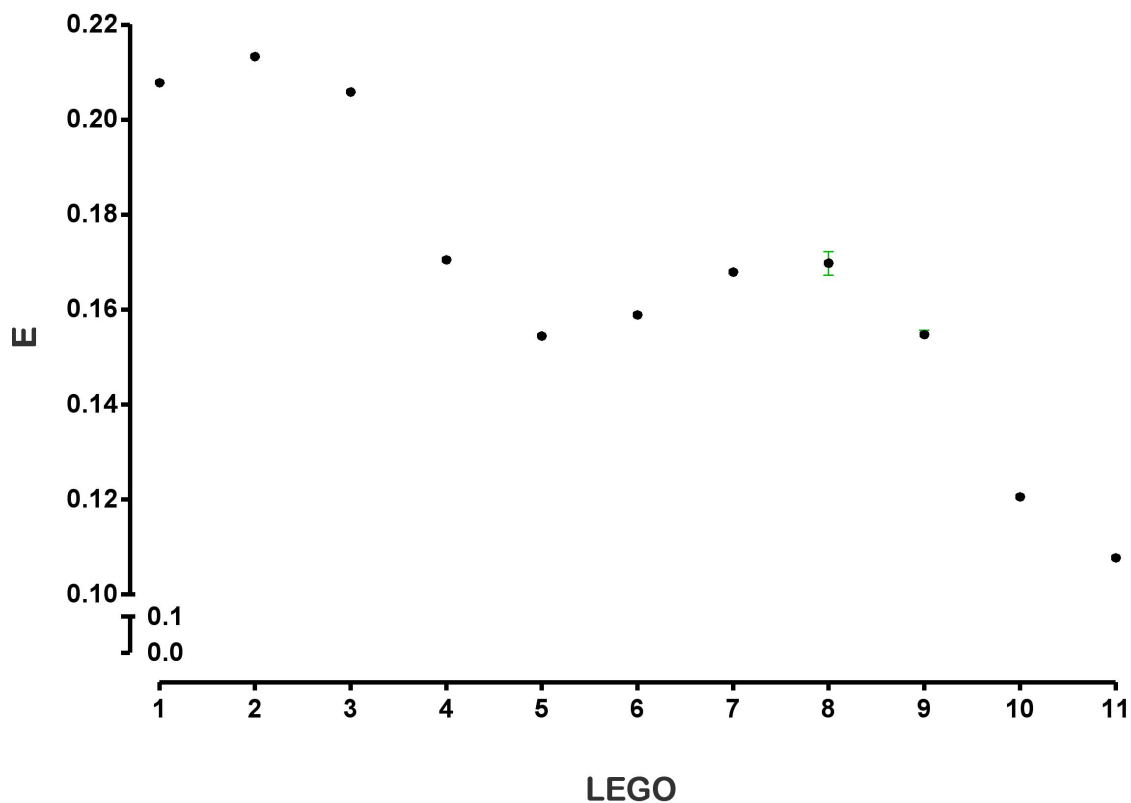


Figure 3.11: Relative FRET efficiency of HeLaSS6 cells expressing LEGO1-11, respectively. The error bars represent the standard error of the mean. The number of cells measured is reported in table 3.3.

The goal of the LEGO project was to generate a FRET biosensor with the task to report on the intracellular activity state of the RhoA GTPase. Moreover, the dynamic detection range of this biosensor was to be optimized toward maximum sensitivity by rationally altering the distance and orientation between the donor and acceptor molecules. In other words, the ideal biosensor would exhibit the highest difference between the RhoA GTPase bound versus unbound state. The sensitivity of the eleven LEGO biosensors was tested in a further set of experiments, in which a FACS analysis was performed on cells co-transfected with the respective LEGO and dominant negative RhoA (RhoA_{T19N}) or LEGO with constitutively active RhoA (RhoA_{G14V}). In the first scenario the biosensor was unbound, whereas in the second

it was bound. Presumably these two states correlate with two different conformations of the FRET biosensor and thereby with two different FRET efficiencies. The result of this set of experiments is shown in figure 3.12, where the relative FRET efficiency is plotted against the respective LEGO. The two different treatments per LEGO construct are indicated by a black square, which represents a co-transfection with RhoA_{T19N} and a red triangle representing a co-transfection with RhoA_{G14V}.

Overall, the FRET efficiency in figure 3.12 decreases in a bi-phasic manner resembling the pattern and relative magnitude seen in figure 3.11. The difference in FRET efficiency between the bound and the unbound scenario for each individual LEGO construct can be appreciated in figure 3.12. While the difference between the two states is high in LEGO1, 5, 8-10, it is entirely absent for LEGO2 and 4.

Interestingly, LEGO10 is better than LEGO2 at reporting differences in FRET efficiency between the bound and unbound state, even though its FRET efficiency is two-fold less than that of LEGO2. Furthermore, the change in FRET efficiency between the two states in LEGO10 in light of its maximum FRET efficiency is highest when compared to all other constructs.

Figure 3.13 illustrates the difference in FRET efficiency between the RhoA unbound (A, B) and bound (C, D) state of LEGO10. A shift toward the blue part of the colortable is apparent in A and C and is further emphasized in the form of the respective histograms.

3.2 FRETing Matrix

While the establishment of a FRET-based biosensor for the detection of the biochemical signaling leading up to generation of intracellular force was the aim of the LEGO project, the task of the FRETing Matrix was to report on the extension of this intracellular force in the form of extracellular force that cells exert on the substrate on which they adhere. According to the experimental model (figure 2.5), due

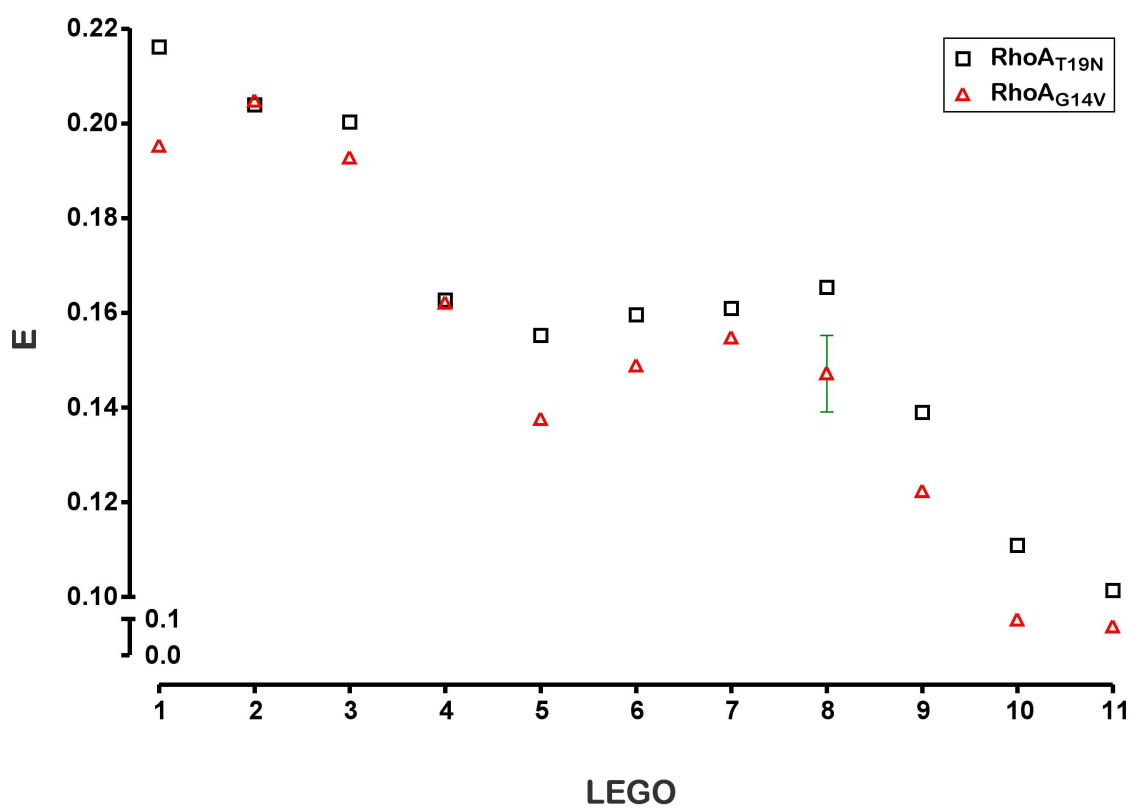


Figure 3.12: Relative FRET efficiency (E) of cells co-transfected with either LEGO and RhoA_{T19N} (black squares) or LEGO and RhoA_{G14V} (red triangles).

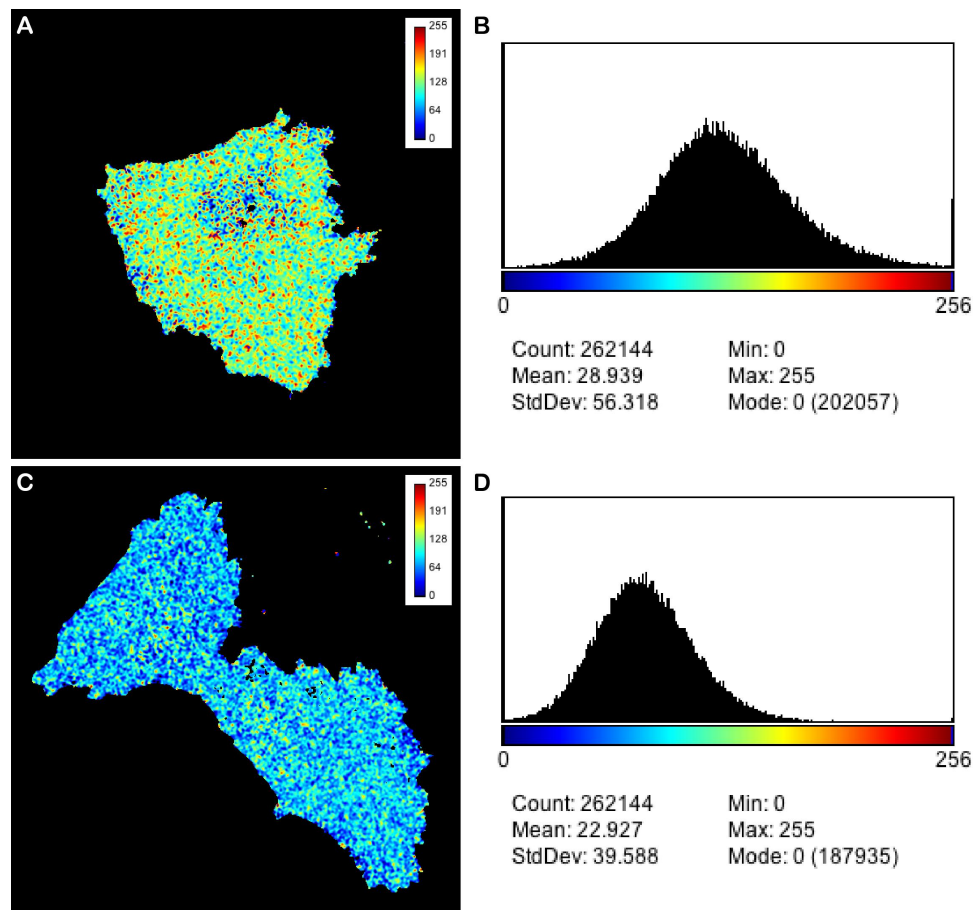


Figure 3.13: HeLaSS6 cell co-transfected with LEGO10 and RhoA_{T19N} is shown in **A** with the respective histogram in **B**. In **C** and **D** is a HeLaSS6 cell co-transfected with LEGO10 and RhoA_{G14V} and the resulting histogram, respectively.

to the absence of a criterion or selective pressure affecting the distribution of the differently labeled Fn within the Fn-coat, the FRET efficiency was predicted to be the same throughout the coat. However, once cells are allowed to attach to the FRETing Matrix, they would reorganize it and thereby cause local changes in the FRET efficiency, the extent of which would be correlated to the force exerted by the cells. The following results characterize the FRETing Matrix as an extra-cellular force detector and ultimately relate it to the intracellular biochemical signaling visualized by the LEGO sensors.

3.2.1 Lambda scan shows Cy3 and Cy5 emission peaks

A Fn coat was prepared as illustrated in figure 2.5. The spectral properties of the resulting FRETing Matrix were first characterized with a λ -scan on a CLSM. Images generated during the one such scan are shown in figure 3.14A, which summarizes the consecutive emissions collected in 10nm-wide emission windows between 558 and 703nm upon a $\lambda = 543nm$ excitation. The intensity in that figure peaks twice with an increase in the emission wave length observed through the respective emission window. To better localize the emission peaks, the average intensity of each window was estimated and plotted versus the respective wavelength (figure 3.14B). Emission maxima were revealed at $\lambda_1 = 556nm$ and $\lambda_2 = 670nm$. This finding is in agreement with published Cy3 and Cy5 spectral data shown in figure 3.15 and is indicative of the presence of these dyes and their proper function as such.

3.2.2 Acceptor photobleaching reveals the high FRET efficiency of the FRETing Matrix

Acceptor photobleaching was conducted to determine the FRET efficiency of the FRETing Matrix. An exemplary result is shown in figure 3.16. Part A and B of this figure show the donor (Cy3) emission before and after acceptor photobleaching, respectively. Equation 3.3 was applied to calculate the FRET efficiency image, which

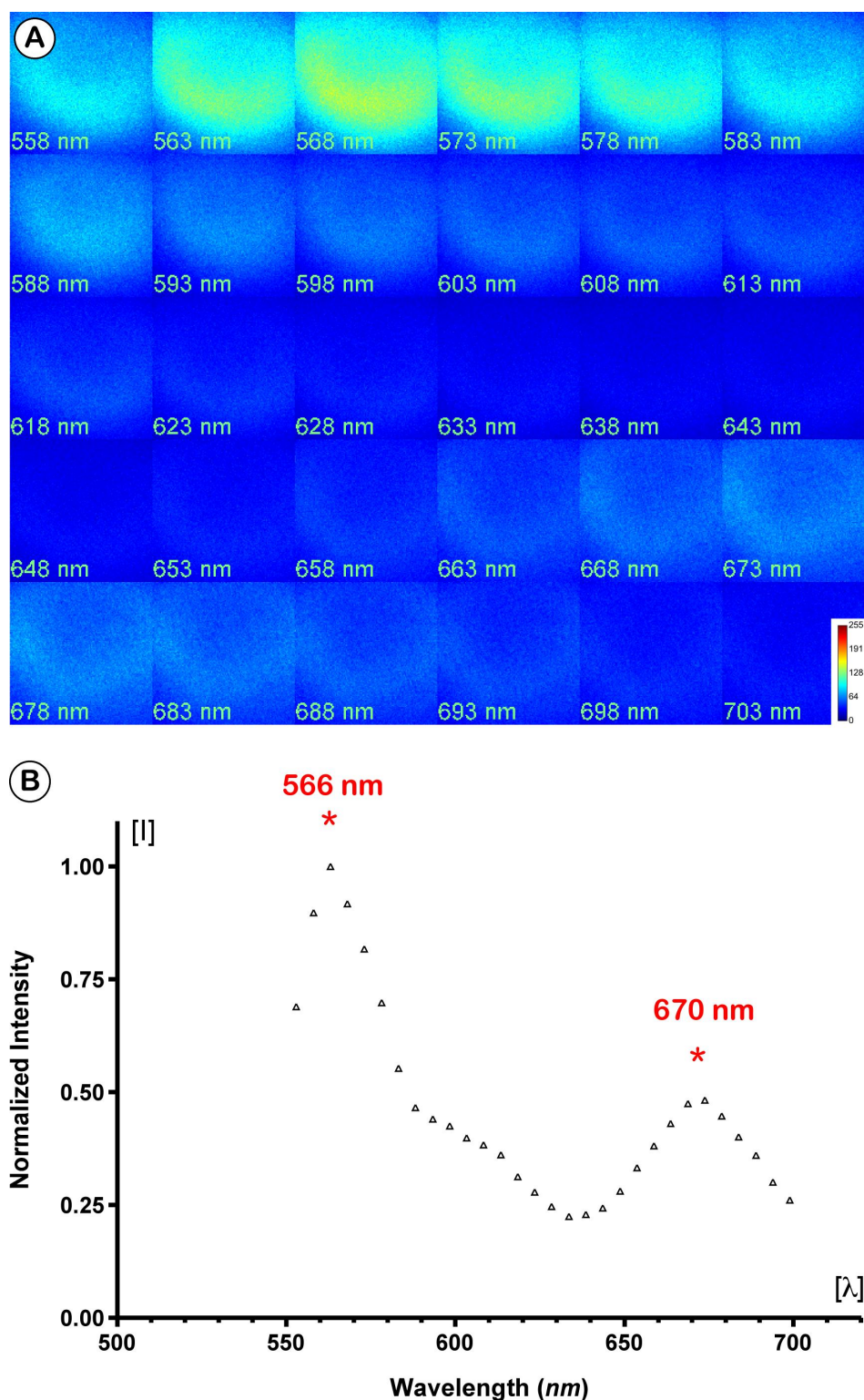


Figure 3.14: A λ -scan was conducted during which a FRETing Matrix preparation was excited at $\lambda = 543\text{nm}$. The emission was collected in 30 overlapping windows of 10 nm width covering 558 – 703nm. In **A** all 30 recordings are shown with the respective mean wavelength of the emission window at which they were recorded. The plot shown in **B** reveals the Cy3 (566nm) and Cy5 (670nm) emission peaks.

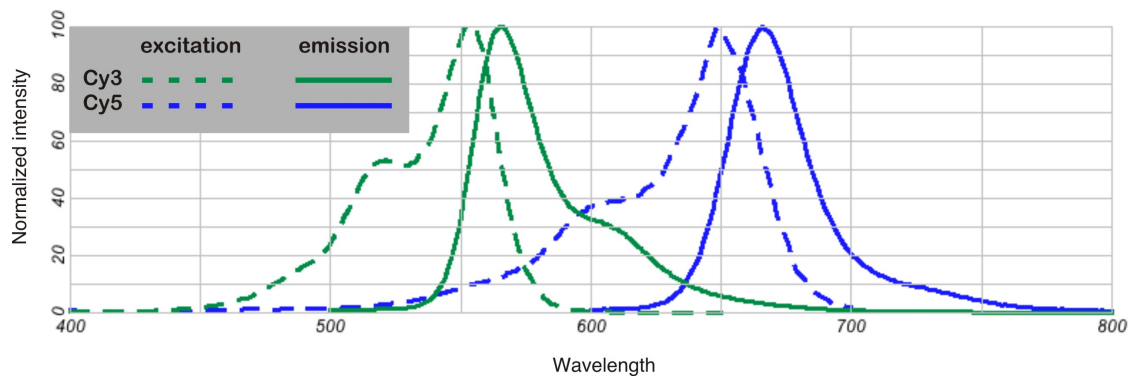


Figure 3.15: The excitation and emission spectra of Cy3 and Cy5 [33].

reported a average FRET efficiency of 54% in the section where the acceptor was bleached.

3.2.3 Ratiometric imaging of the FRETing Matrix

A more rapid and less invasive method for establishing differences in FRET efficiency is the ratiometric method. As outlined previously in the LEGO project (page 39), for this method the acceptor sensitized emission is divided by the donor emission. Since the increase in sensitized emission is coupled to a decrease or quenching of the donor emission, the ratio would then be indicative of the relative FRET efficiency in the field of view being investigated. To test this hypothesis a NIH/3T3 cell was allowed to adhere to the FRETing Matrix and the donor emission and acceptor sensitized emission was collected, both of which are shown in figure 3.17A and B, respectively. The ratio was then computed and is shown in section C of that figure. The interference reflection microscopy (IRM) image was also collected in a sequential scan and is shown in D. When the ventral membrane of a cell is observed in IRM-mode, adhesion sites will appear darker because they are in close proximity to the substrate. The darkest areas in D correspond to the most red regions shown in C. Overall, the highest relative FRET efficiencies are present at tensegrity points [31,32], which are characterized by more pronounced (darker) adhesions sites. The difference in FRET efficiency in areas to which the cell has no access and where

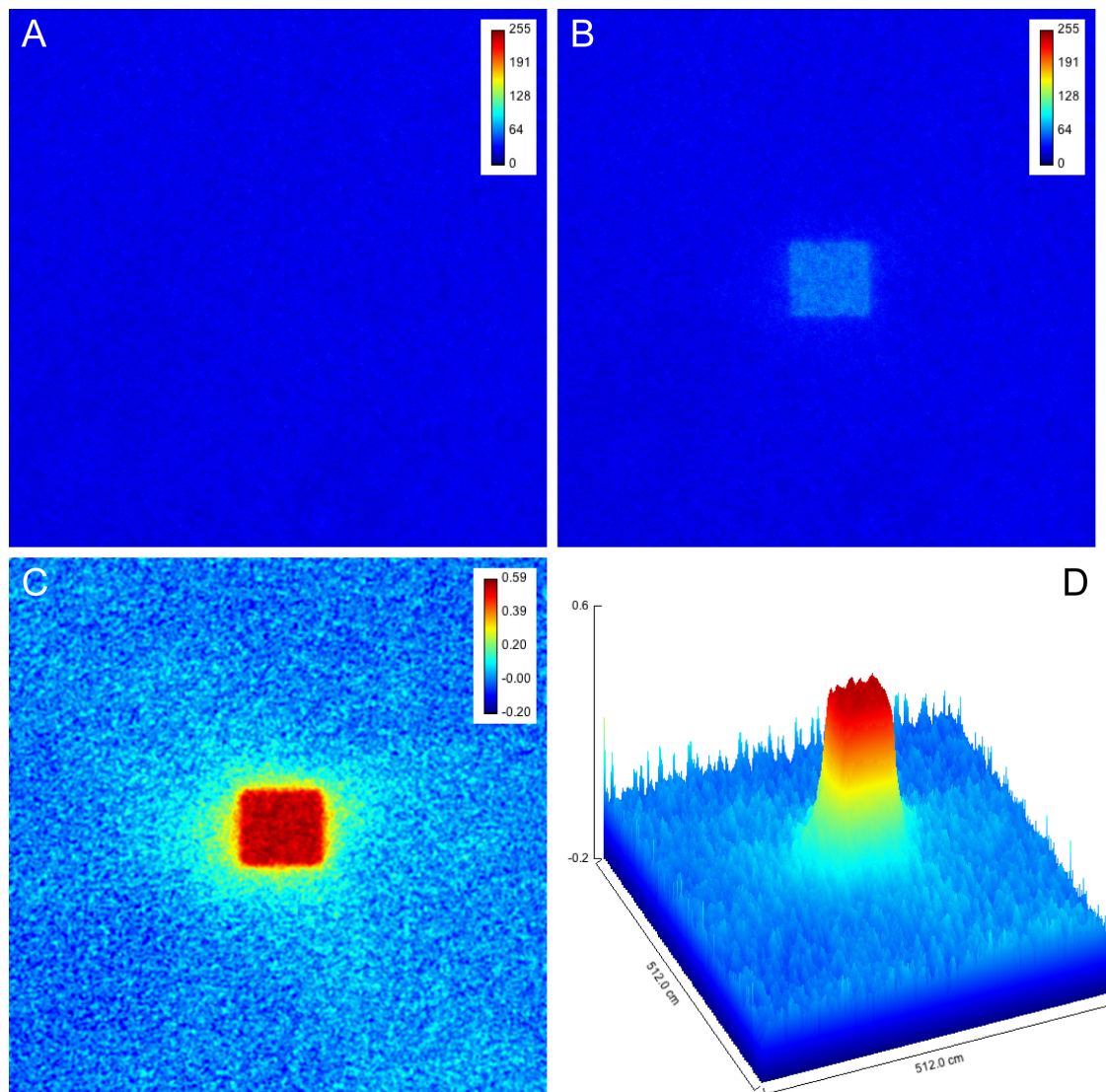


Figure 3.16: Cy3 emission before (A) and after (B) acceptor-photobleaching. In C and D are different representations of the FRET efficiency which was calculated to be 54% according to equation 3.3.

$$E = \frac{D_{post} - D_{pre}}{D_{post}} = 54\% \quad (3.3)$$

the FRETing Matrix is undisturbed is negligible as it is three-fold less than the maximum relative FRET efficiency displayed at adhesion sites.

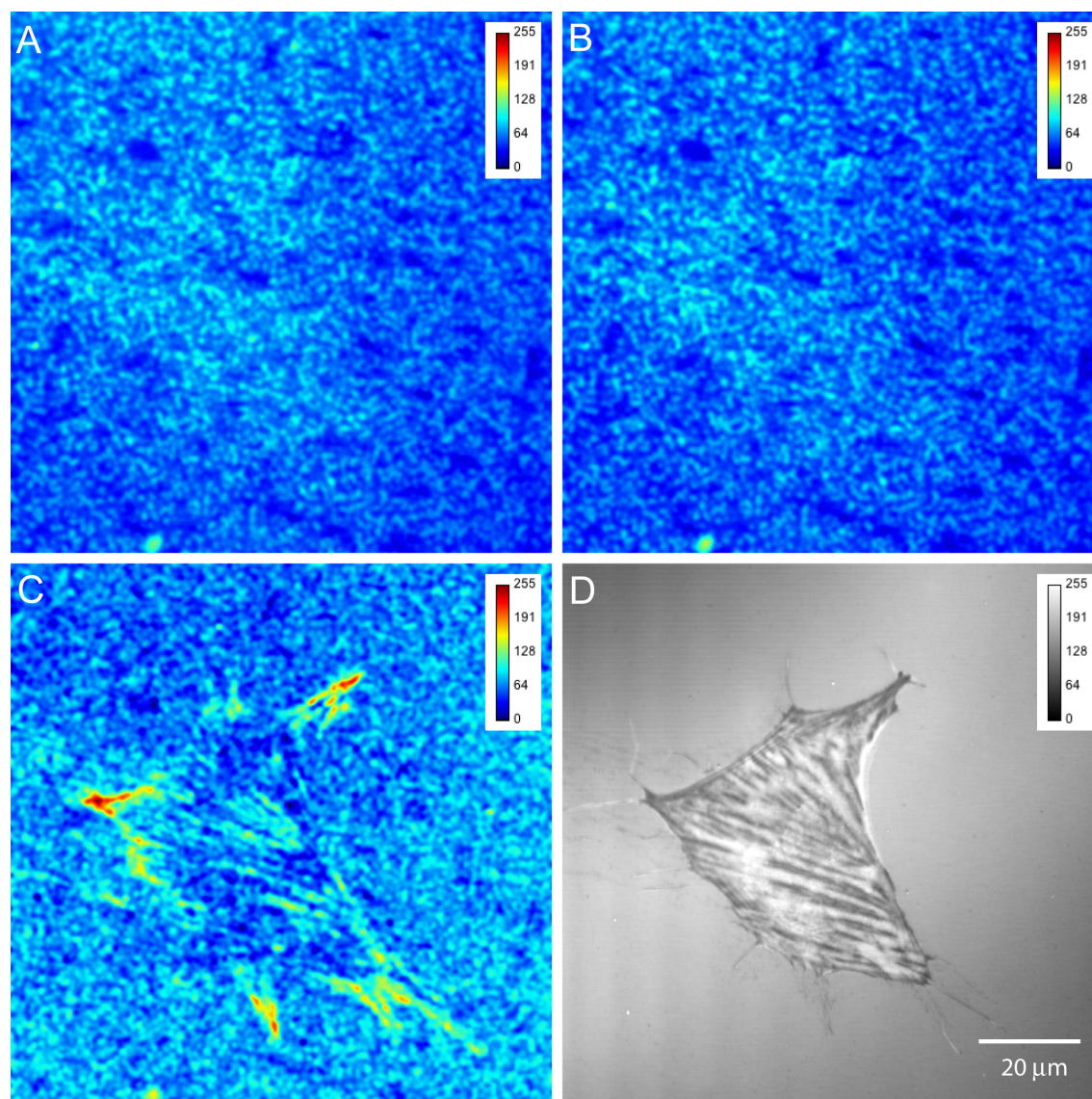


Figure 3.17: A NIH/3T3 cell grown overnight on the FRETing Matrix. Cy3 emission (A) and Cy5 sensitized emission (B) were collected upon Cy3 excitation ($\lambda = 543nm$). The Cy5/Cy3-ratio is shown in C. Interference reflection microscopy was used to visualize points of close contact (darker regions) between the cell and the substrate (D).

Further cells were imaged to test whether the ratiometric method faithfully reports on the variation in FRET efficiency. In addition to calculating the ratiometric image, the acceptor was photobleached so that a FRET efficiency image could be derived according to equation 3.1. An example is shown in figure 3.18, where the donor emission and acceptor sensitized emission before acceptor photobleaching are shown

in A and B and after in C and D. In E is the ratio image, whereas in F the APB image. Section H, which is a magnified version of the bleached area in F, was produced by adjusting the color table in F so that only the intensities in the second peak of the shown histogram are displayed. At this point H revealed similarities with G, which shows the ratio information of the same area. I was generated by applying an intensity-based co-localization algorithm. An overlay between I and the IRM image J is shown in K, which showed that both the Venus/ECFP and APB methods pointed to higher FRET efficiencies exhibited at cell adesion sites.

3.2.4 The high FRET efficiency patterns localize along stress fibers

The actin cytoskeleton plays a major role in the establishment of cell shape and therefore its biological function. Stress fibers are components of the actin cytoskeleton and are anchored in cell adhesion sites. In figure 3.19 an RMCD cell was imaged which had been allowed to grow on the FRETing Matrix and was subsequently stained with FITC phalloidin. Section A of this figure shows the Cy5/Cy3 ratio, while in B is the FITC phalloidin emission. C represents the overlay of A (red) and B (green). The highest relative FRET efficiency spots are located at ends of stress fibers. Incidentally, the size of a stress fiber is dependent on the force that is applied through it. The stress fibers ending in ratio spots where the FRET efficiency is highest have the highest FITC emission.

3.2.5 The onset of force exertion during cell spreading can be visualized with the FRETing Matrix

Following division, cells explore their environment, generate new adhesion sites and spread. The force exerted during initial stages of cell-substrate adhesion formation was monitored with the FRETing Matrix. Summaries thereof are provided in figures 3.20, 3.21, 3.22 and 3.23, which show different aspects of three exemplary B16F1 cells that stably express GFP:actin. The number in the upper-left corner of the individual

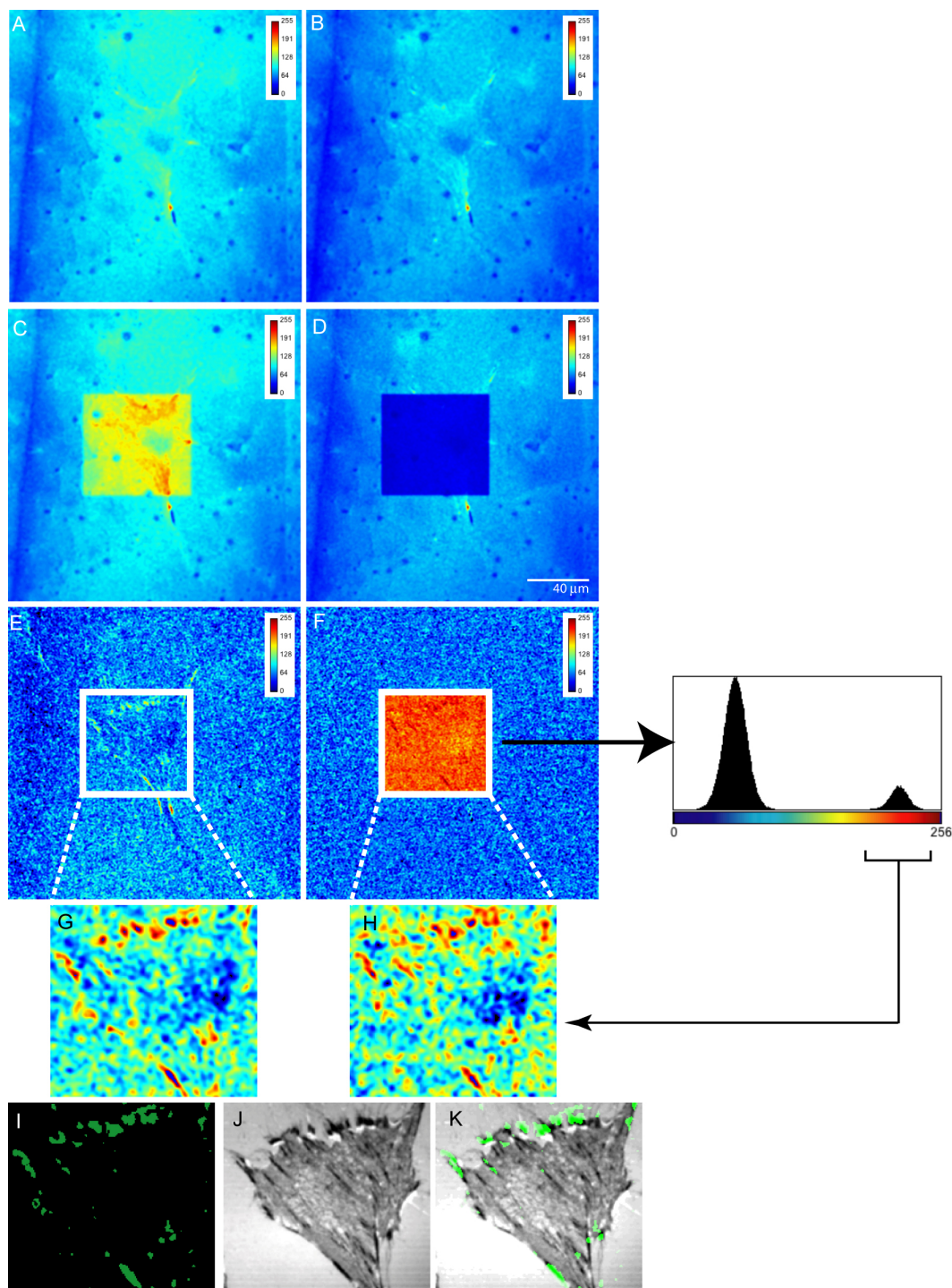


Figure 3.18: Cy3 emission (**A**) and Cy5 sensitized emission (**B**) of a FRETing Matrix on top of which a cell has adhered. The same area is shown after acceptor photo-bleaching, where **C** is the Cy3 emission and **D** is the Cy5 sensitized emission. The pre-bleaching Cy5/Cy3 ratio is shown in **E** and the FRET efficiency of the bleached area (white rectangle) is shown in **F**. **G** and **H** are magnified areas from **E** and **F**, respectively. However, the color table in **H** was adjusted to show only the second peak of the histogram showing the intensity distribution of **F** (shown to the right of **F**). **I** shows colocalization of features in **G** and **H**. The IRM image (**J**) is shown to visualize areas of substrate contact. **K** is an overlay between **I** and **J**.

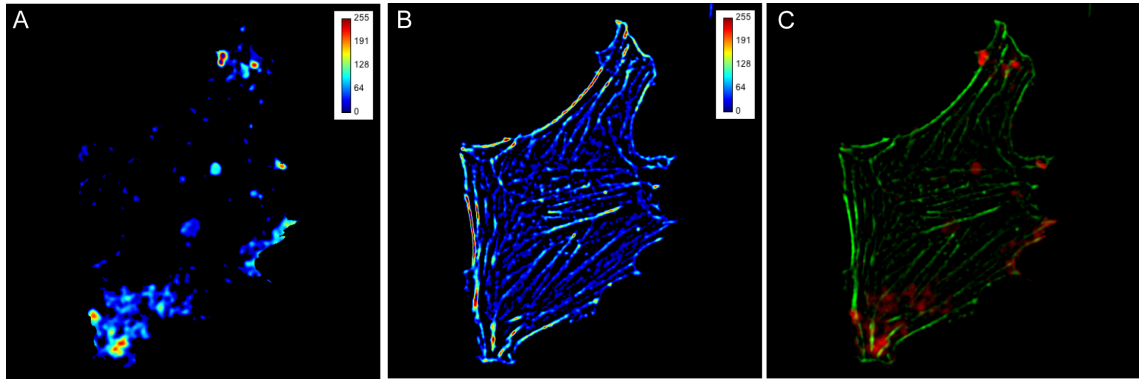


Figure 3.19: A RMCD cell was allowed to adhere to the FRETing Matrix and was subsequently stained with FITC-phalloidin. The high FRET efficiency pattern is shown in **A**. In **B** is shown the resulting FITC-phalloidin image after application of a low frequency band pass filter. The overlay is shown in **C**, where FITC-phalloidin is shown in green and the Cy5/Cy3 ratio in red.

images comprising figures 3.20 and 3.21 refers to the time (minutes) at which the images was recorded. Cell spreading was monitored with IRM and is shown in figure 3.20. Based on the degree of cell polarization and generation of dark adhesion spots, it is apparent that the lower two cells start spreading before the upper cell.

The delayed spreading of the upper cell can also be seen in figure 3.21, in which the overlay between GFP:actin (green) and the Cy5/Cy3 ratio (red) is shown. 120 minutes after the onset of imaging the central cell begins to modify the arrangement of the FRETing Matrix so that a high FRET efficiency spot begins to emerge in its upper left corner. In time the high FRET efficiency spots increase in number and intensify in the lower two cells. The upper cell begins to spread and polarize at 280 minutes at which time it starts to generate faint high FRET efficiency spots.

The same cells are shown once again, but at a higher magnification, in figure 3.22 to gain a better appreciation for the cell membrane protrusion (GFP:actin) and appearance and dynamics of the high FRET efficiency spots as the cells polarize during cell-spreading. In time, the membrane of the lower-left cell protrudes laterally (toward the left). At 208 minutes the high FRET efficiency spot is not at the left tip of this cells' membrane. However, by the 272nd minute, the high FRET efficiency spot has reached the left membrane tip. Then, at 288 minutes the left part of this cell

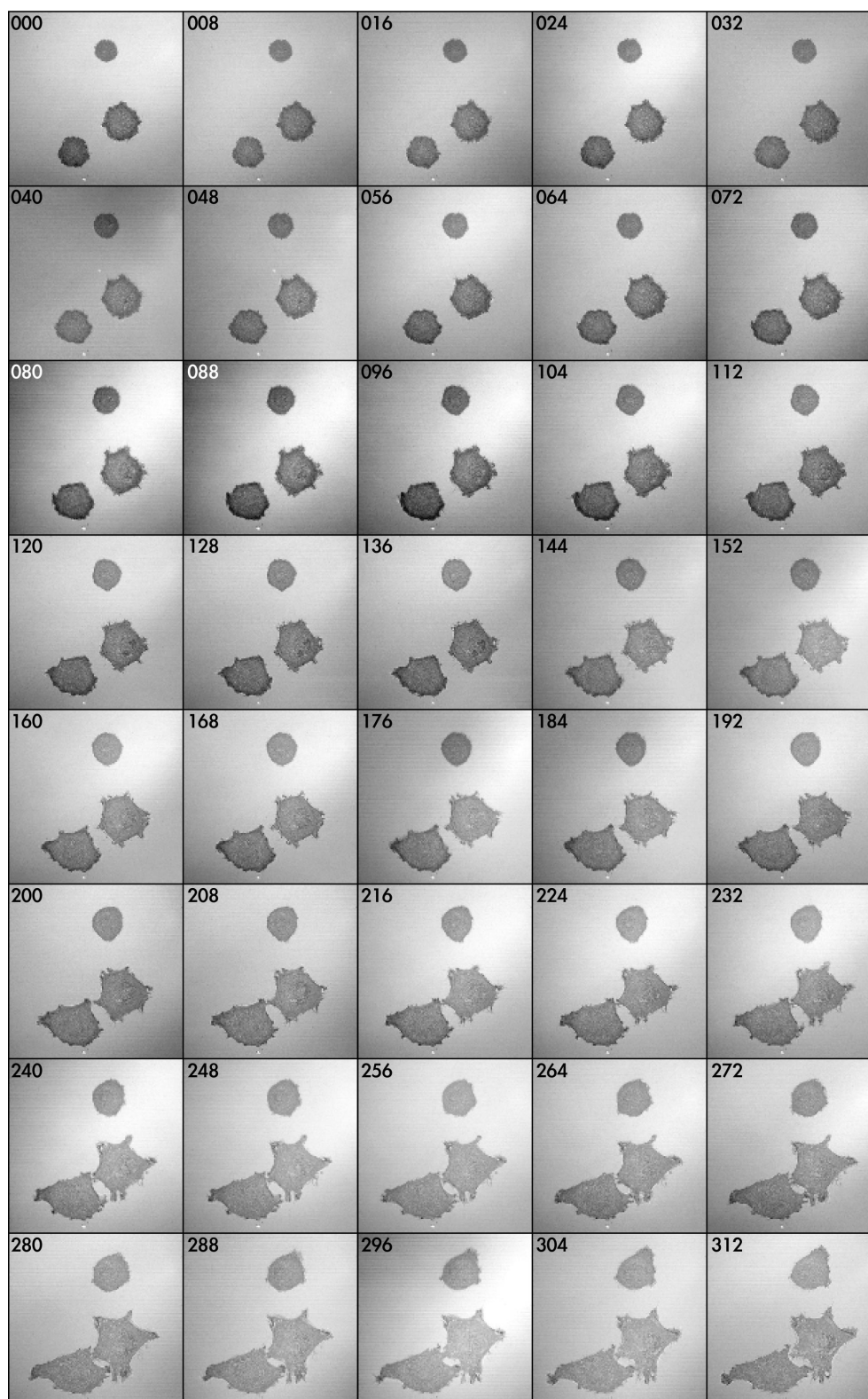


Figure 3.20: Three B16F1 cells expressing GFP:actin were allowed to adhere onto the FRETing Matrix in a “touch-down” experiment. Interference-reflection microscopy was used to monitor the progression of cell adhesion. The number in the upper-left corner indicates the time (minutes) at which the respective image was recorded.

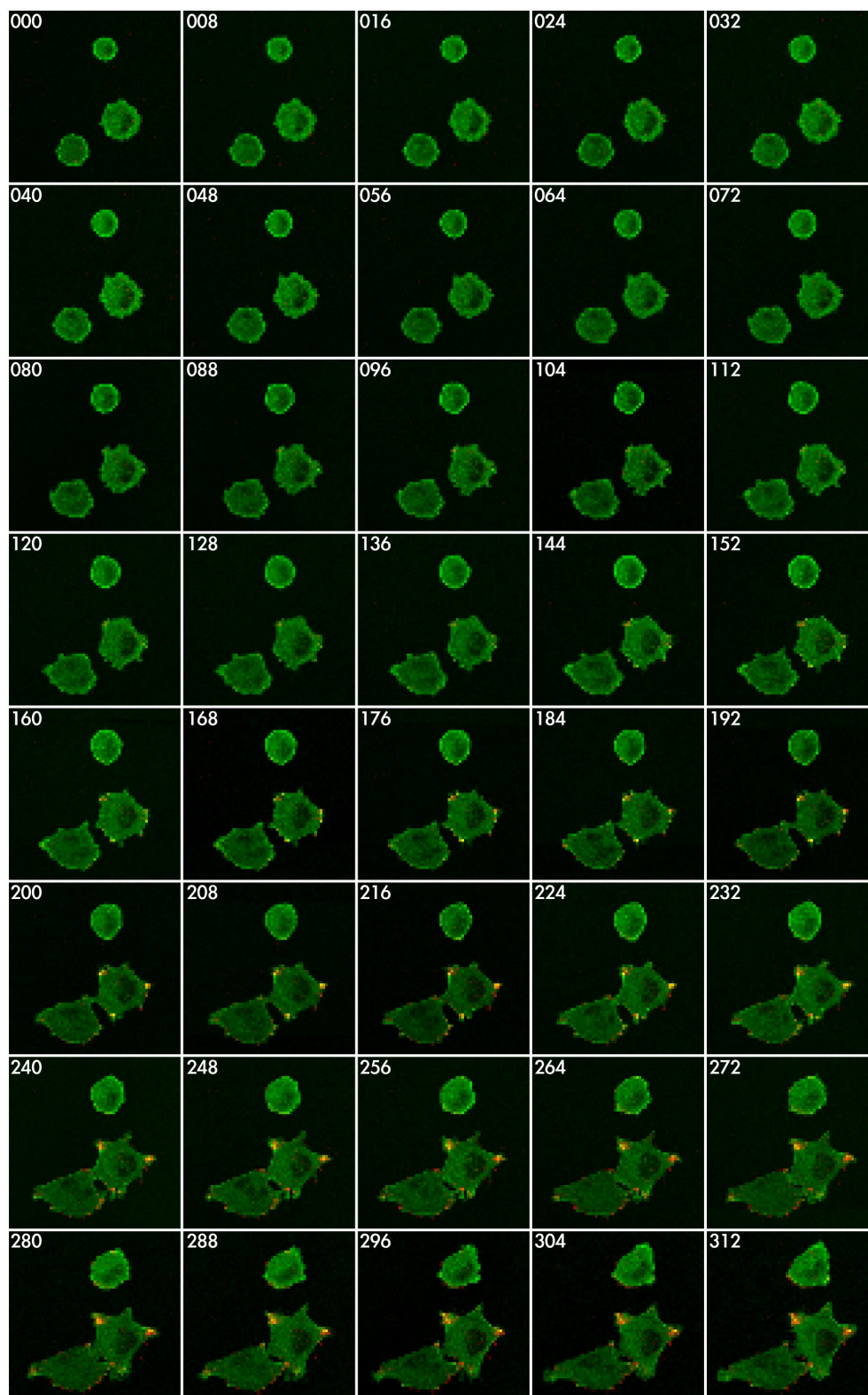


Figure 3.21: The same cells as in figure 3.20 are shown. However, in this figure the GFP:actin (green) and high FRET efficiency pattern (red) is shown.

begins to protrude more rapidly, leaving the high FRET efficiency spots behind once again. This dynamic interplay between cell protrusion and the localization of the high FRET efficiency spots is investigated more closely in figure 3.23. The Cy5/Cy3 ratio is shown in sections A, the upper row of C and in the upper row of section D. Furthermore, the GFP:actin emission is shown in B and the lower rows of C and D. In G is the overlay of the ratio (red) and GFP:actin (green) signal. Taken together, sections C and G visualize how during cell spreading the GFP:actin signal protrudes first and is then followed by subsequent increase in FRET efficiency (also illustrated in E). D emphasizes the fact that the FRETing Matrix can report transient changes in its FRET efficiency. As the GFP:actin signal increases and decreases, there is also an increase, followed by a decrease in FRET efficiency (the latter is also shown in F).

3.2.6 High FRET efficiency spots correlate with actin stress fibers during cell migration

A process that might ensue following cell spreading is cell migration. Force exertion during cell migration was investigated in B16F1 cells stably transfected with GFP:actin and is summarized in figures 3.24 and 3.25. The first of these two figures illustrates a whole cell view at the starting (0 minutes) and end point (10 minutes). Three different aspects of this cell were recorded over time as it migrated toward the lower-left direction: IRM (A, B), GFP:actin (C, D) and the Cy5/Cy3 ratio (E, F). Shown in G and H is the overlay between the GFP:actin emission (green) and Cy5/Cy3 ratio (red) at time points 0 and 10 minutes, respectively. Once more (compare with figure 3.19), high FRET efficiency spots localized along and most often at the ends of actin stress fibers. This finding also parallels earlier observations shown in figure 3.17.

Figure 3.25 illustrates the events taking place in figure 3.24 at a greater magnification. All sections of this figure are overlays between GFP:actin and the Cy5/Cy3

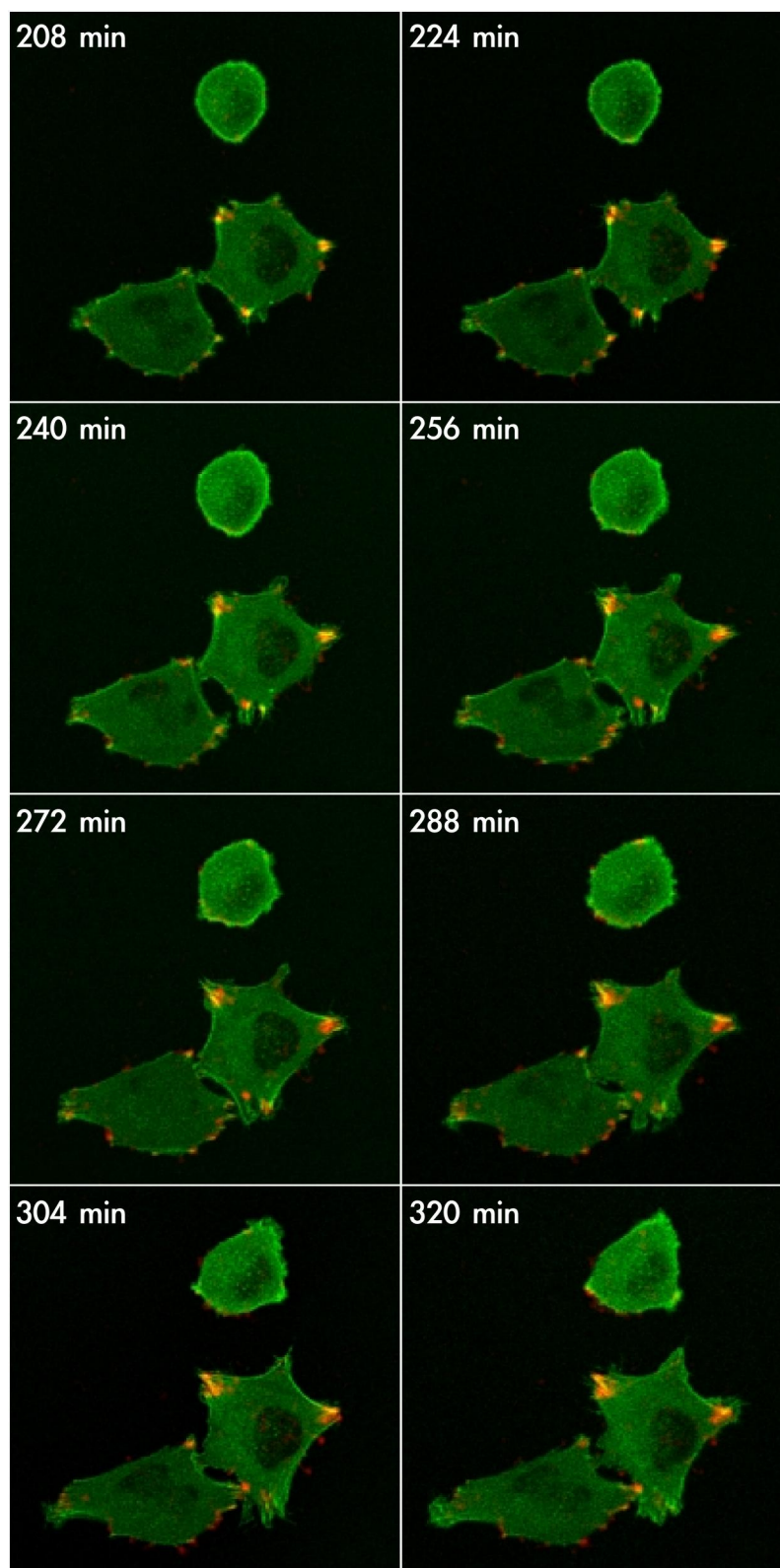


Figure 3.22: The same cells as in figures 3.20 and 3.21 are shown at a higher magnification to better demonstrate the actin cytoskeleton and high FRET efficiency pattern dynamics.

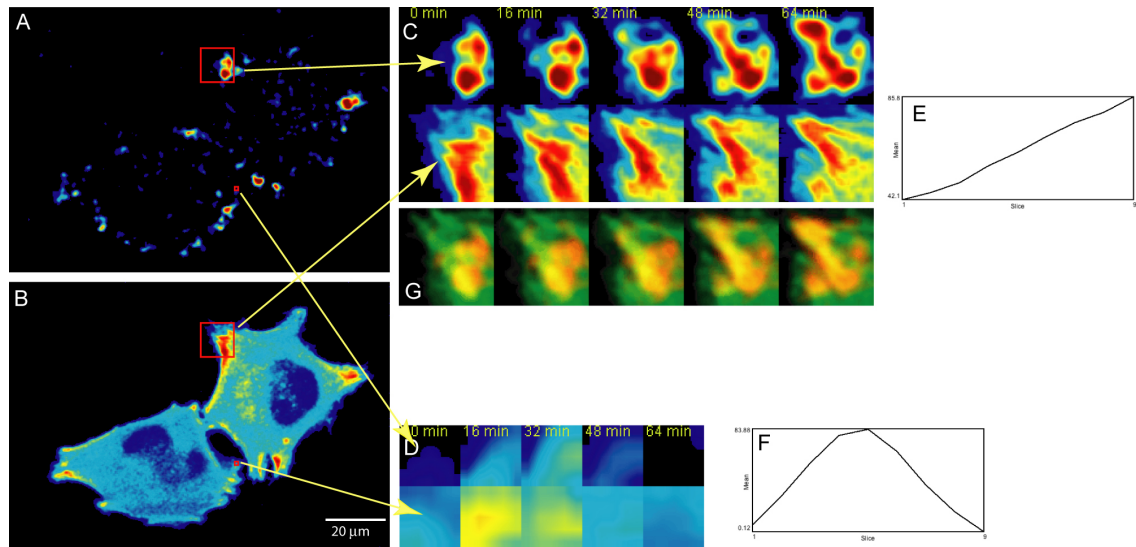


Figure 3.23: **A** and **B** show the Cy5/Cy3 ratio and GFP intensity (B16F1-GFP:Actin cell line) images, respectively, at 0 minutes. **C** and **D** are zoomed-in areas, where the top row represents the Cy5/Cy3 ratio and the bottom row the GFP intensity. **E** shows the increase in the ratio (i.e. FRET efficiency) over time, whereas **F** illustrates an example where a transient increase in FRET efficiency occurs. **G** represents the overlay between the GFP and Cy5/Cy3 ratio shown in **C** and shows that cell expansion due to actin polymerization occurs prior to exertion of force.

ratio. Shown in the upper-left corner is the cell at the onset of migration, while in the lower-right corner is the same cell at 10 minutes later. In-between are six images that were recorded in 2 minute intervals and which represent enlargements of the area indicated in red. This red rectangle is stationary in the two low-magnification images and also serves as an orientation marker to show that the cell migrates in the lower-left direction. In time, a collapse of the most outer (upper-right) actin stress fibers takes place. Simultaneously, new stress fibers are created or emphasized, some of which are labeled with 1, 2 and 3. For example, the stress fiber the associated high FRET efficiency spot indicated by the arrow next to the letter *b* in the 0 minutes frame completely disappears after 6 minutes. The letter *a* points out a stress fiber and the associated high FRET ratio further inward within the cell. This ratio spot persists longer than the one in *b*, but also disappears as the associated stress fiber collapses. The numbers 1, 2 and 3 indicate anchoring points that connect to form a triangular stress fiber formation. As the cell moves downward, the anchoring point at 1 exerts force on the FRETing Matrix such that a high FRET efficiency spot

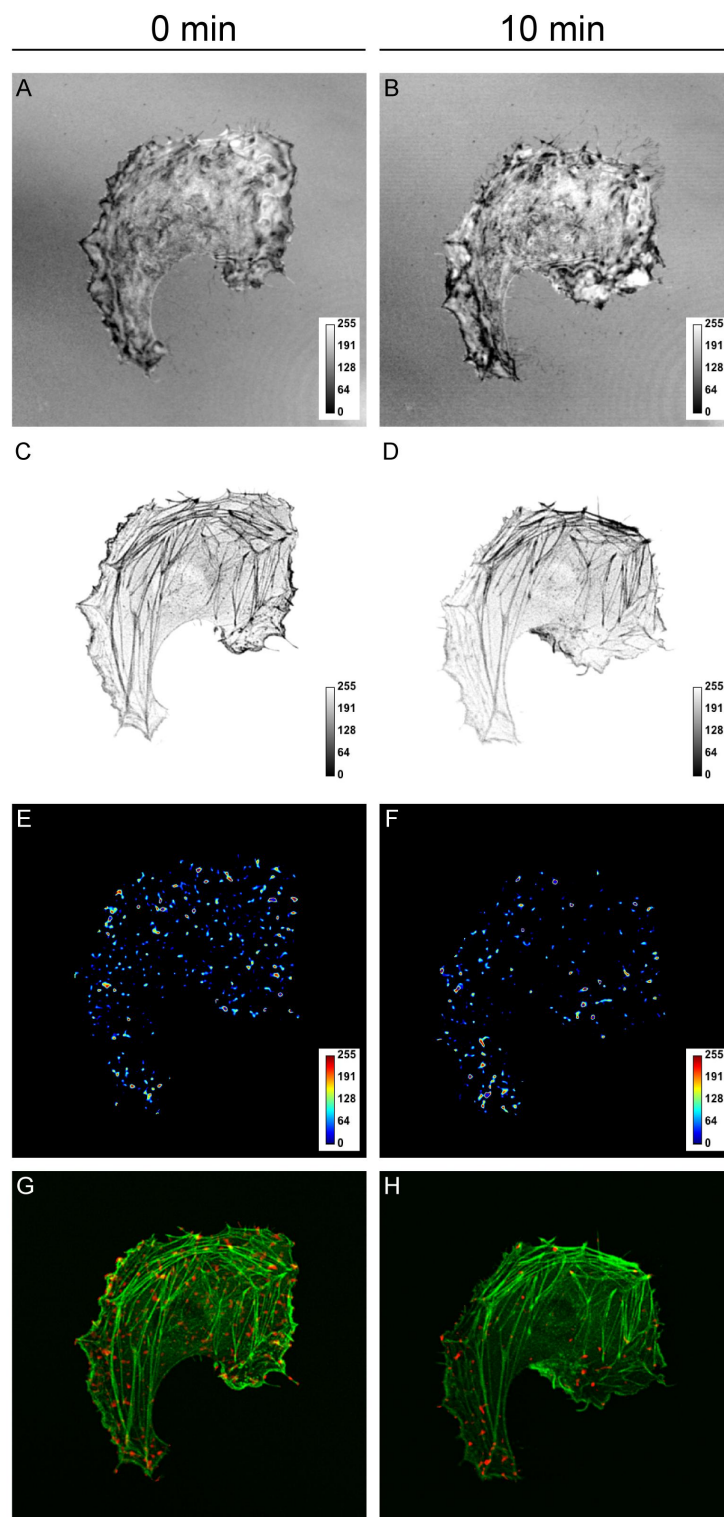


Figure 3.24: A B16F1 cell expressing GFP:Actin migrates on the FRETing Matrix. In **A** and **B** is the interference reflection microscopy view at 0 and 10 min, respectively. Similarly, **C** and **D** show the GFP:actin and **E** and **F** the Cy5/Cy3 ratio, respectively at the two different time points. **G** and **H** are overlays of the GFP:actin and Cy5/Cy3 ratio at 0 and 10 min, respectively.

appears.

3.2.7 RhoA GTPase is involved in the patterning of the high FRET ratio spots

The dynamics of the actin cytoskeleton underly the control of the RhoA GTPase. The involvement of RhoA GTPase in the formation and patterning of the high FRET ratio spots is laid out in figure 3.26. Two different cell types are shown: sections A-F are NIH/3T3 cells, while sections G-L are B16F1 cells. Both cell types were either co-transfected with GFP:actin and RhoA_{G14V} (shown in A-C and G-I), the constitutively active form of RhoA. The two cell types were additionally co-transfected with GFP:actin and RhoA_{T19N}, the dominant negative form of RhoA. In the first column of figure 3.26 the GFP:actin emission is shown after it had been inverted to achieve better contrast. In the middle column of this figure is the Cy5/Cy3 ratio, while in the right column is the overlay between GFP:actin (green) and the Cy5/Cy3 ratio (red). Overexpression of RhoA_{G14V} lead to massive stress-fiber formation, while overexpression of RhoA_{T19N} resulted in the complete lack thereof. When constitutively active RhoA GTPase was expressed, the high FRET ratio spots were of higher intensity and organized along stress fibers and especially their anchoring points. The opposite was true when the dominant negative RhoA was expressed: the high FRET ratio spots were less intense and more disorganized.

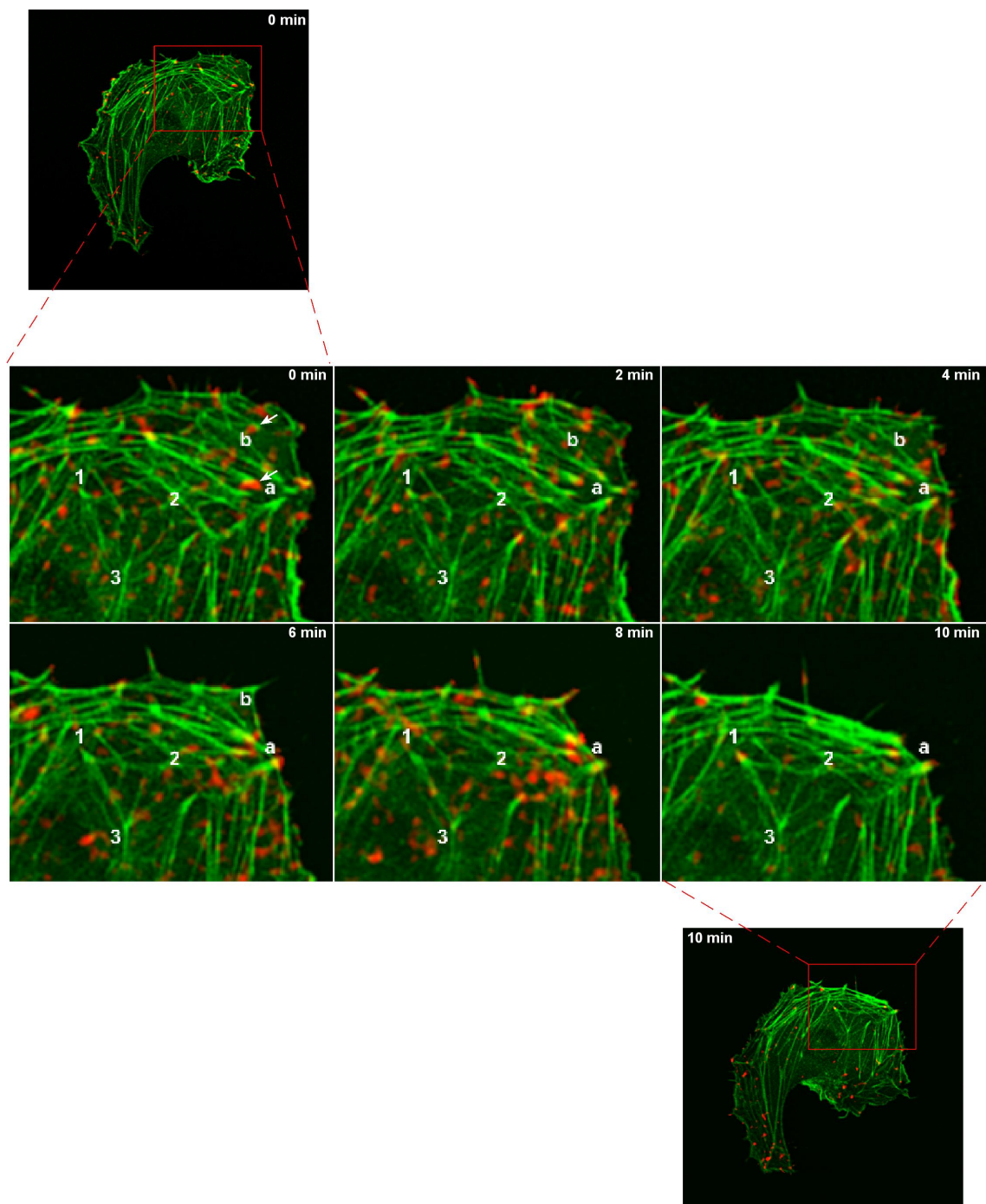


Figure 3.25: The same B16F1 cell expressing GFP:Actin as previously shown in figure 3.24 was magnified to better visualize changes in the actin cytoskeleton (green) and the high FRET efficiency pattern (red) over time. Points of interest are indicated with *a* (with arrow at 0 min) and *b* (with arrow at 0 min) and *1*, *2* and *3*. *a* and *b* illustrate a reduction in the Cy5/Cy3 ratio as the respective actin stress fiber with which they are associated is disassembled over time (the cell is moving downward and to the left). *1*, *2* and *3* point out the formation of a triangular stress fiber structure in time. At 10 min, when the high Cy5/Cy3 ratio has disappeared from *a* and *b*, a new high FRET efficiency spot appears at *1*, as the cell migrates downward.

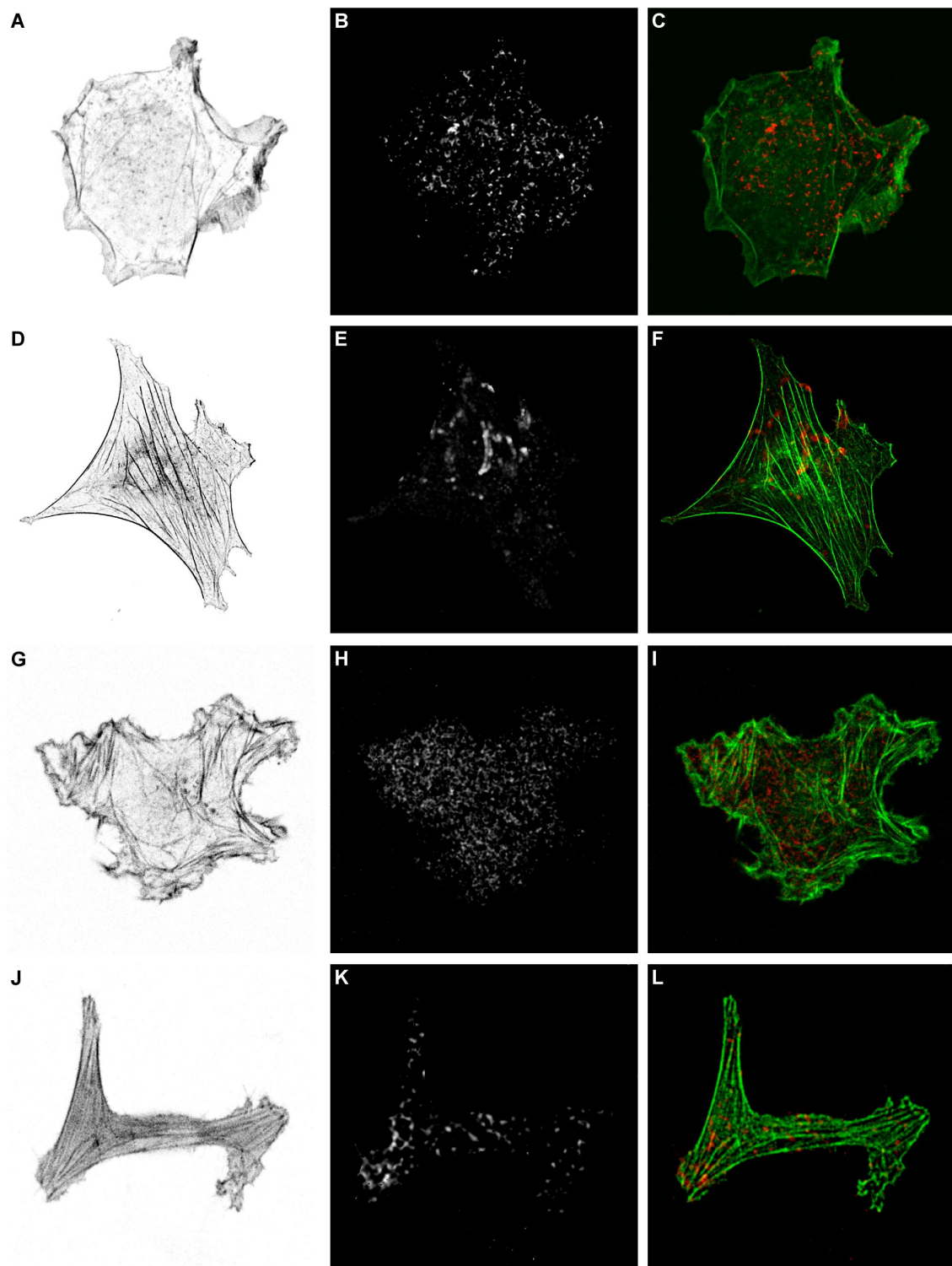


Figure 3.26: NIH/3T3 (**A-F**) and B16F1 (**G-L**) cells were co-transfected with either GFP:Actin/RhoA_{T19N} (**A-C** and **G-I**) or GFP:Actin/RhoA_{G14V} (**D-F** and **J-L**), grown on the FRETing Matrix and fixed. In the first and second column the GFP:Actin and Cy5/Cy3 ratio are shown, respectively. The overlay between the two is shown in the third column (GFP:Actin in green and Cy5/Cy3 ratio in red).

Chapter 4

Discussion

An ever-growing number of component proteins involved in the biochemical signaling that controls the morphology and function of the cellular cytoskeleton is being uncovered [28,70,103]. To get a better understanding of the role of these proteins, more needs to be learned about the spatiotemporal nature of their function. FRET biosensors are molecules designed to report on the spatiotemporal activity of specific proteins. Time and space-resolved information about the biochemical [50,52,53,99,102] and as of recent, mechanical signaling [39,94], can be gained at the sub-cellular level through the application of FRET.

Two FRET biosensors were designed. First, the set of LEGO sensors were created with the goal to visualize the biochemical signaling leading up to intracellular generation of force. Additionally, the influence of dipole distance and orientation between the two visually fluorescent proteins (VFPs) composing the biosensors was investigated. Then, a biosensor was created to visualize mechanical signaling or the force exerted by adherent cells onto the extracellular matrix (ECM).

4.1 LEGO

4.1.1 Transfection and expression

HeLaSS6 cells grown up to 60 or 80% confluency were transfected with the respective LEGO constructs. An expression period of 18-24hrs was allowed in which the cells could express properly folded LEGO constructs in amounts sufficient for examination using CLSM or flow cytometry. Microscopic examination, as well as flow cytometry analysis revealed that the presence of the RBD and the alpha-helical domain was not toxic to the cells, which continued to divide and assume their typical morphology. The fact that the presence of the biosensor was a non-intrusive was expected from previous work characterizing GFP related VFPs , as well as existing FRET biosensors [10, 24, 59, 102].

4.1.2 Lambda scan and APB

Adhering cells expressing LEGO constructs were subjected to λ scans that revealed two emission maxima corresponding with ECFP and Venus, respectively. This finding was of two-fold significance. First, the presence of both peaks indicated that the ECFP and Venus chromophores had properly matured. Furthermore, it needs to be taken into account that the emission collected during the λ scan occurred upon direct excitation of the donor only ($\lambda = 405nm$). Therefore, the presence of the second emission peak corresponding to Venus suggested the occurrence of sensitized emission and therefore FRET [18, 40]. The Venus sensitized emission seen in the λ scans was investigated further in APB experiments. Indeed, bleaching of Venus resulted in dequenching of ECFP and confirmed that sensitized emission of Venus seen during the λ scans occurred due to FRET. The non-toxic nature of the LEGO constructs, their proper expression and maturation and the presence of FRET between ECFP and Venus were the desired criteria that allowed for the further investigation of the FRET biosensors in terms of their ability to report on the activity of RhoA

GTPase.

4.1.3 Ratiometric determination of relative FRET efficiency

In order to establish a RhoA FRET biosensor of the highest sensitivity and dynamic detection range, a method needed to be applied which would enable comparison of the FRET efficiency between the different LEGO constructs. For this purpose, images obtained via CLSM were analyzed by comparing the Venus/ECFP (FRET acceptor/donor) emission ratios obtained from cells expressing the respective LEGO constructs. A comparison of the different ratios was made possible by applying the same microscopy settings during the image acquisition for all constructs.

Figures 3.6 and 3.7, exemplify a comparison of the cumulative ratio calculated from eleven cells for each LEGO. Overall, a decrease in FRET efficiency was observed, which correlated with an increase in length of the α helix and therefore in the distance between the ECFP and Venus fluorochrome. However, a decrease in FRET efficiency, as the one shown in figure 1.6, where the decrease occurs at a rate that is inversely proportional to the sixth power of the distance between the donor and the acceptor, was not seen. A linear regression of the mean values revealed that LEGO4, 7 and 8 are below, above and below, respectively, of the 95% confidence interval of the linear fit (figure 3.7). Taken as a whole, the residuals from the linear fit (figure 3.8) of the mean values of all LEGO constructs seem to follow a dampened sinusoidal behavior, of which LEGO4, 7 and 8 are the maximum amplitudes. This type of periodicity suggested the presence of α helices of varying length in the different LEGO constructs, as they would alter FRET efficiency not only by successively increasing the distance between the donor and the acceptor, but also by changing the respective dipole orientation in a repetitive manner [12]. Yet, the error bars associated with the CLSM measurements did not allow for this conclusion. The low number of cells measured with the CLSM did not allow for a statistically significant analysis of

the dependency of FRET on the expression level of the respective construct. It was necessary to establish the minimum and maximum expression level between which variation in FRET efficiency would be lowest. Flow cytometry was used to measure the necessary number of cells for establishment of such statistics (Also refer to figure 3.10 on page 48B, where those cells were chosen where variation in FRET efficiency was lower. This figure also points out dependency of FRET efficiency and variation thereof on expression level of a LEGO construct).

4.1.4 Flow cytometry

CSLM measurements of 11 cells per LEGO did not suffice to make a definitive statement about differences in FRET efficiency, due to the large standard error that they produced. A possible solution would have been to increase the number of cells measured per LEGO construct. Such an approach would have necessitated CLSM measurement sessions of 12 hrs or more, depending on the number of cells that would have needed to be measured in order to reduce the standard error of the mean. However, equal acquisition settings for all LEGO constructs over such long measurement periods could not have been warranted due to eventual changes in ambient temperature and photo-multiplier settings of the CSLM. Therefore, flow cytometry [54,55,85,88] was used to estimate the relative FRET efficiency exhibited by each of the LEGO constructs. The strength of this method is that it is quicker and more robust, as the 10000 fold amount of cells were measured, when compared to the CLSM method. The high number of cells allowed for a more precise localization of the true mean relative FRET efficiency value and for the exclusion of cells where the FRET efficiency could not be determined well due to low signal-to-noise ratio or due to overexpression artifacts.

Flow cytometry with cells transfected with LEGO only

First, cells expressing the respective LEGO constructs alone were measured. If FRET efficiency within the constructs were to depend on the donor-acceptor distance alone, then a sigmoidal decrease of FRET efficiency should be observed similar to the theoretical case shown in figure 1.6A, since the length of the α helix increases linearly with an increase in LEGO number.

Overall, a decrease in FRET efficiency did take place in the data obtained from flow cytometry. However, as was the case with CSLM-derived data, the overall decrease in FRET efficiency shown in figure 3.11 is bimodal and not sigmoidal in nature. In several cases (LEGO2, 6-8) a counter-intuitive increase in FRET efficiency occurred with an increase in LEGO number. In other words, the FRET efficiency increased despite of a subsequent increase of the distance between the donor and the acceptor.

The FRET efficiency peaks first at LEGO 2. Then follows a sharp decrease of FRET efficiency between LEGO 3 and 4, which slows at LEGO5, at which point it increases and peaks with LEGO8. Again, as it occurred between LEGO3 and 4 a sharp decrease occurs after the peak at LEGO 8 between LEGO9 and 10, which is then followed by a smaller decrease and reveals a repetitive behavior of the FRET efficiency.

Altogether, the above findings suggest that the donor-acceptor distance was not the only factor affecting the FRET efficiency within the LEGO constructs. Instead, it must be taken into account that as the alpha helix grew in length by $0.15nm$ after the addition of each amino acid for the respective LEGO constructs the orientation of the N terminus with respect to the C terminus changed by 100° [47, 90]. By extension, this resulted in a change of the dipole orientation between the donor and acceptor molecules. Since the FRET efficiency is dependent upon the respective dipole orientation of the donor and acceptor molecules, it was then to be expected

that the FRET efficiency will change upon rotation of the dipoles induced by the different alpha helices. Therefore, even though the donor-acceptor distance increases with successive LEGO number, the dipole orientation was more favorable in the case of LEGO2 or LEGO6-8, with respect to the preceding LEGO and resulted in a higher FRET efficiency. In working with DNA helices of differing length, whose 5' and 3' ends were labeled with a FRET compatible donor-acceptor pair, Clegg et al. [12] also detected a bimodal decrease in FRET efficiency with increasing length of the DNA α helix and conclude that the lack of a sigmoidal decrease in FRET efficiency is due to the DNA α helix.

LEGO cotransfected with dominant negative or constitutively active RhoA

From the onset, the function of the LEGO FRET biosensor relied on the idea that binding of RhoA GTPase will result in change of conformation of the LEGO construct and therefore a change in FRET efficiency, because the distance and/or orientation between the donor and acceptor dipoles would be changed. This approach was also successfully applied by Yoshizaki et al. [102]. A single molecule biosensor, such as LEGO, is more valuable if the change in FRET efficiency due to the binding of RhoA GTPase, especially with respect to its maximum FRET efficiency, is large. In other words, larger changes in FRET efficiency relate to a higher sensitivity of the biosensor and are therefore more easily detected.

To test for the FRET efficiency when the LEGO constructs are unbound and bound by RhoA GTPase, cells were co-transfected with the LEGO constructs and either dominant negative (RhoA_{T19N}) or constitutively active RhoA (RhoA_{G14V}), respectively [42, 68, 78]. In both types of co-transfections, an overall decrease in FRET efficiency was observed with an increase in LEGO number (figure 3.12). As was found in the previous experiment (figure 3.11), the decrease in FRET efficiency is bimodal, which is again suggestive of the presence of the alpha helical domain by means of the previous argumentation (page 74). The data shown in figure 3.11 cor-

respond more closely to those of constitutively active co-transfected samples in figure 3.12. For instance, the dominant negative co-transfection with LEGO1 in figure 3.12 shows the highest FRET efficiency, while the constitutively active co-transfection is same as in previous figure 3.11. This is in agreement to previous findings [26, 102], where it was found that the biosensor is more likely to be found in the bound state, as the endogenous active GTP bound RhoA is probably present in a sufficient amount so that it saturates the overexpressed biosensor. The RhoA GTPase is also likely to be found in its active state, since cell adhesion and cytosolic tension are required at all times [26]. Biochemical studies by Ren et al [60] also revealed that RhoA in suspended cells, as was the case during flow cytometry, is in its active, GTP bound state.

Differences in FRET efficiency were found between the two different types of co-transfections. However, the differences were not equal in all constructs. While in most cases the FRET efficiency varied, for LEGO2 and 4, there was no difference between the two scenarios. This means that even though LEGO2 showed the highest FRET efficiency in figure 3.11, it is actually the worst construct to use as a biosensor, since it would not show any differences between the “bound” and “unbound” scenario. A counter-intuitive finding was that in fact LEGO10 is the best candidate as a RhoA GTPase biosensor, because it shows the biggest percentual change in FRET efficiency between the two states, even though it has the second longest α helix and second lowest FRET efficiency readings. Examples of the ratio of cells co-transfected with LEGO10 and with either RhoA_{T19N} or RhoA_{G14V} is shown in figure 3.13.

Taken together these findings present a novel and rationalized approach toward the design of a single-molecule FRET biosensor which was optimized for the highest detection sensitivity for the RhoA GTPase. Furthermore, the set of eleven different constructs was designed so that the RBD can be exchanged for another binding domain of a protein of interest. Therefore, the LEGO constructs may be used as a kit, which serves to determine the best FRET biosensor for a protein of interest.

4.2 FRETing Matrix

According to the proposed model (figure 2.5 on page 21), a change in FRET efficiency will ensue when an adherent cell causes a local rearrangement of the labeled Fn by exerting force on it. In particular, the FRET efficiency would then be different at adhesion sites, while remaining the same elsewhere.

Rearrangement of Fn will occur as a consequence to activated RhoA GTPase, which initiates a signaling cascade that results in formation of focal adhesions (FAs). During this process, transmembrane integrin subunits, which in turn are bound to the RGD (figure 2.4 on page 20) domain of Fn, are aggregated to form an adhesion site [11, 25, 72, 97]. Simultaneously, active RhoA initiates a pathway that induces stress fibers to form, which emanate from these adhesion sites [25, 26, 62]. Then, the contractile actomyosin force exerted by these stress fibers is relayed to the FRETing Matrix via the integrin molecules, which act as an interface between the two [75, 78]. This additional force exertion onto the Fn will potentiate the bundling and therefore further increase the FRET efficiency as donor and acceptor molecules are brought closer together. A third factor that will contribute to an increase in FRET efficiency is the fact that Fn is globular when first coated on the glass coverslip. However, integrin binding will result in an unfolding of Fn so that it will assume a fibrillar shape in which it can be packed even more closely [3, 5].

4.2.1 Lambda scan and acceptor photobleaching

The λ scan function of the Leica CLSM was again successfully used to verify the presence of the donor and acceptor fluorochromes, which in this case were the Cy3 and Cy5 dyes that were initially used to label the Fn. The presence of the acceptor emission peak is caused by sensitized emission, since the acceptor was not excited directly. The λ scan then showed the presence of the donor and acceptor and furthermore suggested presence of FRET.

APB was used to verify the presence of FRET and to determine the efficiency of the energy transfer. By modifying the coating ratio of Cy3 to Cy5-labeled Fn, while keeping the coating concentration constant at $10 \frac{\mu\text{g}}{\text{ml}}$, it was possible to tune the FRET efficiency to 50%. The fact the FRET efficiency is tunable is an important aspect of the FRETing Matrix, because it enables the choice on whether to concentrate observations on a FRET efficiency increase or decrease. With a FRET efficiency of 50%, the dynamic detection range of the FRETing Matrix is such a that it is able to equally well report an increase or a decrease in FRET efficiency (also refer to figure 1.6).

4.2.2 Ratiometric visualization of contrast in FRET in the FRETing Matrix

Cells were allowed to adhere to the FRETing Matrix to determine whether they would generate contrast in FRET. The Cy5/Cy3 emission ratios were calculated and used to monitor changes in FRET efficiency. Essentially, when a cell alters the FRET efficiency, then either a decrease or an increase in sensitized acceptor emission will occur at that point, which would correspond to the opposite behavior of the donor.

First, it was found that cell spreading, adhesion and proliferation were normal. Sections C and D of figure 3.17 show that up to a three-fold increase in FRET efficiency occurred at sites of cell adhesion, while no such change in FRET efficiency was found in areas not covered by a cell. The areas of cell adhesion which exhibited the highest FRET efficiencies are also sites at which the cellular cytoskeleton adheres or is closest to the substrate, such that it enables the cell to assume its shape and proper function by establishing the required cytoplasmic tension [31, 35].

4.2.3 Verification of the ratiometric readout via acceptor photobleaching

FRET efficiency readings obtained with the ratiometric method were verified with APB. In figure 3.18, the contrast pattern in FRET efficiency made visible with the ratiometric method, was shown to overlap with the FRET efficiency pattern determined via APB. In particular, when taking into account the simultaneously recorded IRM reading, high FRET efficiency spots determined with the ratiometric and APB methods were found to overlap only and completely at cell adhesion sites. This finding was of particular interest, as it validated the ratiometric method for visualization of differences in FRET efficiency. The ratiometric method is less invasive than APB and can essentially be conducted at the maximum acquisition speed of the CSLM, which makes it suitable for live cell imaging studies.

4.2.4 FRET patterns and stress fibers in fixed cells

To further characterize the nature of the high FRET efficiency spots, cells were allowed to grow on the FRETing Matrix and were then stained with phalloidin. Phalloidin can be used to label filamentous actin and is particularly useful for visualizing stress fibers which are essential for cell shape establishment, maintenance of cytoplasmic tension and cell migration [11,23,35,87]. It was revealed that the most intense high FRET efficiency spots occur at sites from where the most prominent stress fibers emanate. The remaining high FRET efficiency spots of lower intensity occur along less pronounced stress fibers. Since more prominent stress fibers are associated with greater force exertion [39] then it can be postulated that the respective FRET efficiency spots of higher intensity formed due to larger force exertion.

It was interesting to observe that nearly all high FRET efficiency spots occurred along stress fibers, which is also where adhesion sites and therefore aggregation of labeled Fn are most likely to occur. Of interest is also the fact that the integrity of the FRETing Matrix was maintained during the optimized staining procedure,

so that changes in FRET efficiency caused by cells were maintained. Therefore, the FRETing Matrix lends itself for future studies in which for instance proteins involved in cell adhesion or mechanosensing may be investigated through antibody labeling.

4.2.5 Cell spreading

Cell binding, spreading and contraction are events that take place during cell adhesion [86,101]. The exertion of force was monitored during the cell spreading process, where B16F1 cells stably expressing GFP-actin were released onto the FRETing Matrix and observed with live cell microscopy.

In figures 3.20, 3.21 and at a higher magnification in figures 3.22 and 3.23 an example is shown in which three cells were monitored during cell spreading. The IRM and GFP perspectives show that the upper cell remains circular or non-polarized for the majority of the time, while the lower two cells are able to adhere and spread sooner. This is also reflected in the high FRET efficiency pattern, which is more pronounced in the lower cells, when compared to the upper cell.

Figure 3.23 illustrates two aspects. First, the FRETing Matrix did not exhibit a memory effect. This was shown with GFP-actin and the intensity of the FRET efficiency pattern. As the GFP-actin signal increases and decreases, there is a corresponding increase and a decrease in the FRET efficiency. This is important in dynamics studies, where transient applications of force onto the FRETing Matrix are to be visualized, as it is the case during cell spreading or cell migration. In other words, it can be said that when force is withdrawn from an area exhibiting a high FRET efficiency spot, then the intensity of this spot will decrease in a manner that corresponds with the decrease in force applied onto it and vice versa.

Figure 3.23 furthermore illustrates an interesting aspect of cell protrusion during cell spreading. Cell spreading starts with protrusion in all directions, which is then

followed by cell polarization [37, 76, 93]. The evidence in figure 3.23 shows that protrusion of the cell membrane occurred prior to the exertion of force. The sequence of events was such that first actin bundles were established, through which then in time the cells began to exert force, as shown by the Cy5/Cy3 ratio. Previous work published by another group [60], where RhoA GTPase activity during cell spreading was monitored by biochemical means, showed high RhoA activity during cell spreading, which would explain the formation of stress fibers, adhesions and high FRET efficiency spots seen at this early stage.

4.2.6 FRET patterns and stress fibers during cell migration

As was previously shown, the FRETing Matrix does not have a memory effect and is therefore suitable for the study of force exertion dynamics that the cell exhibits during cell migration. Figure 3.24 and at a higher magnification figure 3.25 exemplify a B16F1 cell expressing GFP-actin over a period of 10 minutes as it migrates on the FRETing Matrix. It becomes evident that as the cell migrates it emphasizes certain adhesions sites, while it de-emphasizes others. This is seen in the GFP-actin signal, as well as in the Cy5/Cy3 ratio. As the cell migrates toward the lower-left direction, the area shown by figure 3.24 is the trailing edge of the cell. It is generally accepted that the RhoA GTPase is active in the trailing edge, while other members of the small GTPase family (Rac and CDC42) are active in the protruding end [25, 78]. The GFP-actin signal, along with the Cy5/Cy3 ratio suggests a highly controlled retreat, in which specific stress fibers were emphasized and targeted to adhesion sites, while others were being disassembled, along with their respective adhesion sites (refer to figure 3.25). Such up- and downregulation of stress fiber and FA formation is indicative of positive and negative feedback loops controlling RhoA, whose presence have been suggested by others [60] and is important for maintenance of the necessary continuous cytoplasmic tension [31, 78]. Furthermore, evidence of sliding adhesions [95] was found where an increase of the Cy5/Cy3 ratio occurred

in time as neighboring adhesion sites joined. As the cell moved on, this adhesion site was disassembled and the force exerted was reduced (see adhesion sites at the termini of stress fibers next to letter “a” in figure 3.25).

4.3 RhoA GTPase was involved in patterning of the high FRET efficiency spots

The involvement of RhoA GTPase in the patterning and intensity of the high FRET efficiency spots was investigated in different cell types. Co-transfections of GFP-actin and either RhoA_{T19N} or RhoA_{G14V} in B16F1 or NIH-3T3 cells were conducted. These cells were then detached and allowed to adhere on a FRETing Matrix preparation. As expected from previous work [25, 26, 62], with the exception of some cortical filaments, no stress fibers were found in cells co-transfected with RhoA_{T19N}, whereas massive stress fibers spanning the entire cell were formed in cells expressing RhoA_{G14V}.

In both cell types the expression of the RhoA_{T19N} mutant resulted in a lack of stress fibers and FRET efficiency spots of weaker intensity that were randomly dispersed. On the other hand, cells co-transfected with RhoA_{G14V} produced massive stress fibers spanning the entire cell whose termini were marked by FRET efficiency spots of higher intensity and greater size than those seen in cells co-transfected with RhoA_{T19N}. Active RhoA GTPase is known to maintain and enhance FAs [72, 78], which have also been described as sites of mechanosensing [8, 95, 105]. The evidence obtained from the GFP-actin and RhoA mutant co-transfections further support that RhoA GTPase is involved in the patterning and the degree of FRET exhibited by the high FRET efficiency spots. Related recent work in which a FRET biosensor based on labeled RGD peptides, which act as ligands for transmembrane integrin molecules, was used revealed similar results. Kong et al. [39] treated cells with microtubule disrupting reagents, which are known to induce RhoA activity, and also found an increase in FRET efficiency.

4.4 Conclusions

The LEGO and FRETing Matrix biosensors were created, which rely on the principle of FRET. The LEGO sensors report on the biochemical signaling of the RhoA GTPase, the active form of which ultimately leads to the aggregation of integrin molecules to form an adhesion site from which stress fibers emanate that can generate force via actomyosin contraction. In a further step, the eleven LEGO constructs address the long standing problem of the lack of control over the transition dipole orientation of the donor with respect to that of the acceptor fluorochrome within a FRET biosensor. They represent a novel, rational approach for the sampling of different FRET efficiencies in a single molecule FRET biosensor where the protein binding domain is sandwiched between a donor and an acceptor fluorochrome. Within the eleven constructs, the distance and dipole orientation was varied with the aid of a set of α helices of increasing length between the RBD and the Venus VFP. The effect of the change in dipole orientation within the constructs was revealed with the fact that for some LEGO constructs an increase in FRET efficiency occurred even though the distance between the donor and acceptor increased. Further evidence was provided by the fact that some LEGO constructs had larger differences in FRET efficiency between the bound and the unbound state, while others showed no difference at all. Thus, the LEGO approach may aid the design of novel single molecule FRET biosensors where the binding domain of interest is located between the donor and acceptor fluorochrome, so that the specific biosensor of highest sensitivity is obtained.

Aggregation of integrin molecules to form adhesion sites and the formation of stress fibers occur both in response to active RhoA GTPase. These stress fibers can generate force based on actomyosin contraction, which is relayed via integrin molecules to the ECM. The aggregation of integrin molecules and their further bundling through the contractile force exerted by the stress fibers were visualized with the FRETing Matrix. This biosensor allows qualitative comparison of different adhesion sites or

cell adhesion during cell migration or during different treatments. The advantage over other methods is its simple preparation and fast readout, which is only limited by the acquisition speed of the microscope. Furthermore, the labeled Fn which comprises the FRETing Matrix is a permissive surface for many cell types, unlike other force detection methods which employ flexible, “wrinkling” substrates which are difficult for cells to attach to and may also lead to reduction in cell proliferation and occurrence of apoptosis [92]. The FRETing Matrix is a biosensor of continuous nature so that force exertion is directly measured at the nanometer range at every point in a field of view, which is an advantage over some methods, where the force applied at certain areas has to be inferred [86].

The FRETing Matrix lends itself for future studies in which proteins are investigated for their involvement in force exertion. Additionally, Fn-derived three-dimensional systems [13] may be modified to create a three-dimensional FRETing Matrix for the study of force exertion.

Index

A

α helix, [x](#), [10](#), [14](#), [16](#), [17](#), [36](#), [43](#), [72](#),
[74–76](#), [83](#)
actomyosin, [x](#), [7](#), [8](#), [77](#), [83](#)
adhesion, [1](#)

B

biosensor, [x](#), [xi](#), [8](#), [10–13](#), [39](#), [48–50](#),
[70–72](#), [75](#), [76](#), [82–84](#)

C

cytoskeleton, [x](#), [1](#), [2](#), [4](#), [7](#), [8](#), [11](#)

F

FRET, [10](#)

F

focal adhesion, [x](#), [xi](#), [2](#), [4](#), [8](#), [11](#), [77](#),
[81](#), [82](#)
FRET, [x](#), [xi](#), [8](#), [10](#), [11](#), [13](#), [19](#), [20](#), [22](#),
[26](#), [32](#), [33](#), [38](#), [39](#), [43](#), [46](#), [48–50](#),
[53](#), [55](#), [58](#), [60](#), [63](#), [65](#), [67](#), [70–80](#),
[82](#), [83](#)

G

GAP, [4](#), [11](#)
GDI, [4](#)
GEF, [4](#)
GTPases, [x](#), [xi](#), [2](#), [4](#)

I

integrin, [x](#), [1](#), [4](#), [7](#), [8](#), [20](#), [77](#), [82](#),
[83](#)
intermediate filaments, [1](#)

L

lamellipodium, [2](#), [7](#)

M

microtubules, [5](#)

M

microfilaments, [1](#)

microtubules, [x](#), [1](#), [4](#), [82](#)
migration, [1](#)
morphology, [1](#)

R

RBD, [13](#)
RhoA, [x](#), [xi](#), [2](#), [4](#), [7](#), [8](#), [11–13](#), [49](#), [67](#),
[75–77](#), [81–83](#)
RhoA mutant, [82](#)
RhoA mutants, [48](#)
RhoA_{G14V}, [4](#), [28](#), [50](#), [67](#), [75](#), [76](#),
[82](#)
RhoA_{T19N}, [4](#), [28](#), [50](#), [67](#), [75](#), [76](#),
[82](#)

S

sliding adhesion, [2](#), [81](#)
stress fiber, [x](#), [xi](#), [2](#), [4](#), [11](#), [13](#), [21](#), [58](#),
[63](#), [65](#), [67](#), [77](#), [79](#), [81–83](#)

V

VFP, [13](#)

Bibliography

- [1] R. Albrecht and I. Weber. Interference reflection microscopy. <http://www.els.net>, 2001.
- [2] W. E. Allen, D. Zicha, A. J. Ridley, and G. E. Jones. A role for cdc42 in macrophage chemotaxis. *J Cell Biol*, 141(5):1147–57, 1998.
- [3] G. Baneyx, L. Baugh, and V. Vogel. Coexisting conformations of fibronectin in cell culture imaged using fluorescence resonance energy transfer. *Proc Natl Acad Sci U S A*, 98(25):14464–8, Dec 2001.
- [4] G. Baneyx, L. Baugh, and V. Vogel. Fibronectin extension and unfolding within cell matrix fibrils controlled by cytoskeletal tension. *Proc Natl Acad Sci U S A*, 99(0027-8424):5139–43, 2002.
- [5] L. Baugh and V. Vogel. Structural changes of fibronectin adsorbed to model surfaces probed by fluorescence resonance energy transfer. *J Biomed Mater Res A*, 69(1549-3296):525–34, 2004.
- [6] K. A. Beningo, M. Dembo, I. Kaverina, J. V. Small, and Y. L. Wang. Nascent focal adhesions are responsible for the generation of strong propulsive forces in migrating fibroblasts. *J Cell Biol*, 153(4):881–8, 2001.
- [7] A. D. Bershadsky, N. Q. Balaban, and B. Geiger. Adhesion-dependent cell mechanosensitivity. *Annu Rev Cell Dev Biol*, 19(1081-0706):677–95, 2003.
- [8] I. Bischofs and U. Schwarz. Cell organization in soft media due to active mechanosensing. *Proc Natl Acad Sci U S A*, 100(16):9274–9, Aug 2003.
- [9] A. L. Bishop and A. Hall. Rho gtpases and their effector proteins. *Biochem J*, 348 Pt 2(0264-6021):241–55, 2000.
- [10] G. Bunt and F. S. Wouters. Visualization of molecular activities inside living cells with fluorescent labels. *Int Rev Cytol*, 237(0074-7696):205–77, 2004.
- [11] K. Burridge and M. Chrzanowska-Wodnicka. Focal adhesions, contractility, and signaling. *Annu Rev Cell Dev Biol*, 12(1081-0706):463–518, 1996.
- [12] R. M. Clegg, A. I. Murchie, A. Zechel, and D. M. Lilley. Observing the helical geometry of double-stranded dna in solution by fluorescence resonance energy transfer. *Proc Natl Acad Sci U S A*, 90(0027-8424):2994–8, 1993.

- [13] E. Cukierman, R. Pankov, and K. M. Yamada. Cell interactions with three-dimensional matrices. *Curr Opin Cell Biol*, 14(0955-0674):633–9, 2002.
- [14] A. S. CURTIS. The mechanism of adhesion of cells to glass. a study by interference reflection microscopy. *J Cell Biol*, 20(0021-9525):199–215, 1964.
- [15] A. S. Curtis. Cell reactions with biomaterials: the microscopies. *Eur Cell Mater*, 1(1473-2262):59–65, 2001.
- [16] E. H. Danen and K. M. Yamada. Fibronectin, integrins, and growth control. *J Cell Physiol*, 189(0021-9541):1–13, 2001.
- [17] M. Department-of-Biophysics-and-Cell-Biology University of Debrecen. *ReFlex FACS Software Package*. Department of Biophysics and Cell Biology, University of Debrecen, Medical and Health Science Center, Debrecen, Hungary, 2005.
- [18] A. Esposito and F. S. Wouters. *Current Protocols in Cell biology*. John Wiley & Sons, Inc., 2004.
- [19] E. Ezratty, M. Partridge, and G. Gundersen. Microtubule-induced focal adhesion disassembly is mediated by dynamin and focal adhesion kinase. *Nat Cell Biol*, 7(6):581–90, Jun 2005.
- [20] C. Fiorentini, L. Falzano, S. Travaglione, and A. Fabbri. Hijacking rho gtpases by protein toxins and apoptosis: molecular strategies of pathogenic bacteria. *Cell Death Differ*, 10(1350-9047):147–52, 2003.
- [21] T. Förster. Zwischenmolekulare energiewanderung und fluoreszenz. *Ann. Physik*, 2:55–75, 1948.
- [22] E. Fuchs. Keith r. porter lecture, 1996. of mice and men: genetic disorders of the cytoskeleton. *Mol Biol Cell*, 8(2):189–203, Feb 1997.
- [23] B. Geiger, Z. Avnur, G. Rinnerthaler, H. Hinssen, and V. J. Small. Microfilament-organizing centers in areas of cell contact: cytoskeletal interactions during cell attachment and locomotion. *J Cell Biol*, 99(1 Pt 2):83s–91s, 1984.
- [24] H. H. Gerdes and C. Kaether. Green fluorescent protein: applications in cell biology. *FEBS Lett*, 389(0014-5793):44–7, 1996.
- [25] A. Hall. Rho gtpases and the actin cytoskeleton. *Science*, 279(0036-8075):509–14, 1998.
- [26] A. Hall and C. D. Nobes. Rho gtpases: molecular switches that control the organization and dynamics of the actin cytoskeleton. *Philos Trans R Soc Lond B Biol Sci*, 355(0962-8436):965–70, 2000.
- [27] R. Heim. Green fluorescent protein forms for energy transfer. *Methods Enzymol*, 302(0076-6879):408–23, 1999.
- [28] A. Howe. Regulation of actin-based cell migration by camp/pka. *Biochim Biophys Acta*, 1692(2-3):159–74, Jul 2004.

- [29] R. O. Hynes. Integrins: bidirectional, allosteric signaling machines. *Cell*, 110(0092-8674):673–87, 2002.
- [30] D. Ilić, Y. Furuta, S. Kanazawa, N. Takeda, K. Sobue, N. Nakatsuji, S. Nomura, J. Fujimoto, M. Okada, and T. Yamamoto. Reduced cell motility and enhanced focal adhesion contact formation in cells from fak-deficient mice. *Nature*, 377(6549):539–44, Oct 1995.
- [31] D. E. Ingber. Tensegrity: the architectural basis of cellular mechanotransduction. *Annu Rev Physiol*, 59(0066-4278):575–99, 1997.
- [32] D. E. Ingber. Mechanical signaling and the cellular response to extracellular matrix in angiogenesis and cardiovascular physiology. *Circ Res*, 91(10):877–87, 2002.
- [33] Invitrogen. (<http://probes.invitrogen.com/resources/spectraviewer/>) *Fluorescence Spectra Viewer*. Molecular Probes, 2005.
- [34] K. Kaibuchi, S. Kuroda, and M. Amano. Regulation of the cytoskeleton and cell adhesion by the rho family gtpases in mammalian cells. *Annu Rev Biochem*, 68(0066-4154):459–86, 1999.
- [35] K. Katoh, Y. Kano, M. Amano, H. Onishi, K. Kaibuchi, and K. Fujiwara. Rho-kinase-mediated contraction of isolated stress fibers. *J Cell Biol*, 153(0021-9525):569–84, 2001.
- [36] I. Kaverina, O. Krylyshkina, K. Beningo, K. Anderson, Y.-L. Wang, and J. V. Small. Tensile stress stimulates microtubule outgrowth in living cells. *J Cell Sci*, 115(Pt 11):2283–91, 2002.
- [37] I. Kaverina, O. Krylyshkina, and J. V. Small. Microtubule targeting of substrate contacts promotes their relaxation and dissociation. *J Cell Biol*, 146(5):1033–44, 1999.
- [38] A. Kodama, T. Lechler, and E. Fuchs. Coordinating cytoskeletal tracks to polarize cellular movements. *J Cell Biol*, 167(2):203–7, Oct 2004.
- [39] H. Kong, T. Polte, E. Alsberg, and D. Mooney. Fret measurements of cell-contraction forces and nano-scale clustering of adhesion ligands varied by substrate stiffness. *Proc Natl Acad Sci U S A*, 102(12):4300–5, Mar 2005.
- [40] J. R. Lakowicz. *Principles of Fluorescence Spectroscopy*. Kluwer Academic/Plenum, New York, 2 edition, 1999.
- [41] E. Lane and W. McLean. Keratins and skin disorders. *J Pathol*, 204(4):355–66, Nov 2004.
- [42] J. E. Lee, G. Bokoch, and B. T. Liang. A novel cardioprotective role of rhoa: new signaling mechanism for adenosine. *FASEB J*, 15(0892-6638):1886–94, 2001.
- [43] D. Lehnert, B. Wehrle-Haller, C. David, U. Weiland, C. Ballestrem, B. A. Imhof, and M. Bastmeyer. Cell behaviour on micropatterned substrata: lim-

- its of extracellular matrix geometry for spreading and adhesion. *J Cell Sci*, 117(0021-9533):41–52, 2004.
- [44] N. Li Jeon, H. Baskaran, S. K. W. Dertinger, G. M. Whitesides, L. Van de Water, and M. Toner. Neutrophil chemotaxis in linear and complex gradients of interleukin-8 formed in a microfabricated device. *Nat Biotechnol*, 20(8):826–30, 2002.
- [45] H. F. Lodish. *Molecular Cell Biology*. W. H. Freeman and Company, 4th edition, 1999.
- [46] W. E. Lowry, J. Huang, Y.-C. Ma, S. Ali, D. Wang, D. M. Williams, M. Okada, P. A. Cole, and X.-Y. Huang. Csk, a critical link of g protein signals to actin cytoskeletal reorganization. *Dev Cell*, 2(6):733–44, 2002.
- [47] S. Marqusee, V. H. Robbins, and R. L. Baldwin. Unusually stable helix formation in short alanine-based peptides. *Proc Natl Acad Sci U S A*, 86(14):5286–90, 1989.
- [48] P. Martin. Wound healing—aiming for perfect skin regeneration. *Science*, 276(5309):75–81, Apr 1997.
- [49] G. Meyer and E. Feldman. Signaling mechanisms that regulate actin-based motility processes in the nervous system. *J Neurochem*, 83(3):490–503, Nov 2002.
- [50] A. Miyawaki, O. Griesbeck, R. Heim, and R. Y. Tsien. Dynamic and quantitative ca^{2+} measurements using improved cameleons. *Proc Natl Acad Sci U S A*, 96(5):2135–40, 1999.
- [51] A. Miyawaki, J. Llopis, R. Heim, J. M. McCaffery, J. A. Adams, M. Ikura, and R. Y. Tsien. Fluorescent indicators for ca^{2+} based on green fluorescent proteins and calmodulin. *Nature*, 388(0028-0836):882–7, 1997.
- [52] A. Miyawaki, A. Sawano, and T. Kogure. Lighting up cells: labelling proteins with fluorophores. *Nat Cell Biol*, Suppl(1465-7392):S1–7, 2003.
- [53] A. Miyawaki and R. Y. Tsien. Monitoring protein conformations and interactions by fluorescence resonance energy transfer between mutants of green fluorescent protein. *Methods Enzymol*, 327(0076-6879):472–500, 2000.
- [54] P. Nagy, L. Bene, W. Hyun, G. Vereb, M. Braun, C. Antz, J. Paysan, S. Damjanovich, J. Park, and J. Szollosi. Novel calibration method for flow cytometric fluorescence resonance energy transfer measurements between visible fluorescent proteins. *in press*, 2005.
- [55] A. W. Nguyen and P. S. Daugherty. Evolutionary optimization of fluorescent proteins for intracellular fret. *Nat Biotechnol*, 23(3):355–60, 2005.
- [56] B. Olofsson. Rho guanine dissociation inhibitors: pivotal molecules in cellular signalling. *Cell Signal*, 11(0898-6568):545–54, 1999.

- [57] M. Pop, K. Aktories, and G. Schmidt. Isotype-specific degradation of rac activated by the cytotoxic necrotizing factor 1. *J Biol Chem*, 279(0021-9258):35840–8, 2004.
- [58] T. Reid, T. Furuyashiki, T. Ishizaki, G. Watanabe, N. Watanabe, K. Fujisawa, N. Morii, P. Madaule, and S. Narumiya. Rhotekin, a new putative target for rho bearing homology to a serine/threonine kinase, pkn, and rhotekin in the rho-binding domain. *J Biol Chem*, 271(0021-9258):13556–60, 1996.
- [59] A. Rekas, J.-R. Alattia, T. Nagai, A. Miyawaki, and M. Ikura. Crystal structure of venus, a yellow fluorescent protein with improved maturation and reduced environmental sensitivity. *J Biol Chem*, 277(0021-9258):50573–8, 2002.
- [60] X. D. Ren, W. B. Kiosses, and M. A. Schwartz. Regulation of the small gtp-binding protein rho by cell adhesion and the cytoskeleton. *EMBO J*, 18(0261-4189):578–85, 1999.
- [61] G. P. Resch, K. N. Goldie, A. Krebs, A. Hoenger, and J. V. Small. Visualisation of the actin cytoskeleton by cryo-electron microscopy. *J Cell Sci*, 115(Pt 9):1877–82, 2002.
- [62] A. J. Ridley. Rho family proteins: coordinating cell responses. *Trends Cell Biol*, 11(0962-8924):471–7, 2001.
- [63] A. J. Ridley. Rho gtpases and cell migration. *J Cell Sci*, 114(0021-9533):2713–22, 2001.
- [64] A. J. Ridley and A. Hall. Signal transduction pathways regulating rho-mediated stress fibre formation: requirement for a tyrosine kinase. *EMBO J*, 13(0261-4189):2600–10, 1994.
- [65] G. Rinnerthaler, B. Geiger, and J. V. Small. Contact formation during fibroblast locomotion: involvement of membrane ruffles and microtubules. *J Cell Biol*, 106(3):747–60, 1988.
- [66] D. Rivelino, E. Zamir, N. Q. Balaban, U. S. Schwarz, T. Ishizaki, S. Narumiya, Z. Kam, B. Geiger, and A. D. Bershadsky. Focal contacts as mechanosensors: externally applied local mechanical force induces growth of focal contacts by an mdia1-dependent and rock-independent mechanism. *J Cell Biol*, 153(6):1175–86, 2001.
- [67] M. Roederer, S. De Rosa, R. Gerstein, M. Anderson, M. Bigos, R. Stovel, T. Nozaki, D. Parks, and L. Herzenberg. 8 color, 10-parameter flow cytometry to elucidate complex leukocyte heterogeneity. *Cytometry*, 29(0196-4763):328–39, 1997.
- [68] K. Rottner, A. Hall, and J. V. Small. Interplay between rac and rho in the control of substrate contact dynamics. *Curr Biol*, 9(12):640–8, 1999.
- [69] V. P. Sah, T. M. Seasholtz, S. A. Sagi, and J. H. Brown. The role of rho in g protein-coupled receptor signal transduction. *Annu Rev Pharmacol Toxicol*, 40(0362-1642):459–89, 2000.

- [70] E. Sahai. Mechanisms of cancer cell invasion. *Curr Opin Genet Dev*, 15(1):87–96, 2005.
- [71] A. Schmidt and M. N. Hall. Signaling to the actin cytoskeleton. *Annu Rev Cell Dev Biol*, 14(1081-0706):305–38, 1998.
- [72] S. M. Schoenwaelder and K. Burridge. Bidirectional signaling between the cytoskeleton and integrins. *Curr Opin Cell Biol*, 11(0955-0674):274–86, 1999.
- [73] J. Y.-J. Shyy and S. Chien. Role of integrins in endothelial mechanosensing of shear stress. *Circ Res*, 91(9):769–75, 2002.
- [74] R. M. Siegel, F. K. Chan, D. A. Zacharias, R. Swofford, K. L. Holmes, R. Y. Tsien, and M. J. Lenardo. Measurement of molecular interactions in living cells by fluorescence resonance energy transfer between variants of the green fluorescent protein. *Sci STKE*, 2000(38):PL1, 2000.
- [75] J. Small, K. Rottner, P. Hahne, and K. I. Anderson. Visualising the actin cytoskeleton. *Microsc Res Tech*, 47(1):3–17, 1999.
- [76] J. V. Small and I. Kaverina. Microtubules meet substrate adhesions to arrange cell polarity. *Curr Opin Cell Biol*, 15(1):40–7, 2003.
- [77] J. V. Small, I. Kaverina, O. Krylyshkina, and K. Rottner. Cytoskeleton cross-talk during cell motility. *FEBS Lett*, 452(1-2):96–9, 1999.
- [78] J. V. Small, K. Rottner, and I. Kaverina. Functional design in the actin cytoskeleton. *Curr Opin Cell Biol*, 11(0955-0674):54–60, 1999.
- [79] J. V. Small, K. Rottner, I. Kaverina, and K. I. Anderson. Assembling an actin cytoskeleton for cell attachment and movement. *Biochim Biophys Acta*, 1404(3):271–81, 1998.
- [80] J. V. Small, T. Stradal, E. Vignall, and K. Rottner. The lamellipodium: where motility begins. *Trends Cell Biol*, 12(3):112–20, 2002.
- [81] D. Strassheim, R. A. Porter, S. H. Phelps, and C. L. Williams. Unique in vivo associations with smgGDPs and rhoGDI and different guanine nucleotide exchange activities exhibited by rhoA, dominant negative rhoA(asn-19), and activated rhoA(val-14). *J Biol Chem*, 275(0021-9258):6699–702, 2000.
- [82] L. Stryer. Fluorescence energy transfer as a spectroscopic ruler. *Annu Rev Biochem*, 47(0066-4154):819–46, 1978.
- [83] L. Stryer and R. P. Haugland. Energy transfer: a spectroscopic ruler. *Proc Natl Acad Sci U S A*, 58(0027-8424):719–26, 1967.
- [84] J. Swanson, M. Johnson, K. Beningo, P. Post, M. Mooseker, and N. Araki. A contractile activity that closes phagosomes in macrophages. *J Cell Sci*, 112 (Pt 3):307–16, Feb 1999.
- [85] G. Szentesi, G. Horvath, I. Bori, G. Vamosi, J. Szollosi, R. Gaspar, S. Damjanovich, A. Jenei, and L. Matyus. Computer program for determining fluo-

- rescence resonance energy transfer efficiency from flow cytometric data on a cell-by-cell basis. *Comput Methods Programs Biomed*, 75(3):201–11, 2004.
- [86] J. L. Tan, J. Tien, D. M. Pirone, D. S. Gray, K. Bhadriraju, and C. S. Chen. Cells lying on a bed of microneedles: an approach to isolate mechanical force. *Proc Natl Acad Sci U S A*, 100(4):1484–9, 2003.
- [87] N. Tapon and A. Hall. Rho, rac and cdc42 gtpases regulate the organization of the actin cytoskeleton. *Curr Opin Cell Biol*, 9(0955-0674):86–92, 1997.
- [88] L. Tron, J. Szollosi, S. Damjanovich, S. H. Helliwell, D. J. Arndt-Jovin, and T. M. Jovin. Flow cytometric measurement of fluorescence resonance energy transfer on cell surfaces. quantitative evaluation of the transfer efficiency on a cell-by-cell basis. *Biophys J*, 45(0006-3495):939–46, 1984.
- [89] B. Verwer. Bd facsdiva option. *BD Biosciences*, 2002.
- [90] D. Voet and J. G. Voet. *Biochemistry*. John Wiley & Sons, Inc., second edition edition, 1995.
- [91] V. Vogel and G. Baneyx. The tissue engineering puzzle: a molecular perspective. *Annu Rev Biomed Eng*, 5(1523-9829):441–63, 2003.
- [92] H. B. Wang, M. Dembo, and Y. L. Wang. Substrate flexibility regulates growth and apoptosis of normal but not transformed cells. *Am J Physiol Cell Physiol*, 279(5):C1345–50, 2000.
- [93] H.-R. Wang, Y. Zhang, B. Ozdamar, A. A. Ogunjimi, E. Alexandrova, G. H. Thomsen, and J. L. Wrana. Regulation of cell polarity and protrusion formation by targeting rhoa for degradation. *Science*, 302(1095-9203):1775–9, 2003.
- [94] Y. Wang, E. L. Botvinick, Y. Zhao, M. W. Berns, S. Usami, R. Y. Tsien, and S. Chien. Visualizing the mechanical activation of src. *Nature*, 434(7036):1040–5, 2005.
- [95] B. Wehrle-Haller and B. Imhof. The inner lives of focal adhesions. *Trends Cell Biol*, 12(0962-8924):382–9, 2002.
- [96] B. Wehrle-Haller and B. Imhof. Integrin-dependent pathologies. *J Pathol*, 200(4):481–7, Jul 2003.
- [97] B. Wehrle-Haller and B. A. Imhof. Actin, microtubules and focal adhesion dynamics during cell migration. *Int J Biochem Cell Biol*, 35(1):39–50, 2003.
- [98] F. S. Wouters, P. I. Bastiaens, K. W. Wirtz, and T. M. Jovin. Fret microscopy demonstrates molecular association of non-specific lipid transfer protein (nsltp) with fatty acid oxidation enzymes in peroxisomes. *EMBO J*, 17(0261-4189):7179–89, 1998.
- [99] F. S. Wouters, P. J. Vermeer, and P. I. Bastiaens. Imaging biochemistry inside cells. *Trends Cell Biol*, 11(5):203–11, 2001.

- [100] J. Xu, F. Wang, A. Van Keymeulen, P. Herzmark, A. Straight, K. Kelly, Y. Takuwa, N. Sugimoto, T. Mitchison, and H. Bourne. Divergent signals and cytoskeletal assemblies regulate self-organizing polarity in neutrophils. *Cell*, 114(2):201–14, Jul 2003.
- [101] K. M. Yamada and D. W. Kennedy. Dualistic nature of adhesive protein function: fibronectin and its biologically active peptide fragments can autoinhibit fibronectin function. *J Cell Biol*, 99(1 Pt 1):29–36, 1984.
- [102] H. Yoshizaki, Y. Ohba, K. Kurokawa, R. E. Itoh, T. Nakamura, N. Mochizuki, K. Nagashima, and M. Matsuda. Activity of rho-family gtpases during cell division as visualized with fret-based probes. *J Cell Biol*, 162(2):223–32, 2003.
- [103] E. Zamir and B. Geiger. Components of cell-matrix adhesions. *J Cell Sci*, 114(Pt 20):3577–9, 2001.
- [104] E. Zamir and B. Geiger. Molecular complexity and dynamics of cell-matrix adhesions. *J Cell Sci*, 114(Pt 20):3583–90, 2001.
- [105] E. Zamir, M. Katz, Y. Posen, N. Erez, K. M. Yamada, B. Z. Katz, S. Lin, D. C. Lin, A. Bershadsky, Z. Kam, and B. Geiger. Dynamics and segregation of cell-matrix adhesions in cultured fibroblasts. *Nat Cell Biol*, 2(4):191–6, 2000.
- [106] D. Zicha, W. E. Allen, P. M. Brickell, C. Kinnon, G. A. Dunn, G. E. Jones, and A. J. Thrasher. Chemotaxis of macrophages is abolished in the wiskott-aldrich syndrome. *Br J Haematol*, 101(4):659–65, 1998.
- [107] M. Zuker. On finding all suboptimal foldings of an rna molecule. *Science*, 244(0036-8075):48–52, 1989.

Curriculum Vitae

Personal Information

Name: Mitkovski, Mišo
Address: Levinstr. 9A, 37079 Göttingen, Germany
Birthplace: Bad Homburg, Germany
Date of birth: 01 Aug., 1973
Nationality: Macedonian
Telephone: +49 179 704 7865
E-mail: mitkovm@gmail.com

Education

June 2002 - present (*PhD Student*)
European Neuroscience Institute, Göttingen Göttingen, Germany
December 2001
Gesellschaft für Biotechnologische Forschung Braunschweig, Germany
October 2001 - May 2002
Max-Planck-Institute for Biophysical Chemistry Göttingen, Germany
September 1999 - June 2001 (*Research Assistant*)
University of Idaho Moscow, ID, U.S.A.
September 1997 - May 1999 (*Degree: Master of Science, Major: Botany*)
University of Idaho Moscow, ID, U.S.A.
June 1994 - August 1994
University of Washington Seattle, WA, U.S.A.
September 1993 - May 1997 (*Degree: Bachelor of Arts, Major: Biology, Minor: Chemistry*)
Whitman College Walla Walla, WA, U.S.A.
September 1992 - August 1993 (*Major: Biology*)
Columbia Basin College Pasco, WA, U.S.A.